

Aalborg University
Department of Chemistry and Bioscience

MASTER THESIS



AALBORG UNIVERSITY
DENMARK

Konstantin Jefimov
Paulius Krebsas

CAPROCK CHARACTERIZATION FOR CARBON DIOXIDE STORAGE IN RESERVOIRS USING AN INTEGRATED APPROACH

Supervisors: Ismaila Adetunji Jimoh
Erik Gydesen Søgaard

Study programme: Oil and Gas Technology, MSc

Esbjerg 2018

Title Page

Thesis from: Aalborg University Esbjerg (AAUE)

Address: Niels Bohrs Vej 8, 6700 Esbjerg, Denmark

Study programme: Oil and Gas Technology, Master of Science in Engineering

Semester: 10th semester

Group number: K10OG-5-F18

Thesis title: Caprock Characterization For Carbon Dioxide Storage In Reservoirs Using An Integrated Approach

ECTS: 30

Authors: Konstantin Jefimov and Paulius Krebsas

Supervisors: Senior Service Delivery Petrophysicist Ismaila Adetunji Jimoh (Schlumberger) and Professor Erik Gydesen Sogaard (AAUE)

Thesis period: February – June 2018

Submission date: 7th of June 2018

Declaration

We declare that this thesis has been composed solely by ourselves and that it has not been submitted, in whole or in part, in any previous application for a degree. Except where states otherwise by reference or acknowledgment, the work presented is entirely our own. By signing authors take the full responsibility for the contents of the master thesis.



Konstantin Jefimov



Paulius Krebsas

7th of June 2018
Esbjerg, Denmark

Abstract

Current master thesis deals with petrophysical and geomechanical analysis of the Tensleep formation, Teapot Dome field in Natrona County, Wyoming, United States of America. The main aspect of the analysis is the selection of a suitable location (well) to carry out the injection of CO₂ as the last and integral part of the carbon capture and sequestration technology. This is done through a careful analysis of a list of factors that affect the integrity of the caprock, which during the thesis was considered of critical importance. Dominant part of the analysis is performed with two key Schlumberger softwares: Techlog Wellbore Software Platform, which integrates all wellbore-centric data types into multidisciplinary workflows and Petrel EP Software Platform, which allows to perform well correlations, interpret seismic data, build reservoir models, calculate volumes and others. The well selection process is divided into three key parts: (i) ductility-brittleness maps are created for the caprock zone according to the cross-plots of Young's modulus-Bulk modulus and (ii) calculation of HCPV amounts for the reservoir and (iii) juxtaposing these techniques via six types of constraints that yield a number of possible scenarios, from which the most optimal well can be selected.

Some of the calculated results include: average lithology composition for the caprock is 78% dolomite, 14% limestone, 8% anhydrite. Average composition of the reservoir is 52% limestone, 25% dolomite, 23% sandstone. Permeability was calculated with Coates' method, resulting in an average value of 0.0594 mD for the caprock. The average volume of shale in the caprock is 0.5188 v/v, leading to the conclusion that it is shaly. It was concluded from the geomechanical analysis that the average fracture gradient for the caprock was 3444.161 ± 62.011 psi, while the average maximum and minimum horizontal stresses were 4650 psi and 2600 psi, respectively. Well 17-WX-21 was selected as the most suitable well for injection, because it lied within a ductile zone as confirmed by the mineralogical, geomechanical and rock strength results. Calculated storage capacity is 168.68 Mt.

Keywords: CO₂ injection, CCS, caprock integrity, wireline logs, reservoir analysis, caprock analysis, storage capacity, ductility.

Acknowledgment

Firstly, we would like to thank Ismaila Adetunji Jimoh, who was our supervisor and was helping us during the months that we were doing the thesis. Without his knowledge and contacts the work would surely be impossible. Likewise, want to thank Schlumberger, which provided us the licenses for the softwares (and the software itself).

Secondly, we are very grateful to Sachin Kriplani, who was kind enough to spare a significant amount of his free time helping us to get the Petrel[©] model to function properly and taught us a great deal regarding that software. Without him the analysis in Petrel[©] have been, if not impossible, then at least very troublesome.

Additionally, we would like to thank Jacquelin Cobos, who was very helpful during the thesis period and assisted us when we first launched Techlog[©]. Also, thank you, Jhony Quintal, for answering our questions regarding some technical issues in the thesis.

What is more, we would like to thank our fellow colleagues from oil and gas technology program, especially Erica Godinho for her reminders that coffee breaks are of utmost importance; Mathias Jørgensen for reminding to work harder; Frida Franic and Konstantinos Sapounas for their hospitality, cold drinks and delicious food.

We also thank the IT department of Aalborg University Esbjerg, whose workers were keenly helping us with the license corrections and PC administrative rights issues.

We want to acknowledge the US Geological Survey Site (USGS) and Rocky Mountain Oilfield Testing Center (RMOTC), since a compelling amount of work done in the thesis was based on the public data that is available via these organisations.

Individually, I, Konstantin, want to thank my family for the great support and encouragement that I have been receiving during the two years of my master studies in Denmark. Without them I would never have reached that far.

Nomenclature

Symbol	Definiton
ρ_{bulk}	Formation bulk density
μ	Viscosity
Δt_{comp}	Compressional slowness of the bulk formation
A	Cross section of the rock
BMK_{DYN}	Dynamic bulk modulus
B_o	Formation oil volumetric factor
CALD	Caliper log
CEP	Capillary entry pressure
CCS	Carbon capture and sequestration
C_{dyn}	Dynamic bulk compressibility
CNL	Neutron porosity
CO ₂	Carbon dioxide
cP	Centipoise
DT	Compressional slowness log
E	Young's modulus
EOR	Enhanced oil recovery
ft	Feet (1 ft = 0.3048 m)
FG	Fracture gradient
FPRESS	Formation pressure log
FTEMP	Formation temperature log
g	Gravity acceleration (9.80665 m/s ²)
G	Shear modulus
G_{dyn}	Dynamic shear modulus
GR	Gamma ray log
Gt	Gigaton ($10^9 \times ton$)
HC	Hydrocarbon
HCPV	Hydrocarbon per volume
HS	Hydrostatic pressure
HSE	Health, safety and environment

IFT	Interfacial tension
IGR	Gamma ray shale index
k	Permeability
K	Bulk modulus
K_{dyn}	Dynamic bulk modulus
L	Length of the rock
mD	Millidarcy
MD	Measured depth log
Mpsi	Mega-psi ($10^6 \times psi$)
Mt	Mega-ton ($10^6 \times ton$)
ND	Neutron density log
NTG	Net-to-gross
OOIP	Original oil in place
OWC	Oil-water contact
NPHI	Neutron porosity log
PEFZ	Photoelectric factor log
PHIE	Effective porosity log
PHIT	Total porosity log
PR_{DYN}	Poisson's ratio
PV	Pore volume
psi	pounds per square inch (1 psi = 0.0689 bar)
ppm	parts per million
Q	Flow rate
RHOB	Bulk density log
RT	Deep resistivity log
R_{sp}	Ratio between shear and compressional slowness
RB/BBL	Reservoir barrels per barrel
RF	Recovery factor
SP	Spontaneous potential log
STOIIP	Stock-tank original oil in place
SMG_{DYN}	Dynamic shear modulus
S_W	Water saturation
S_{WC}	Critical water saturation
StDev	Standard deviation
T_{str}	Tensile strength
UCS	Unconfined compressive strength

v/v	volume per volume
VANH	Volume of anhydrite
VDOL	Volume of dolomite
VLS	Volume of limestone
V_{sh}	Volume of shale
VSS	Volume of sandstone
WAG	Water alternating gas injection
YME_{DYN}	Dynamic Young's modulus

Contents

Title Page	i
Declaration	ii
Abstract	iii
Acknowledgment	iv
Nomenclature	v
1 Introduction	1
1.1 Problem Definition and Methods	1
1.2 Thesis Outline	2
2 Literature Review	3
2.1 Teapot Dome	3
2.1.1 Historical background	3
2.1.2 Geology	3
2.1.3 Pennsylvanian Tensleep Formation	4
2.1.4 Lithology	4
2.2 Carbon Capture and Sequestration	7
2.2.1 CO ₂ Capturing	8
2.2.2 CO ₂ Transportation	9
2.2.3 CO ₂ Injection	10
2.2.4 Risks Regarding CO ₂ Injection	14
2.2.5 Selection of the Injection Site and Wells	16
2.2.6 CO ₂ Storage Capacity Theory	17
3 Petrophysics	19
3.1 Reservoir Properties	19
3.1.1 Porosity	19
3.1.2 Water Saturation	20
3.1.3 Permeability	21
3.1.4 Volume of Shale	22
4 Geomechanics	24
4.1 Caprock Overview	24
4.2 Pore Pressure	28
4.3 Fracture Gradient	29
4.4 Elastic Properties	30
4.5 Rock Strength	33

5	Results and Discussion	35
5.1	Tensleep Reservoir Characterization	35
5.2	General Data	35
5.2.1	Location and Types of Logs	35
5.2.2	Thickness of Zones	36
5.2.3	Temperature Computation	36
5.2.4	Pressure Computation	39
5.3	CO ₂ Solubility Modelling	39
5.4	Petrophysics	41
5.4.1	Total and Effective Porosity	41
5.4.2	Water Saturation	43
5.4.3	Permeability	44
5.4.4	Volume of Shale	47
5.4.5	Lithology	50
5.5	Geomechanics	54
5.5.1	Pore Pressure	55
5.5.2	Fracture Gradient	55
5.5.3	Elastic Properties	56
5.5.4	Rock Strength	60
5.5.5	Brittleness-Ductility Analysis	61
5.6	Petrel [©] Model	63
5.6.1	Problem Set-Up and Limitations	63
5.6.2	Property Modelling	66
5.6.3	Volume Calculation	84
5.6.4	Well Selection Process	85
5.6.5	Capacity Calculation	91
6	Conclusions	98
	Bibliography	101
A	Wireline Logs	107
A.1	Gamma Ray Log	107
A.2	Neutron Porosity Log	107
A.3	Depth log	108
A.4	Caliper log	108
A.5	Acoustic (sonic) logs	109
A.5.1	Compressional slowness log	109
A.6	Resistivity log	110
A.7	Formation temperature log	110
A.8	Formation density log (FDL)	111
B	Additional Data From Techlog[©]	112
B.1	Porosity	112
B.2	Water Saturation	117
B.3	Volume of Shale and Mineralogy	122
B.4	Bulk Modulus and Bulk Density	126
B.5	Permeability	130

C Additional Data From Petrel[©]	133
C.1 Elevation Depth	133

List of Figures

2.1	Teapot Dome location. Source: [60]	4
2.2	Stratigraphic column of the Teapot Dome Field with the emphasis on the Tensleep and Goose Egg sections. Area marked with red line is the region of interest in the current thesis. Cell width is not correlated with the actual thickness of the zone. Modified after: [37, 24]	5
2.3	Stratigraphy of the caprock and the reservoir. Modified after: [78, 22]	6
2.4	Different possibilities of storing CO ₂ . Source: [74]	8
2.5	(a) Depiction of a fossil plant that has the required technology to capture, compress and transport CO ₂ to the injection area, where CO ₂ is injected beneath the caprock. (b) Depiction how the capillary menisci trap the free CO ₂ . (c) Capillary tube analogy showcasing the water-wet case. Source: [32]	11
2.6	CO ₂ density as a function of hydrostatic gradient. Source: [8]	12
2.7	Phase diagram of CO ₂ . Source: [67]	12
3.1	Depiction of effective and total porosity within the rock. Source: [19]	20
4.1	Wettability states between supercritical water, mineral substrate and CO ₂ . Source: [65]	26
4.2	Depth vs pressure, different types of pressure and depiction of effective stress. Source: [33]	29
4.3	Relationship between stress, strain, elastic and ductile deformations. Young's modulus is denoted as the slope between stress and strain. Source: [54]	32
4.4	Different types of stresses. Source: [54]	34
5.1	Map of the wells in the Teapot Dome region.	36
5.2	Solubility of CO ₂ as a function of pressure at constant T=94 °C and FW salinity of 20975 ppm.	40
5.3	Solubility of CO ₂ as a function of temperature at constant P=148 bar and FW salinity of 20975 ppm.	40
5.4	Solubility of CO ₂ as a function of FW salinity at P=148 bar and T=94 °C.	41
5.5	Depiction of total and effective porosity values for all the 10 wells in the caprock (Permian layer).	42
5.6	Depiction of total and effective porosity values for all the 10 wells in the reservoir (Pennsylvanian layer). Dark blue indicates the total porosity. Light blue indicates the effective porosity.	43

5.7	Depiction of a cumulative porosity values for all the 10 wells in the caprock (Permian layer).	44
5.8	Depiction of a cumulative porosity values for all the 10 wells in the reservoir (Pennsylvanian layer).	45
5.9	Total porosity logs across the Permian (Caprock) and Pennsylvanian (Reservoir) layers for Wells 62-TPX-10 and 67-TPX 1-10.	45
5.10	Water saturation logview for well 67 TPX 1-10 in the caprock (Permian layer).	46
5.11	Depiction of cumulative water saturation of all the 10 wells in the caprock (Permian layer).	47
5.12	Depiction of cumulative water saturation of all the 10 wells in the reservoir (Pennsylvanian layer).	48
5.13	Depiction of cumulative permeability in the 10 wells in the caprock (Permian layer).	49
5.14	Depiction of cumulative permeability in the 10 wells in the reservoir (Pennsylvanian layer).	49
5.15	Permeability vs porosity crossplot for well 67 TPX 1-10. Red line indicates the trendline.	50
5.16	Depiction of cumulative volume of the shale of all the 10 wells in the reservoir (Pennsylvanian layer).	51
5.17	Depiction of cumulative volume of the shale of all the 10 wells in the caprock (Permian layer).	52
5.18	GR and VSH logs for wells 62-TPX-10 and 67 TPX 1-10 showcasing the calculation of VSH.	52
5.19	Average lithology composition of caprock (Permian layer) of all the wells.	53
5.20	Average lithology composition of reservoir (Pennsylvanian layer) of all the wells.	53
5.21	Mineralogy for wells 62-TPX-10 and 67 TPX 1-10 in the Permian layer.	54
5.22	Mineralogy for wells 62-TPX-10 and 67 TPX 1-10 in Pennsylvanian layer.	54
5.23	Logview for Well 11-AX-11: determination of rock physics, overburden stress, elastic properties, rock strength, horizontal stress and lithology.	55
5.24	Multi-well histogram of pore pressure values across 10 wells in the reservoir zone (Pennsylvanian layer).	56
5.25	Multi-well histogram of fracture pressure across 10 wells in the caprock zone (Permian layer).	57
5.26	Shear modulus multi-well histogram depicting pressure values across 10 wells in the caprock zone (Permian layer).	57
5.27	Multi-well histogram of Young's modulus in the caprock zone (Permian layer).	58
5.28	Multi-well histogram of Poisson's ratio in the caprock zone (Permian layer).	59
5.29	Multi-well histogram of bulk modulus in the caprock zone (Permian layer).	60

5.30	Unconfined Compressive Strength of all the 10 wells in the caprock zone (Permian layer).	61
5.31	Tensile strength of all the 10 wells in the caprock zone (Permian layer).	61
5.32	Relationship between Young’s modulus and Poisson’s ratio for Well 67 TPX 1-10 (Permian zone).	62
5.33	Upscaled and non-upscaled distribution of water saturation for the caprock (on the left) and the reservoir (on the right). Red color shows the well logs, green color the cells after the upscaling process.	65
5.34	Cross-section of the area of interest. Layers’ thickness is not correlated to actual thickness.	66
5.35	3D property model for pore pressure in the reservoir area with views from the top and the bottom.	67
5.36	3D property model for permeability in the caprock (Permian layer). North to South direction with all the well locations.	69
5.37	3D property model for permeability in the reservoir (Pennsylvanian layer). North to South direction with all the well locations.	70
5.38	Cross-section for permeability in the caprock (Permian layer) and reservoir (Pennsylvanian layer). West view.	71
5.39	3D property model for porosity in the caprock (Permian layer). North to South direction and the location of all 10 wells.	72
5.40	3D property model for porosity in the reservoir (Pennsylvanian layer). North to South direction and the location of all 10 wells.	73
5.41	3D property model for the volume of shale in the reservoir (Pennsylvanian layer). North to South direction with the locations of the 10 wells.	74
5.42	Cross-section of the volume of shale in the caprock (Permian layer) and reservoir (Pennsylvanian layer). West side view.	75
5.43	3D property model for water saturation in the reservoir (Pennsylvanian layer). North to South view with all the locations of the wells.	76
5.44	Cross-section of water saturation in the caprock (Permian layer) and reservoir (Pennsylvanian layer). West side view.	77
5.45	3D property model for fracture gradient in the caprock zone (Permian layer). North to South view with all the locations of the wells.	78
5.46	3D property model for vertical stress in the caprock zone (Permian layer). North to South view with all the locations of the wells.	79
5.47	Cross section for vertical stress in the caprock zone (Permian layer). West view.	80
5.48	2D property model for the maximum horizontal stress in the caprock zone (Permian layer). North to South view with all the locations of the wells.	81
5.49	2D property model for the minimum horizontal stress in the caprock zone (Permian layer). North to South view with all the locations of the wells.	82
5.50	3D property model for Poisson’s ratio in the caprock zone (Permian layer). North to South view with all the locations of the wells.	83

5.51	3D property model for shear modulus in the caprock zone (Permian layer) north to south view with all the locations of the wells. . . .	84
5.52	3D property model for Young’s modulus in the caprock zone (Permian layer) north to south view with all the locations of the wells. . . .	85
5.53	Volume calculation with OWC. Blue plane depicts the OWC. Area above the plane is the basis for the volume calculation.	86
5.54	Process flow diagram explaining the procedure for the selection of the optimal injection well.	87
5.55	2D map showcasing the areas of ductile and brittle zones in the caprock (Permian layer).	88
5.56	2D map of the areas with the highest volumes in the reservoir (Pennsylvanian layer).	90
5.57	2D map of the areas with the highest hydrocarbon pore volumes in the reservoir (Pennsylvanian layer).	91
5.58	2D map of the areas with the most optimal conditions for CO ₂ injection and storage for Case 1. High HCPV constraint, constant ductility.	92
5.59	2D map of the areas with the most optimal conditions for CO ₂ injection and storage for Case 2. Medium HCPV constraint, constant ductility.	93
5.60	2D map of the areas with the most optimal conditions for CO ₂ injection and storage for Case 3. Low HCPV constraint, constant ductility.	94
5.61	2D map of the areas with the most optimal conditions for CO ₂ injection and storage for Case 4. High ductility constraint, constant HCPV.	95
5.62	2D map of the areas with the most optimal conditions for CO ₂ injection and storage for Case 5. Medium ductility constraint, constant HCPV.	96
5.63	2D map of the areas with the most optimal conditions for CO ₂ injection and storage for Case 6. Low ductility constraint, constant HCPV.	97
5.64	Cumulative probability plot of the storage capacity calculated with Equation 2.4 and cumulative probability with SipMath Excel Add-On.	97
A.1	Principle of a sonic log. Source: [50]	109
A.2	Formation density log. Source: [47]	111
B.1	Depiction of total porosity values for each individual well in the reservoir (Pennsylvanian layer).	112
B.2	Depiction of total porosity values for each individual well in the caprock (Permian layer).	113
B.3	Depiction of cumulative effective porosity values for all 10 wells in the caprock (Permian layer).	113
B.4	Depiction of cumulative effective porosity values for all 10 wells in the reservoir (Pennsylvanian layer).	114

B.5	Logs for all 10 wells showing the effective and total porosity in the caprock (Permian layer). Logs from left: 11-AX-11, 17-WX-21, 25-1-X-14, 25-LX-11, 41-AX-3, 51-CMX-10-WD, 57-AX-28, 57-WX-3, 62-TPX-10, 67-TPX 1-10.	115
B.6	Logs for all 10 wells showing the effective and total porosity in the reservoir (Pennsylvanian layer). Logs from left: 11-AX-11, 17-WX-21, 25-1-X-14, 25-LX-11, 41-AX-3, 51-CMX-10-WD, 57-AX-28, 57-WX-3, 62-TPX-10, 67-TPX 1-10.	116
B.7	Depiction of water saturation values for each individual well in the caprock (Permian layer).	117
B.8	Depiction of water saturation values for each individual well in the reservoir (Pennsylvanian layer).	118
B.9	Depiction of the average water saturation of each individual well in the reservoir (Pennsylvanian layer).	118
B.10	Depiction of the average water saturation of each individual well in the caprock (Permian layer).	119
B.11	Depiction of the cross-plot for water saturation and porosity for the reservoir zone across all the wells with data density legend.	119
B.12	Logs for all 10 wells showing water saturation in the caprock (Permian layer). Logs from left: 11-AX-11, 17-WX-21, 25-1-X-14, 25-LX-11, 41-AX-3, 51-CMX-10-WD, 57-AX-28, 57-WX-3, 62-TPX-10, 67-TPX 1-10.	120
B.13	Logs for all 10 wells showing water saturation in the reservoir (Pennsylvanian layer). Logs from left: 11-AX-11, 17-WX-21, 25-1-X-14, 25-LX-11, 41-AX-3, 51-CMX-10-WD, 57-AX-28, 57-WX-3, 62-TPX-10, 67-TPX 1-10.	121
B.14	Matrix histograms showcasing the volume of shale in each of the 10 wells in the reservoir (Pennsylvanian layer).	122
B.15	Matrix histograms showcasing the volume of shale in each of the 10 wells in the caprock (Permian layer).	123
B.16	Logs of all the 10 wells showing the volume of shale in the caprock (Permian layer) and reservoir (Pennsylvanian layer). Logs from left: 11-AX-11, 17-WX-21, 25-1-X-14, 25-LX-11, 41-AX-3, 51-CMX-10-WD, 57-AX-28, 57-WX-3, 62-TPX-10, 67-TPX 1-10.	124
B.17	Logs of all the 10 wells showcasing the mineralogy in the caprock (Permian layer) and reservoir (Pennsylvanian layer). Logs from left: 11-AX-11, 17-WX-21, 25-1-X-14, 25-LX-11, 41-AX-3, 51-CMX-10-WD, 57-AX-28, 57-WX-3, 62-TPX-10, 67-TPX 1-10.	125
B.18	Logs of all the 10 wells presenting the bulk density in the caprock (Permian layer). Logs from left: 11-AX-11, 17-WX-21, 25-1-X-14, 25-LX-11, 41-AX-3, 51-CMX-10-WD, 57-AX-28, 57-WX-3, 62-TPX-10, 67-TPX 1-10.	127
B.19	Logs of all the 10 wells presenting the bulk density in the reservoir (Pennsylvanian layer). Logs from left: 11-AX-11, 17-WX-21, 25-1-X-14, 25-LX-11, 41-AX-3, 51-CMX-10-WD, 57-AX-28, 57-WX-3, 62-TPX-10, 67-TPX 1-10.	128

B.20	Logs of all the 10 wells presenting the bulk modulus in the caprock (Permian layer). Logs from left: 11-AX-11, 17-WX-21, 25-1-X-14, 25-LX-11, 41-AX-3, 51-CMX-10-WD, 57-AX-28, 57-WX-3, 62-TPX-10, 67-TPX 1-10.	129
B.21	Logs of all the 10 wells presenting the permeability in the caprock (Permian layer). Logs from left: 11-AX-11, 17-WX-21, 25-1-X-14, 25-LX-11, 41-AX-3, 51-CMX-10-WD, 57-AX-28, 57-WX-3, 62-TPX-10, 67-TPX 1-10.	131
B.22	Logs of all the 10 wells presenting the permeability in the reservoir (Pennsylvanian layer). Logs from left: 11-AX-11, 17-WX-21, 25-1-X-14, 25-LX-11, 41-AX-3, 51-CMX-10-WD, 57-AX-28, 57-WX-3, 62-TPX-10, 67-TPX 1-10.	132
C.1	Elevation depth distribution for reservoir (Pennsylvanian layer).	133

List of Tables

2.1	Overview of CO ₂ capturing methods. Modified after: [72]	10
2.2	Common parameters and their values for a CO ₂ transporation pipeline. Modified after: [67, 6]	10
2.3	Main positive and negative indicators for CO ₂ -injection site selection. Modified after: [5]	17
3.1	Typical values of permeability for an oil reservoir. Modified after: [47]	22
4.1	Change of ductility for different lithologies. Modified after: [24, 14]	27
4.2	Geomechanical properties and their formulas with nomenclature. Modified after: [24]	31
5.1	Tensleep reservoir properties as of 2005. Modified after: [37]	35
5.2	Average thicknesses of Permian and Pennsylvanian layers across different wells.	37
5.3	Wells and their wireline logs used in the thesis. Yellow color means that the log was present. Red color means that the log was not available.	38
5.4	Default densities used for computation of lithologies in Techlog [©] . Source: Techlog [©]	50
5.5	Statistical properties of the elastic parameters.	59
5.6	Statistical properties of the rock strength parameters	60
5.7	Cell properties for reservoir and caprock layers in the simulation model.	66
5.8	Key properties used for volumetric calculation in Petrel [©] .	84
5.9	Results of the volume calculation for reservoir area in Petrel [©] .	86
5.10	Constraint values for well selection	90
5.11	Properties used for the computation of storage capacity in Equation 2.4.	92

Introduction

1.1 Problem Definition and Methods

The key objective of this master thesis is to perform a petrophysical, geological, geomechanical analysis of the possibilities to inject CO₂ into Tensleep reservoir in Teapot Dome field in Wyoming, USA for storage purposes. CO₂ injection requires proper planning, taking into account the strength of the caprock, reactions of CO₂ with the formation water, effect of fractures on permeability etc. The data used in the master thesis is in free access and serves as a basis for all the analytical work performed. The work is concentrated on two regions: Permian layer (the caprock) and Pennsylvanian layer (the reservoir). Throughout the work three key assumptions are made: (i) the reservoir is depleted (the oil is produced), (ii) none of the wells are plugged and (iii) the wells are vertical (i.e. they are not directional-deviated wells). Our master thesis is based on calculations performed with Schlumberger software: log analysis with Techlog[©], reservoir 3D visualisation in Petrel[©]. Main limitation of the thesis was time, since the amount of it was not sufficient to perform the Eclipse[©] simulation. The main targets (methodology) addressed in the thesis can be summarised with the following comprehensive list:

1. perform a geological analysis of the Teapot Dome field;
2. describe the lithology present in the region (focusing on both the caprock and the reservoir);
3. perform a petrophysical (porosity, water saturation etc.) analysis of the region using the wireline logs (see Table 5.3 for more information) in Techlog[©];
4. perform a geomechanical analysis of the Tensleep region. It consists of calculating the elastic properties and rock strength properties as seen in Chapter 5.5;
5. study the trends of the properties in two distinct geological zones: Pennsylvanian (the reservoir) and Permian (the caprock)
6. study the theoretical background of the CCS process (three main parts: capturing, transportation and injection), focusing mainly on the injection;
7. carry out the work in Petrel[©], mapping out the wells and the petrophysical properties over the total area of the Tensleep field;

8. decide, based on the performed work and literature, what are the optimal geological and geographical conditions for the injection of CO₂;
9. choose an existing well to perform CO₂ injection;
10. calculate the storage capacity of carbon dioxide and solubility of CO₂ in formation water.

1.2 Thesis Outline

Current thesis contains 151 pages, 101 figures and 17 tables. It is divided as presented in the following list:

- Chapter 2 describes the theoretical background of the Tensleep region and the theory behind a typical CCS process;
- Chapter 3 describes the theoretical background of the petrophysical properties;
- Chapter 4 describes the theoretical background of the geomechanical properties;
- Chapter 5 presents the results obtained in Techlog[©] and Petrel[©];
- Chapter 6 presents main conclusions that have been drawn from the performed work, additionally, future work possibilities are described;
- Appendix A describes in detail the theory behind each type of wireline log that has been used throughout the thesis;
- Appendix B presents the figures that were obtained from Techlog[©], but not used in the main part of the thesis;
- Appendix C presents the figures that were obtained from Petrel[©], but not used in the main part of the thesis.

Literature Review

2.1 Teapot Dome

2.1.1 Historical background

Teapot Dome field, which is also known as the Naval Petroleum Reserve (NPR), is the last United States of America government owned oil field. Government ownership means that the data from the wells (well logs) is in free access. The field was established in 1915 by president Woodrow Wilson. Full production from the field was initiated in year 1976. Currently, it is a promising place for CO₂ injection and sequestration. First CO₂ injections were carried out in 2004 [37, 57].

2.1.2 Geology

Teapot Dome is Late Cretaceous to Eocene Laramide¹-age anticline that is located in central Wyoming (USA), near the southwestern part of the Powder River Basin, 30 km north of Casper, Wyoming. It has a total area of approximately 46 km² with more than 1200 wells [59]. One study describes that *"Teapot Dome is one of several productive structural-style hydrocarbon traps associated with Laramide structures in this area and is part of a larger structural complex, comprised of Salt Creek anticline to the north and the Sage Spring Creek and Cole Creek oil fields to the south"* [66].

Oil from Teapot Dome is mainly produced from Second Wall Creek, Third Wall Creek, Muddy, Dakota, Tensleep, Niobrara Shale intervals. The deepest interval is the Tensleep sandstone. Figures 2.1 and 5.34 show the location of the field relative to the geography of the United States and the Teapot Dome stratigraphic column, respectively.

¹period of mountain-building events that affected much of western North America in Late Cretaceous and Paleogene time.

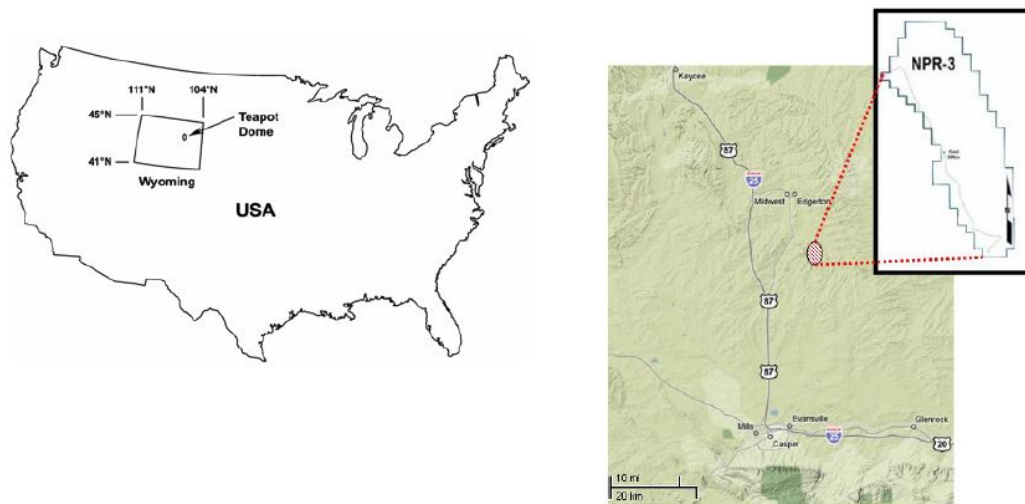


Figure 2.1: Teapot Dome location. Source: [60]

2.1.3 Pennsylvanian Tensleep Formation

Tensleep Formation consists of 91.4 meters (300 ft) of multi-sequenced boundaries of dolomite and sandstone [37]. Tensleep Formation is located between the dolomite strata and Goose-Egg Formation, which is the caprock. According to Zhang *et al.* [81], the sandstones in Tensleep change from being predominantly marine (having corals and crinoids) in the bottom to being continental on the top with thick eolian layers. They also concluded that cementation² processes have significantly reduced the permeability and porosity in the Tensleep Formation, but the dissolution during diagenesis³ has enhanced it. Friedmann *et al.* [36] report an average porosity value of 8% and average permeability of 80 mD. These values depend on the depositional environments and the degree of cementation. Figure 2.3 shows the stratigraphy of the caprock and reservoir region. Core descriptions and logs provide information that Tensleep is fractured [60].

2.1.4 Lithology

Before any sub-surface operation, the determination of lithology and rock type is vital for an effective process to occur. Lithology is gross term that determines the rock layer present in the reservoir, while the term of rock layer is more precise description as it reflects the pores systems within the layer. This allows collecting vital reservoir properties that are used to predict flow, volumes and fluid saturations. It can be said that lithology focuses mainly on the grain level, while the rock type looks at the pores.

The lithology can be determined directly by obtaining a physical sample from

² hardening of clastic sediments (those formed from preexisting rock fragments) by the precipitation of mineral in the pore spaces.

³ sum of all processes (mainly chemical), with which the changes in the sediment are brought about after its deposition, but before its final lithification.

Period	Formation		Lithology	Thickness (m)	Depth (m)	Productive
Upper Cretaceous	Steele			59		
		Sussex		9		○
				88	69	
		Shannon		37	157	●
				413	194	●
						●
	Niobrara Shale		137		●	
	Carlisle Shale		73	744	○	
	Frontier	1st Wall Creek		49	817	○
				75	866	
		2nd Wall Creek		20	940	●
			53	960		
3rd Wall Creek			2	1013	●	
			81	1015		
Lower Cretaceous	Mowry Shale			70	1096	
	Muddy Sandstone			5	1166	●
	Thermopolis Shale			41	1170	
	Dakota			26	1212	●
	Lakota			3	1237	●
Jurassic	Morrison			82	1241	
	Sundance	Upper		29	1323	○
Lower			46	1352		
Triassic	Chugwater Group	Crow Mtn		24	1398	○
		Alcova LS		6	1422	
		Red Peak		158	1428	
Permian	Goose Egg			98	1586	
Pennsylvanian	Tensleep			98	1684	●
Mississippian	Amsden			49	1782	
Devonian	Madison			91	1830	○

LEGEND

	Sandstone
	Shale
	Limestone
●	Oil bearing zone
○	Water bearing zone

Figure 2.2: Stratigraphic column of the Teapot Dome Field with the emphasis on the Tensleep and Goose Egg sections. Area marked with red line is the region of interest in the current thesis. Cell width is not correlated with the actual thickness of the zone. Modified after: [37, 24]

the wells. This is a sure but a rough way to determine lithology, as the samples gathered from the well could not be reflecting the true rock type within the well

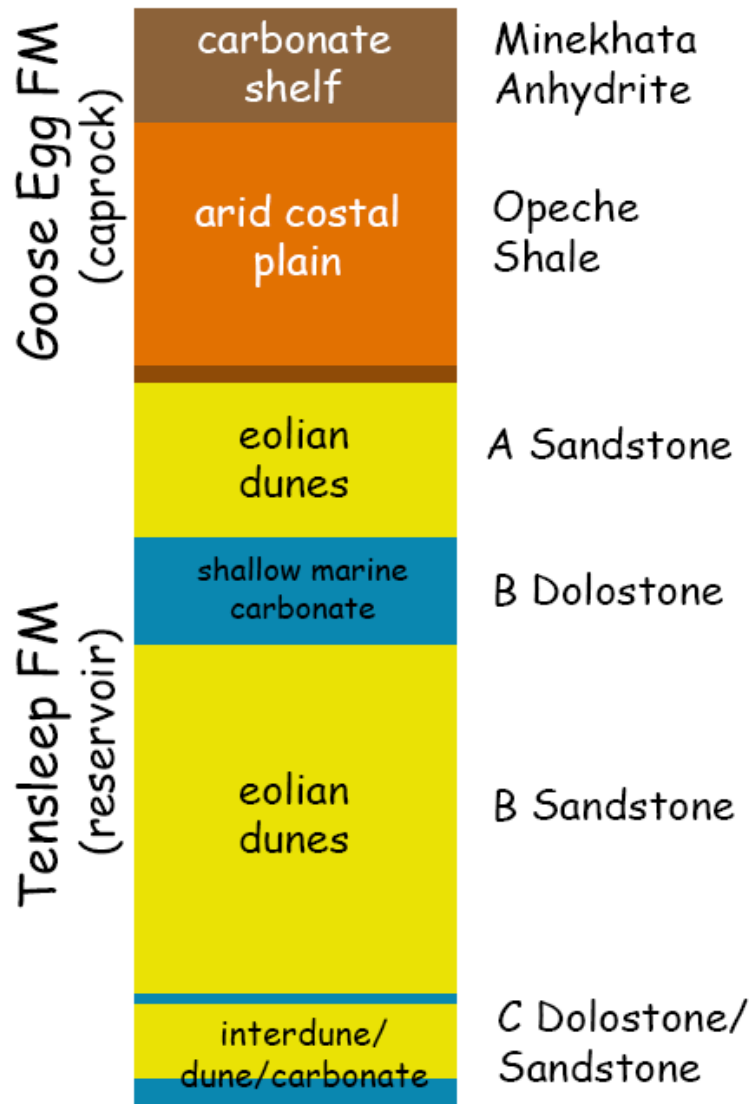


Figure 2.3: Stratigraphy of the caprock and the reservoir. Modified after: [78, 22]

due to the presence of mud and clay, weaker rocks and cuttings.

As the well is set, more detailed core samples such as sideway core samples can be obtained for a more precise investigation. Indirect method is determining the lithology from the log data that is collected from the wells. This log data is compared to information in the log data catalogs that are usually provided by the logging companies. In the case of our thesis, the focus is on the Goose Egg and Tensleep formations. They have mainly four different rock layers: sandstone, limestone, dolomite, anhydrite. Following list describes each type in a brief manner [45]:

- Sandstone is one of the most common lithology types worldwide. The rock grain size are around the size of usual sand grains. This rock type is very favorable as a reservoir due to its high porosity (more porous than carbonates) and permeability. In sandstones, a permeable reservoir is usually a porous reservoir.

- Limestone is a carbonate sedimentary rock, mostly composed of structural components of organic origin. The grain size depends on the skeletal structure of the dominant organic component (corals and shells). Minor components like dolomite, chert and clay are also found in limestones.
- Dolomite is a widely distributed anhydrous carbonate, predominantly composed of calcium/magnesium carbonate. Due to the high levels of calcium and magnesium molecules, the formations form in a structural way.
- Anhydrite is mainly composed of calcium sulfate. This rock type is part of the evaporate group of minerals and mainly forms from evaporating seawater or in the process of gypsum ($\text{CaSO}_4 \times 2\text{H}_2\text{O}$) dehydration. Anhydrites can occur as caprocks if they are above salt domes, providing favorable geomechanical properties for caprocks.

Using Techlog[©], aforementioned lithologies were identified in all the wells. Results are presented in Chapter 5.4.5.

2.2 Carbon Capture and Sequestration

Global energy consumption is in a constant growth and although renewable energy is firmly getting a place in the industry, the fossil fuel is still the most important source of energy. Combustion of the fossil fuels increases the concentrations of CO_2 , which is also the main reason behind human-activity driven global warming. Industrial activities are regarded the key reason behind the increase of CO_2 concentration in air from 280 ppm to 370 ppm since the industrial revolution in 19th century; additionally, CO_2 concentration is believed to reach a critical level in the next 20-30 years [4]. In 2016, average CO_2 concentration in air was 403 ppm, which is an average growth of 2 ppm/year in the last decade. The world total CO_2 emission amount in 2016 was 32.3 Gt. [2]

According to various authors, CCS (carbon capture and sequestration) is the only method that significantly allows to reduce the emissions of CO_2 in the atmosphere [49, 80, 72]. Other options, although not that effective, include energy efficiency improvements, nuclear power, renewable energy sources and using less carbon-intensive fuels [55].

Key idea behind CCS is the capturing of CO_2 from industrial plants and safe, monitored way of storage by means of injecting the CO_2 into either depleted oil/gas reservoir, deep saline aquifer or unminable coal seams, where it could be stored for thousands or millions of years [75]. CO_2 injection has also been a significant EOR method for tens of years. This means that injection of CO_2 into a depleted oil reservoir allows to deal with two processes at the same time (enhanced oil production and CO_2 storage) [77]. Figure 2.4 shows the typical solutions for CO_2 injection for onshore conditions. This type of injection poses a number of different topics (and complete research areas) that need to be understood, e.g.

geophysical and geochemical behaviour of the reservoir, monitoring and modelling of the injection, risk assessment, commercial viability etc.

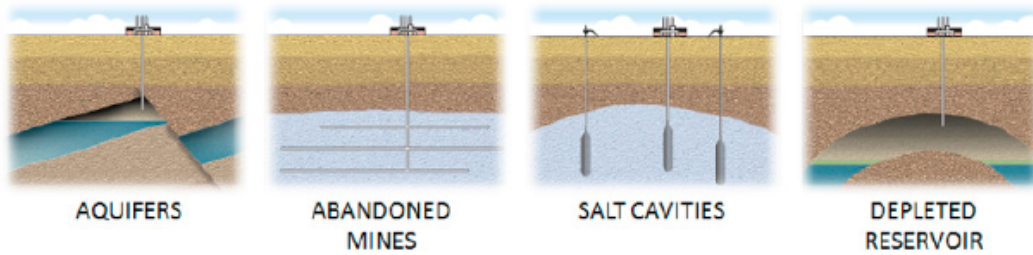


Figure 2.4: Different possibilities of storing CO₂. Source: [74]

CCS process is divided into four main parts [75]:

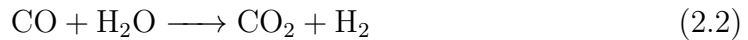
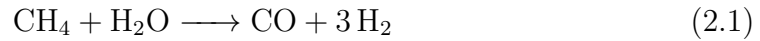
1. CO₂ capturing, which involves the separation of CO₂ from the gas stream using specific chemical solvents and according to some authors [23], [72] remains the most expensive part of the CCS process. According to Dooley *et al.* [29], the cost of CO₂ capturing, depending on the type of industry, ranges from 6-60 USD per ton of CO₂;
2. transportation, which involves compressing the CO₂ to a liquid state (to reduce the volume) and piping it from the industrial site to the injection site;
3. storage, which consists of the injection of the gas to the suitable location;
4. monitoring, which usually means detecting changes in pressure, temperature and making sure CO₂ does not leak.

2.2.1 CO₂ Capturing

This chapter is going to give a brief overview of the most common technologies in the field of CO₂ capturing, which is the first step in the CCS process. Carbon capturing technologies can be divided into three main categories, based on when in the industrial process CO₂ is captured:

1. pre-combustion capturing;
2. post-combustion capturing;
3. oxyfuel combustion.

Pre-combustion capturing means transforming the fuel (coal, biomass etc.) into syngas using gasification, then syngas is shifted to H₂ and CO₂ after which the hydrogen can be removed. Reactions 2.1 to 2.2 showcase this process (natural gas is taken as an example fuel). Conversion of syngas to H₂ and CO₂ takes place at elevated pressures (over 40 bars). [72]



Main advantages of a pre-combustion capturing is the lower cost compared to post-combustion and the high pressure of CO_2 that means lower compression costs. Key disadvantages are complex engineering regarding chemical reaction modelling and large capital investment requirements.

Another major capturing method is post-combustion capturing. In this case CO_2 is captured from the flue gas after the power generation and this is carried out by using various liquid solvents like monoethanolamine. Main advantages of post-combustion are for example the fact that the technologies involved are mature, and there is vast amount of scientific work that is taking place. One of the disadvantages can be regarded the high cost of these processes. Post-combustion technologies can be divided into three major parts: capturing with adsorption, absorption and with membrane technologies. [72]

Oxyfuel capturing is the third technology and it generally means reacting a fuel with pure stream of oxygen (95-99% purity). Result will be high concentration of CO_2 in the gas. This will mean that the exhaust will be water and CO_2 and the separation of CO_2 from the stream is easier because all that is required is to condense the water. This is also the key advantage. However, new materials that can withstand very high temperatures have to be used and that could lead to a significantly higher cost of the process [72, 55]. Most commonly used post-combustion methods for CO_2 capturing and their advantages and disadvantages can be seen in Table 2.1.

2.2.2 CO_2 Transportation

Second important part of the CCS technology is the CO_2 transportation. It involves moving the CO_2 from one location to another via onshore or offshore pipelines or special CO_2 -transporting ships. Several constraints exist that have to be taken into account when designing a pipeline for CO_2 transportation. Most important of them is that CO_2 has to be transported in a supercritical phase. Table 2.2 shows common parameters and their values for pipeline CO_2 transportation. According to Mercedes [67], pressures above 8.6 MPa should be used to avoid changes in compressibility. Due to pressure drops in the pipeline, compressor booster stations are suggested every 150-300 km. This also allows the use of lower diameter pipes, which means a significantly lower cost of the transportation.

Table 2.1: Overview of CO₂ capturing methods. Modified after: [72]

Method	Description	Advantages	Disadvantages
Adsorption	Gas mixture in a direct contact with a porous material (carbon, zeolites, silica gels). CO ₂ captured on the solid surface. Released by changing the temperature or pressure.	Lower energy requirements for regeneration	Low adsorption capacity and slower kinetics. High initial capital cost.
Absorption	Gas mixture in a direct contact with a liquid phase (MEA, MMA, DEA). CO ₂ chemically bound to the scavengers. Released by change of temperature or pressure.	Plenty of solvent options, process needs less energy.	Degradation of solvents, high energy consumption for regeneration. High initial capital cost.
Membranes	Only molecules of the size of CO ₂ are able to pass the membrane in a pressurized gas stream. Common membranes used are inorganic or polymer membranes.	No energy consumption, no regeneration needed. Lower capital cost.	Only applicable for a certain size of molecules for selective permeability.

2.2.3 CO₂ Injection

CO₂ injection is the third part of the CCS process and is probably the most important of them. One of the significant parameters when injecting CO₂ into formation is the injection pressure. According to Espinoza *et al.* [32], it must exceed the fluid pressure that is present in the reservoir, but not exceed the fracture stress gradient. When CO₂ is injected for CCS purposes into the depleted reservoir, it will displace the water that is present in the reservoir. Additionally, buoyancy of CO₂ will create a difference in pressure that is equal to $\Delta P = (\rho_w - \rho_{CO_2})gh$ [32]. This is depicted in Figure 2.5. This gradient pressure is proportional to the height of CO₂ plume and the difference of densities. In oil and gas industry, the displacement of water is called a drainage process. The drainage of water is controlled by

Table 2.2: Common parameters and their values for a CO₂ transportation pipeline. Modified after: [67, 6]

Parameter	Value	Unit
Inlet pressure	152	bar
Min. outlet pressure	103	bar
Pressure drop per unit length	49	Pa/m
Average CO ₂ temperature	25	°C
Average CO ₂ density	884	kg/m ³
Average CO ₂ viscosity	6.06 x 10 ⁻⁵	N-s/m ²
Pipeline length	100	km

various parameters, most significant of which are the relative permeability curves. When the injection of CO_2 stops, the water that was draining out will start imbibing back into the plume of newly injected CO_2 . [18] In this chapter, some of the important aspects that influence CO_2 injection will be discussed.

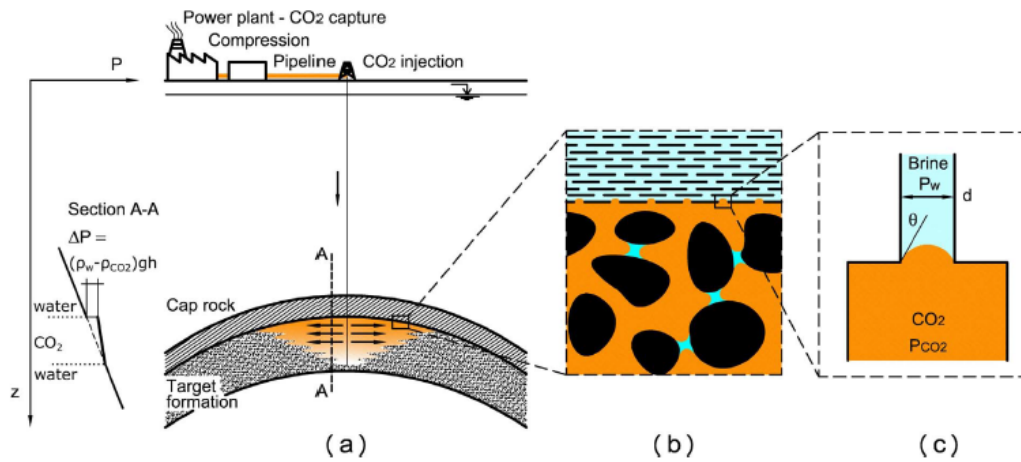


Figure 2.5: (a) Depiction of a fossil plant that has the required technology to capture, compress and transport CO_2 to the injection area, where CO_2 is injected beneath the caprock. (b) Depiction how the capillary menisci trap the free CO_2 . (c) Capillary tube analogy showcasing the water-wet case. Source: [32]

Trapping of CO_2

It is important to realize that there exist four different types of trapping mechanisms of CO_2 , depending on how much time has passed since the initial injection [79, 53]:

1. structural, which originates from tectonic forces and create physical obstacles to the flow;
2. residual (capillary) trapping, which is the CO_2 that is trapped in the pores by capillary forces as the CO_2 is injected. According to Al-Menhali *et al.* [53], this is the most effective and fastest trapping mechanism;
3. solubility trapping occurs because of absorption and adsorption of CO_2 in the formation. Some authors [3] claim that this is one of the most important trapping mechanisms;
4. mineral trapping is relevant after a significant amount of time (thousands of years) has passed since the injection, then CO_2 will interact with the minerals that are present in the formation, thus forming carbonate minerals.

Effect of Pressure and Temperature on CO_2

When injecting CO_2 into formation, we need to take into account the fact that the aquifer will be hosting an aqueous solution (saline H_2O). Important parameters

to consider during the CO₂ injection is the pressure and temperature in the formation, but also the conditions of CO₂ that is injected. Essentially, to understand what happens in the formation during injection and storage, additionally to examine the success of the CCS process, the thermodynamic behaviour of CO₂-H₂O (mutual solubility, reaction path modelling, dissolution etc.) has to be studied, but this is not the main scope of our thesis. Some analysis of solubility is however carried out in the next section.

As can be seen in Figure 2.7, CO₂ has a triple point around -56.6 °C and 5.2 bars and critical point around 31 °C and 74 bars. Other authors [69, 52] confirm these values. CO₂ differs from HC gases in a way that it has a strongly non-linear variation of physical parameters. According to Hurter *et al.* [46] for the pressure difference of 80 to 90 bars at 35 °C, the viscosity and density of CO₂ will change by a factor of 2 (in case of methane, the properties would change by a few percent only). The density of CO₂ as a function of geothermal and hydrostatic gradient is shown in Figure 2.6. This reference will serve as a basis for the density estimation in the storage capacity calculation in Chapter 5.6.5 of the thesis.

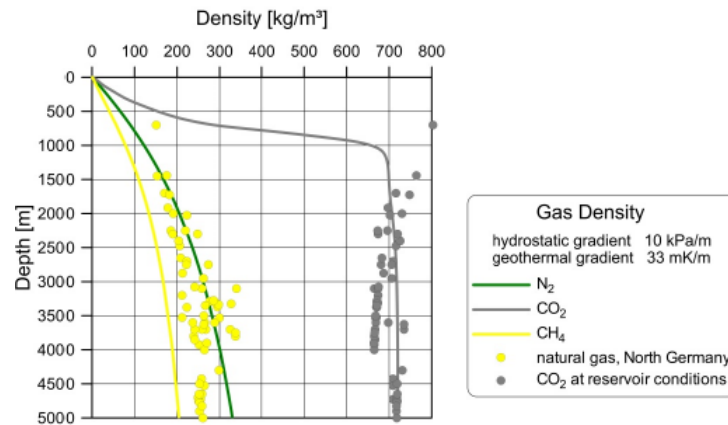


Figure 2.6: CO₂ density as a function of hydrostatic gradient. Source: [8]

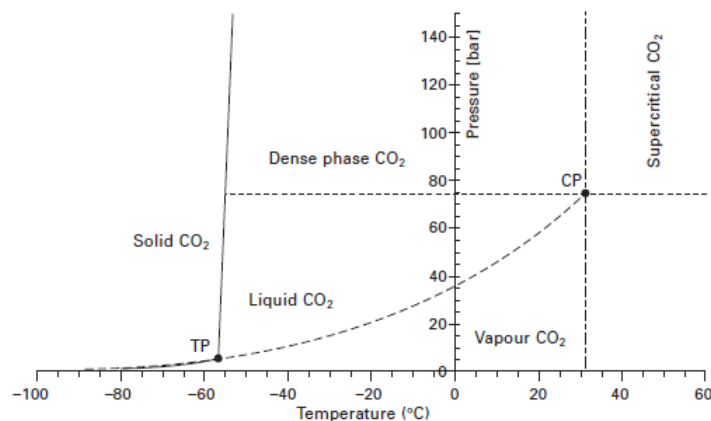


Figure 2.7: Phase diagram of CO₂. Source: [67]

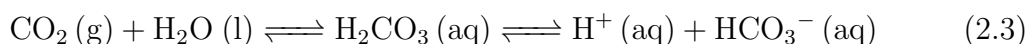
Effect of Solubility and Mineralisation Reactions

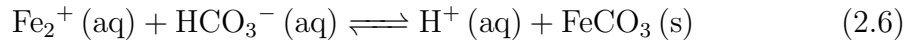
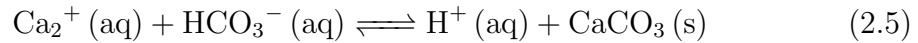
Compared to other hydrocarbon gases (e.g. methane), the solubility of CO₂ in water is much higher: in the range of 50-150 °C and 100-1000 bar, the solubility of CO₂ in brine is approximately 15-60 sm³/sm³ [77]. Solubility increases with pressure and decreases with temperature. Thus, the solubility in the formation water is a significant term that has to be taken into account. As mentioned by Valbuena *et al.* [73], effect of solubility is negligible in the initial stage of injection, meaning that this effect requires a significantly wider span of time to occur.

In the scope of our thesis, the solubility modelling was implemented by using the online calculator made by Duan and Sun [30], which is applicable in the pressure range of 0 to 2000 bar, temperature range of 273 to 555 K and ionic strength range of 0 to 4.3 M and is based on specific particle interaction theory and equation of state developed by Duan [12]. The results of that modelling are presented in Chapter 5.3.

Mutual solubility between CO₂ and water will impact the injection in three main ways [46]: (i) dissolution of CO₂ in the water will increase its density, (ii) dissolution of CO₂ will form carbonic acid (this leads to corrosion in injector wells), (iii) water dissolves into CO₂ and that will increase salinity of the water, by means of the so-called "dry-out" and "salting-out" effects. "Salting out" effect is the byproduct of "dry out" effect and in other words it can be regarded as scaling, because of the precipitating salts. This is important to consider because it decreases the permeability and porosity [46]. Some authors [55] mention that depending on depth and the salt concentration in the brine, approximately 25-60 kg CO₂ per 1 m³ of formation fluid can be dissolved.

As was described earlier, CO₂ trapping is divided into four equally significant parts, starting from the method that takes the least time: (i) structural (also called hydrodynamic or stratigraphic), (ii) capillary, (iii) solubility and (iv) mineral trapping. As the trapping mechanism changes its type, the storage security increases (thus, mineral trapping is the most secure type of storage, but it takes time). In case of mineral trapping (mineralisation), a number of reactions are taking place, which eventually lead to a safe and long storage of CO₂. Reaction 2.3 illustrates the dissolution of CO₂ in the formation water to form carbonic acid, and immediately dissociating and forming bicarbonate. Consequently, reaction 2.4 depicts how the bicarbonate reacts with the cations present in the formation water, which leads to forming stable carbonates (magnesite, calcite and siderite in reactions 2.4 to 2.6, respectively). [43]





Reservoir Properties Affecting Injection

There are various reservoir parameters that affect the storage of CO₂. Most prominent of them are: reservoir heterogeneity, relative permeabilities, natural fractures and reservoir fluids [37].

Reservoir heterogeneity affects the performance of injected CO₂ in a way that the formations with higher vertical permeability (e.g. naturally fractured reservoirs) are influenced by the cross-flow perpendicular to the bulk flow. This is influenced by the viscous, capillary, gravitational and dispersive forces. [48]

Relative permeability is a significant petrophysical property that has an effect on wetting and saturation characteristics of a particular phase. In fact it is one of the key properties that describes how CO₂ is moving in the subsurface [18]. In order to predict the flow of two distinct phases, the fractional flow curves have to be made using the empirical relative permeability correlations [45]. In the scope of our thesis, relative permeability is regarded as the effective permeability of the brine and the CO₂, describing how the flows affect each other. Important aspects of post-CO₂ injection such as the extent of capillary trapping, seal integrity, shape and size of the CO₂ plume is predominantly a function of relative permeabilities [18].

Fractures and faults in the reservoir influence the permeability. According to Garcia [37], fractures can either increase or decrease the permeability, which will mean that there will be a permeability anisotropy in the reservoir. Although the knowledge of location of faults and fractures is significant, it is complicated to accurately predict them.

2.2.4 Risks Regarding CO₂ Injection

CCS technology has many risks that need to be addressed when planning an economically and technically viable CCS project. According to Rouzbeh *et al.* [79], the most critical thing is to select a good caprock, that would not have faults or cracks and a very low permeability. In the opposite case (if the injection pressure exceeds the pressure that the caprock can withstand) CO₂ will flow to the surface and this is not desirable [76]. Various authors [75, 25, 38] mention that most of the problems are likely to occur during the operational stage, and once the injection is finished, the risk drops. The risks can generally be divided into five main groups [25]:

1. CO₂ leakage - CO₂ leaks out through subsurface to the atmosphere;
2. CH₄ leakage - injection of CO₂ might cause CH₄ to escape into atmosphere, as well (assuming the reservoir is not depleted);
3. seismicity - earth tremors caused by the injection operations;
4. ground movement - caused by the pressure changes while injecting CO₂;
5. displacement of the brine - brine will move into other formations.

Most of the research is done for the first type of the risk, which is the CO₂ leakage possibility.

Caprock Failure

Depleted oil and gas reservoirs are considered to be very good candidates for CCS operations, because (i) the reservoir behaviour, geophysical, geomechanical and other properties have been studied properly and (ii) the reservoirs have withheld the hydrocarbons for long periods of time without significant releases to other formations or surface.

For these types of reservoirs, there are still two options through which the CO₂ leakage could occur [25]: (i) caprock failure and (ii) escape of CO₂ along the injection well. The first one of them is more applicable in the scope of our thesis, so it will be discussed in this section.

Caprock failure is a term that encompasses various mechanisms that could eventually lead to the failure of various fluids in the reservoir. Some of the most important mechanisms are concluded in the following list [25]:

- diffusion (concentration difference) of CO₂, which is regarded as a very slow process, but which can lead to significant releases in the long run;
- capillary leakage, which may be a big problem if the pressure difference of the CO₂ and water in pores is bigger than the capillary entry pressure (CEP) of the caprock. This mechanism is also considered of low importance, since the CEP is historically (during the production time and before depletion) high enough to retain the hydrocarbons and then CO₂. CEP of the caprock can be measured and pore pressure threshold calculated to avoid that hazard [44];
- leakage due to man-induced fractures, which are generally known as hydraulic fractures. The fluctuations in pressure in the reservoir may cause the caprock to fracture, as well. This can be avoided if the maximum injection pressure is kept below the fracturing pressure;
- seismic activity may cause fractures in the caprock that leads to the leakage of CO₂;

- dissolution of the caprock when CO₂ reacts with the caprock minerals. CO₂ can dehydrate the shale and increase the permeability of the caprock;
- CO₂ leak through faults that are present in the caprock. This can be mitigated if a thorough geological analysis of the area is performed.

Once the fluid is injected into the reservoir, the pressure will increase and the effective stresses decrease. According to Khan *et al.* [10], this can cause series of different scenarios, some of them include: (i) increase in overburden stress; (ii) decrease in effective stress can reactivate the fractures and/or faults; (iii) high-rate injection can cause fractures. According to Pan *et al.* [9] main modes of failure in the caprock are the tension or shear of the rock, re-shearing of faults and opening of new fractures. In case of the reactivation of faults, seismic events can occur. All of these cause significant threat for a secure storage of CO₂.

2.2.5 Selection of the Injection Site and Wells

There exist three main considerations when selecting a site (or wells) for a successful CO₂ injection: (i) injectivity, (ii) containment and (iii) capacity. They will be discussed in this section.

Injectivity is a significant part of the well-selection algorithm and it addresses mainly pressure and flow related concerns. According to Vishal [75], key properties regarding injectivity are porosity and permeability. Large porosity will provide a sufficient amount of volume for CO₂ storage and high permeability is positively correlated with good injectivity. However, low permeability sections will reduce the injectivity due to the fact that the pressure will increase in the location of the injection, thus slowing down the injection process and putting at risk the integrity of caprock. Injectivity can be increased by using multiple wells and/or by drilling directional wells [28].

Second important aspect of the assessment criteria is that of CO₂ containment. It is mostly connected to the properties of the overlying caprock and its integrity, which will be discussed thoroughly in Chapter 4.1, however the most important aspects of the caprock are, according to some authors [28], its thickness, lateral continuity, low vertical permeability and high capillary entry pressure. According to Mercedes [67], a good site selection should involve a dynamic flow modelling to account for the risk of possible leakage or fracturing. Such risks are regarded as global risks. Additionally, local risks exist that predominantly account for HSE issues like flux of CO₂ to shallower formations and consequently to atmosphere, chemical dissolution of CO₂ in the subsurface and effects of the displacement that will be caused by the injected CO₂ [75].

Thirdly, before an industrial scale injection can commence, the effective capacity of CO₂ must be evaluated. According to Delprat *et al.* [28], the storage capacity in the reservoir is a function of a number of properties, most important of which are pore size and shape of the rock, grain mineralogy, reservoir petrophysical properties, fluids that are present in the reservoir and others. Because the pore

volume cannot be filled completely with CO₂, efficiency factor (EF) has to be implemented, which will result in the estimation of effective capacity. The value of EF varies greatly, mostly depending on the type of lithology and the fluids present in the reservoir.

Most important screening criteria of the site selection is presented in Table 2.3, based on work performed by Chadwick *et al.* [5].

Table 2.3: Main positive and negative indicators for CO₂-injection site selection. Modified after: [5]

Criteria	Parameters affected	Positive Indications	Cautionary Indications
Depth of the reservoir	Temperature Pressure Permeability Porosity	Top of reservoir >1000 m Base of reservoir <2500 m	Top of reservoir <800 m Base of reservoir >2500 m
Reservoir properties	Permeability Porosity Salinity	>500 mD >20 % >100 g/L	<200 mD <10 % <30 g/L
Geology	Stratigraphy Caprock thickness Faults	Uniform distribution >100 m No faults	Lateral variations <20 m Faults
Other	Static storage capacity	Capacity significantly higher than the amount of CO ₂ to be injected	Amounts of CO ₂ to be injected and storage capacity of similar magnitude

2.2.6 CO₂ Storage Capacity Theory

In order to quantify how much CO₂ can be injected into subsurface, analysis of the storage capacity has to be carried out. In the scope of our master thesis, the methodology of Bachu *et al.* [11] was implemented, which does not take into account the dissolution of CO₂ nor mineral precipitation, so it is a purely stratigraphic (volumetric) type of capacity estimation. Important assumption in such calculation for oil and gas reservoirs is that the volume that was previously occupied by hydrocarbons is now accessible to CO₂. This assumption is valid for pressure depleted reservoirs. It provides a capacity indication based on the volumetric estimation of depleted oil and gas reservoirs. Another assumption is that CO₂ will be injected until the initial pressure of the reservoir is restored. If this criteria is not met, it can significantly reduce the integrity of the caprock. This method is based on Equation 2.7. The results of this calculation are presented in Chapter 5.6.5.

$$M_{CO_2} = \rho_{CO_2res} \times R_f \times A \times h \times \phi \times (1 - S_w) - V_{iw} + V_{pw} \quad (2.7)$$

where M_{CO_2} is the mass of CO_2 that can be stored [kg], ρ_{CO_2res} is the density of CO_2 at reservoir conditions [kg/m^3]; R_f is the recovery factor; A is the areal extent [m^2]; ϕ is the porosity of the reservoir [v/v]; S_w is the water saturation of the reservoir [v/v]; V_{iw} is the volume of injected water [m^3] and V_{pw} is the volume of produced water [m^3]. According to Bachu *et al.* [11], V_{iw} and V_{pw} terms are negligible in case of strong water drive reservoir, which is the case for Tensleep formation.

Volume Calculation

In order to implement Equation 2.7, where $A \times h$ symbolises the volume calculation, which is the predominant factor in the equation, several values have to be calculated. Key one of them is the GRV part in STOIIP formula, since Equation 2.7 assumes that depleted HC volume is now available for CO_2 . Formula for STOOIP is shown in Equation 2.8.

$$STOOIP = GRV \times NTG \times \phi \times S_o \times \frac{1}{B_o} \quad (2.8)$$

where STOOIP is the stock-tank oil initially in place (Sm^3); GRV is the gross reservoir volume (computed in Petrel); NTG is the net-to-gross ratio (v/v); ϕ is the porosity (v/v); S_o is the oil saturation (v/v); B_o is the oil formation volume factor (RB/STB).

Petrophysics

3.1 Reservoir Properties

3.1.1 Porosity

Porosity is defined as the ratio between the the volume of void spaces in a rock and the total bulk volume of the rock. These values are commonly expressed as percentages and are calculated using Formula 3.1:

$$\phi = \frac{\text{Pore volume}}{\text{Total volume}} \times 100 \quad (3.1)$$

Generally porosity can be defined as either total porosity or effective porosity. Total porosity indicates a ratio between the total pore volume inside the rock and the total bulk volume of rock. Effective porosity illustrates the ratio between the interconnected pore space and the the total bulk volume. Thus, the effective porosity does not include voids that are completely isolated within the rock. [19] The difference is depicted in Figure 3.1. Primary porosity in sandstone reservoirs is a function of grain size, packing and sorting of the sediment [14]. There are three ways to measure the porosity of the rock [47]:

1. by inspecting the well cuttings that are brought up with the drilling mud using the binocular microscope;
2. by analyzing the coreplug with the porosimeter;
3. by running a wireline log (formation density, neutron porosity or sonic logs; more information about different types logs are presented in Appendix A).

In the scope of our master thesis, the porosity was determined with the wireline logs.

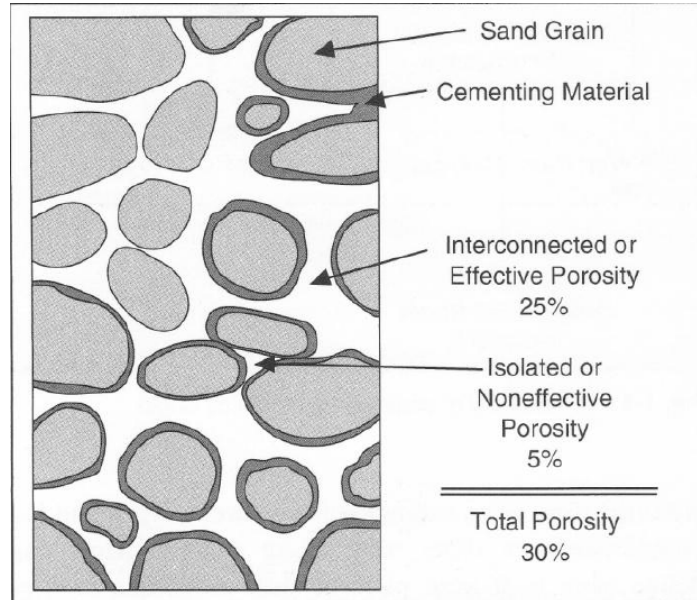


Figure 3.1: Depiction of effective and total porosity within the rock. Source: [19]

3.1.2 Water Saturation

Water saturation is the water fraction inside a specific pore volume. It is important to understand that the water (and oil) saturation is based on pore volume, and not on gross reservoir volume [71]. Saturation value is used to determine the content of oil in the pore and it is normally expressed as volume to volume or in percentage units. There are different types of water saturation that have to be distinguished [71]:

- critical water saturation S_{wc} (also called connate water saturation or irreducible water saturation) is the maximum water saturation at which the water will be immobile, which means it is the lowest water saturation that will be present after the oil or gas has displaced the remained water in the core plug;
- initial water saturation is the saturation that is present in the reservoir before any engineering activities;
- effective water saturation, which is defined as:

$$S_w^* = \frac{S_w - S_{wc}}{1 - S_{wc}} \quad (3.2)$$

where S_w is the water saturation, S_{wc} is the critical water saturation (connate).

There are various methods to calculate water saturation from resistivity logs, however the most common method is the Archie model, which was used in scope of our work. It is a model that was first introduced in 1940s by Archie and Leverett [50]. Archie model takes the resistivity of the rock, which is a function

of the amount and distribution of hydrocarbons and water, and the resistivity of water. It is shown in Equation 3.3 :

$$S_w^n = \frac{aR_w}{\phi^m R_t} \quad (3.3)$$

where a is the tortuosity constant (determined by connectivity of the pore spaces of the rock); R_w is the formation water resistivity; R_t is the true formation resistivity; ψ is the porosity; n is the saturation exponent; m is the cementation factor. According to Liu [50], a is in the range of 0.5-1.5, n is around 2 and m is the range of 1.3-2.6. These constants are strongly dependant on the properties of the rock itself. [19, 40]

3.1.3 Permeability

Permeability describes how easily the fluid can flow through connecting pore spaces within the reservoir rock. Fluids are conducted from the pores towards the borehole and it is the most important parameter when predicting the production rates. Permeability is highly dependent on the size of pore openings, pore connectivity and the type of cementing material between the rock grains. In siliclastic¹ rocks permeability is a function of (i) pore throat size and (ii) the number of the pores that are connected to each other [14].

The calculation of permeability was developed based on laboratory flow tests performed by Henri d'Arcy. He developed the following Equation 3.4 for the permeability calculation [19]. The unit of permeability is usually darcy (D) or millidarcy (mD).

$$k = \frac{Q}{A} \times \frac{\Delta P}{L} \quad (3.4)$$

where k is the permeability (D), Q is flow rate (cm/s), μ is the viscosity of the fluid (cP), A is the cross section of the rock (cm^2), L is the length of the rock (cm), ΔP is pressure drop (psi).

The only way to measure the permeability in laboratory is by drilling a core beforehand and then cutting a plug to analyze it with a tool called a permeameter. It measures how much air or nitrogen (N_2) flows through the plug. Typical values of permeability in an oil reservoir can be seen in Table 3.1.

In the scope of our thesis, Coates' method was implemented in Techlog[®]. It is based on the following inputs: effective porosity, total porosity and irreducible water saturation. The formula satisfies the condition of zero permeability at zero porosity while formation must be at irreducible water saturation [17]. Coates' equation for clean and not clean zones are shown in Equations 3.5 and 3.6, respectively:

¹Silica bearing non-carbonate sedimentary rocks.

Table 3.1: Typical values of permeability for an oil reservoir. Modified after: [47]

Value of permeability (mD)	Quality
1-10	Bad
10-100	Good
100-1000	Excellent

$$k = k_c \times \phi_{eff}^4 \times \left[\frac{1 - S_{wirr}}{S_{wirr}} \right]^2 \quad (3.5)$$

$$k = k_c \times \phi_{eff}^4 \times \left[\frac{\phi_t - \phi_{eff} \times S_{wirr}}{\phi_{eff} \times S_{wirr}} \right]^2 \quad (3.6)$$

where k is the calculated permeability (mD), k_c is Coates constant (unitless; default value 650), ϕ_{eff} is effective porosity (v/v), ϕ_t is total porosity (v/v), S_{wirr} is irreducible water saturation (v/v; value used 0.2).

3.1.4 Volume of Shale

It is important to calculate the volume of shale present in the reservoir, since shale has a significant effect on the response of most of the logging tools. Shale contains water that affects the true resistivity values of the formation, thus making the calculation of water saturation less accurate. Besides water saturation shale also affects the accuracy of porosity and permeability values. Because of this, it is crucial to calculate the values of water saturation, porosity and permeability taking into account the volume of shale. [20]

Generally, it is assumed that all the clay that is present in the reservoir is the same as they clay that is in the shale. If the volume of clay is more than 15% the formation can be named *shaly*. Shale itself can be distributed within the formation as different types, such as: (i) structural shale - where the shale grains replace some of the sand grains; (ii) laminar shale - where thin layers of shale are present in the matrix; (iii) dispensed shale - where the clay minerals fill in the inter granular space [20]. Wireline logs like GR and SP help identifying formation zones containing shale and allow the calculation of shale volume.

For the purposes of this project, GR log was used for the calculation of shale volume and the NTG (net-to-gross). NTG depicts the proportion of the gross rock volume that is formed by the reservoir rock (scale from 0 to 1). It can also be defined as the proportion of the rock that can store the hydrocarbons. The quantitative evaluation of shale data using GR assumes that no radioactive minerals other than clay are present. The gamma ray shale index (IGR) is calculated with the following formula:

$$IGR = \frac{GR - GR_{cn}}{GR_{sh} - GR_{cn}} \quad (3.7)$$

where GR is the log response zone of interest; GR_{cn} is the log response zone in the "clean", shale free zone; GR_{sh} is the log response zone in the shale bed.

With the calculated IGR index, there are two ways to find the shale volume. First method requires a good knowledge of the area and clay content, allowing to make a linear correlation from IGR to the fractional volumes of shale. Second method is much more common as it provides a good estimate of shale volume in a nonlinear way, by the application of the Stieber relationship [20]:

$$V_{sh} = \frac{0.5IGR}{1.5 - IGR} \quad (3.8)$$

where V_{sh} is the shale volume and IGR is the the gamma ray index.

After which NTG can be calculated as follows:

$$NTG = 1 - V_{sh} \quad (3.9)$$

where NTG is the net-to-gross ratio (dimensionless); and V_{sh} is the volume of shale (v/v).

Geomechanics

Geomechanics is the study of how the soil and rock deform due to different environmental parameters such as temperature, pressure and stress. In scope of our thesis (but also in petroleum industry in general), geomechanics is more concentrated on the rocks. The study of geomechanics is applied within the whole scope of a petroleum field: starting from exploration to production to abandonment.

Geomechanics as an engineering field has become more and more significant over the last decades due to the growth of the unconventional oil and the necessity to, for instance, fracture the reservoirs (creation of artificial permeability). These procedures rely predominantly on geomechanical knowledge [1]. Additionally, rock mechanical properties play a crucial role in the prediction of fractures and the study of wellbore stability [7].

In our work, the following geomechanical properties of the caprock were investigated: pore pressure, fracture gradient, elastic properties and rock strength properties. They are theoretically described in the following sections.

4.1 Caprock Overview

Caprock is the main component when it comes to storage part of the CCS process. It is defined as low or very low permeability formation (in the range of μD to nD) and usually low porosities (less than 15%) [34]. The effectiveness of the caprock defines the storage capacity of carbon dioxide, so it is of utmost importance to analyze various caprock properties.

The main issue with the caprock is the upward buoyancy driven force of the injected CO_2 that keeps accumulating as the injection is taking place. If the excess pressure overcomes the tensile and critical pressures of the caprock, it might succumb to mechanical failure, resulting in hydraulic fractures that with increase the loss of CO_2 . According to Fleury *et al.* [34] there are multiple mechanisms that are responsible for CO_2 migration in the caprock. Most notable of them are presented as follows:

- flow of CO_2 through already existing fractures in the caprock;

- molecular diffusion of CO₂ from the reservoir zone into the caprock (some authors [21] consider this only a rate-determining mechanism, and not an actual mechanism that affects the loss of caprock sealing capacity);
- chemical alteration of the mineralogy of the caprock with the acidized water;
- old fractures re-opening due to the overpressure;
- combination of these processes.

Caprock's potential (ability to confine CO₂) is influenced by multiple factors: permeability, seal capacity, seal geometry, seal integrity. According to Fleury *et al.* [34], permeability and thickness of the caprock are the most important parameters which have to be used to choose a caprock for storage purposes. Some of the parameters are discussed in depth in the following sections.

Seal Capacity

Seal capacity is the maximum column height of CO₂ that the caprock can withstand before the capillary forces will allow the migration of CO₂. It is effective through the rock pore size, the upward pressure of CO₂, the capillary pressure of the pores, wettability and the interfacial tension between the phases. Capacity of the seal is therefore a function of the interaction between the rock, water and CO₂. Several authors [21] have reported that there is an effect of dissolution and precipitation on the rock matrix that will influence the permeability. It was reported, however, that it is complicated to analyze these effects in the laboratory, because of a different span of time than would be expected in an actual caprock. Cinar *et al.* [23] mention that the storage capacity is predominantly dependant on porosity, aquifer volume and microscopic displacement efficiency.

Important parameter regarding the seal capacity is the capillary entry pressure. According to Fleury *et al.* [34] capillary entry pressure (threshold) *"is the minimum pressure difference between gas and water necessary for the gas to enter the porous media."* This property is controlled by size of caprock pores, CO₂-supercritical water IFT and the wettability state of the CO₂ to rock when there is also water present [65]. Figure 4.1 shows the contact angles between the different phases present in vicinity of the mineral substrate (rock-brine-CO₂). CO₂ can escape from the sealing formation if the so-called threshold (breakthrough) pressure is exceeded [21]. This threshold pressure is shown in the Equation 4.1 and it depends on pore radius r , water-brine interfacial tension γ and contact angle between brine-CO₂-mineral θ :

$$P_c = \Delta P = \frac{2\gamma \cos\theta}{r} \quad (4.1)$$

It has to be mentioned that usually the system of caprock and reservoir is assumed water-wet (over half of the mineral surface is wetted by water and smaller pores are occupied). However, lately many studies have been carried out that show

that reservoirs can be either oil-wet or CO₂-wet, which will change the state of wettability. Additionally, there exists a possibility of miscibility between the phases of CO₂-supercritical water. This will lead to full wetting (as seen in Figure 4.1). [65]

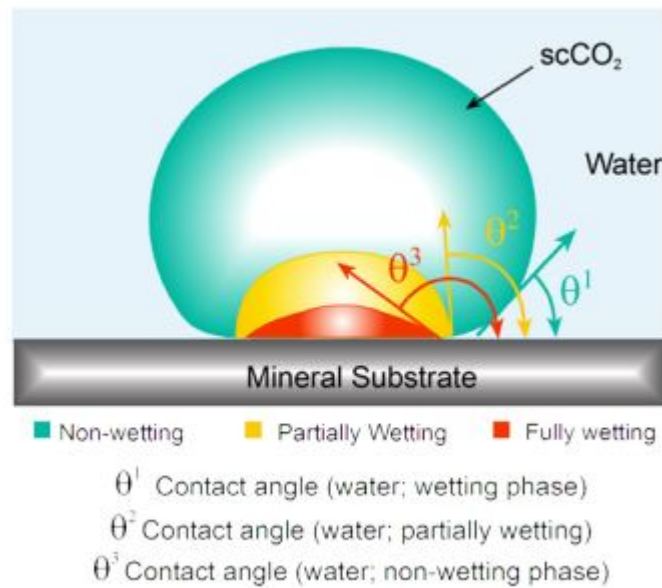


Figure 4.1: Wettability states between supercritical water, mineral substrate and CO₂. Source: [65]

Seal Geometry

Geometry of the caprock depends on the thickness, structural and areal position (extent) of the caprock itself. This information is found using seismic data, well correlations, geological relationships etc. To have an effective seal, it is of utmost importance to have a caprock that extends over the equal or greater area of the reservoir.

Seal Integrity

Seal integrity is the ductility¹ of the rock and is one of the main factors when it comes to evaluating the caprock. According to IEA² report [65], seal integrity is *"a function of lithology, pre-existing planes of weakness, regional stresses and orientation/magnitude of induced stresses from injection and storage"*. Higher ductility means that the lithology can withstand more stress, providing a more effective caprock for a CCS process. Most of the time the seal integrity can be compromised by factors such as rock fatigue, increase of pore pressure, tensile stress, or just complete rock failure when shear stress is reduced. The effectiveness of the caprock is also influenced by factors as: lithology, ductility, thickness, burial depth.

¹Ductility is a measure of the materials ability to withstand deformation.

²International Energy Agency.

Lithology

Lithology of the caprock is of vital importance because of the possibility that the injection of CO₂ and its interaction with brine will alterate the rock-matrix. Problems would be caused by minerals that can be dissolved by acidic CO₂-brine solution. This type of dissolution of caprock may affect the general sealing properties due to the presence of soluble mineral phases. [41]

Ductility

As mentioned earlier, ductile caprocks are less prone to faulting and fracturing (compared to brittle caprocks). The higher the ductility, the better it will withstand the pressure changes during injection and storage processes of CO₂. Examples of the relationship between ductility and lithology type can be seen in Table 4.1. The most ductile lithologies are evaporites and least ductile lithologies cherts. Ductility is a function of temperature and pressure. For example, evaporites may be brittle at shallow depths but ductile as they are buried deeper. [14]

Table 4.1: Change of ductility for different lithologies. Modified after: [24, 14]

Lithology type	Ductility
Chert	Low  High
Sandstone	
Carbonate cement	
Dolomite	
Anhydrite plugged	
Sandy shale	
Calcereous mudstones	
Silty shale	
Shale	
Organic-rich shale	
Anhydrite	
Halite	

Thickness

Although the thickness of the caprock can vary from tens to hundreds of meters, it is still crucial that it is as thick as possible. Thicker caprock prevents horizontal leakage and acts as a lateral seal. According to IEA report [65], thickness has no significant effect on capillary entry pressure, although thinner caprocks are usually more prone to faults and other sedimentary discontinuities.

Burial Depth

According to Allen *et al.* [14], burial depth does not appear to be a significant factor in terms of caprock effectiveness. Authors mention that almost 50% of recoverable oil reserves are present in depth region of 1000m to 2000m, and 31% of the reservoirs deeper than 2000m, thus they concluded that the caprocks may be effective at a wide range of depths. For example, Duri field (Sumatra basin, Indonesia) is at 100 meters below surface and has an effective shale seal above it.

4.2 Pore Pressure

Pore pressure analysis is a significant aspect in the exploration part of the field. The analysis is required to create a pore pressure map, which will greatly help to avoid possible blowouts, kicks and fluid influxes. If log readings are carried out while drilling, the differences in pore pressure can affect the quality of the log measurements.

The relationship between pressure and depth illustrating different types of pressures is shown in Figure 4.2. As can be seen, the normal pressure is called the hydrostatic pressure, which is the other name for the pressure that is exerted by the vertical column of water above. Typical HS pressure gradient is 0.465 psi/ft (0.03206 bar per 0.3048 m) [33]. Normal pressure (HS pressure) is calculated with the following formula:

$$P = \rho gh \quad (4.2)$$

where P is the hydrostatic pressure [Pa]; g is gravity acceleration [m/s^2]; ρ is the density of water [kg/m^3], h the height of the water column [m].

Overburden (lithostatic) pressure is the sum pressure of all the fluids and rocks that are above. It is calculated with the following formula:

$$P(y) = g \int_0^z \rho(y) dz \quad (4.3)$$

where $P(y)$ is the pressure as a function of depth, $\rho(z)$ is the density as a function of depth, g the gravity acceleration and y the depth.

According to Holstein and Lake [45], pore pressure can be approximated as the difference between overburden pressure and the vertical rock stress. It can be calculated using various methods. Most prominent are Eaton, Bowers and Traugott methods using sonic, seismic or resistivity logs. [33]

As can be seen from Figure 4.2, using the previously mentioned pressure types it is possible to derive two important parameters: overpressure and effective stress.

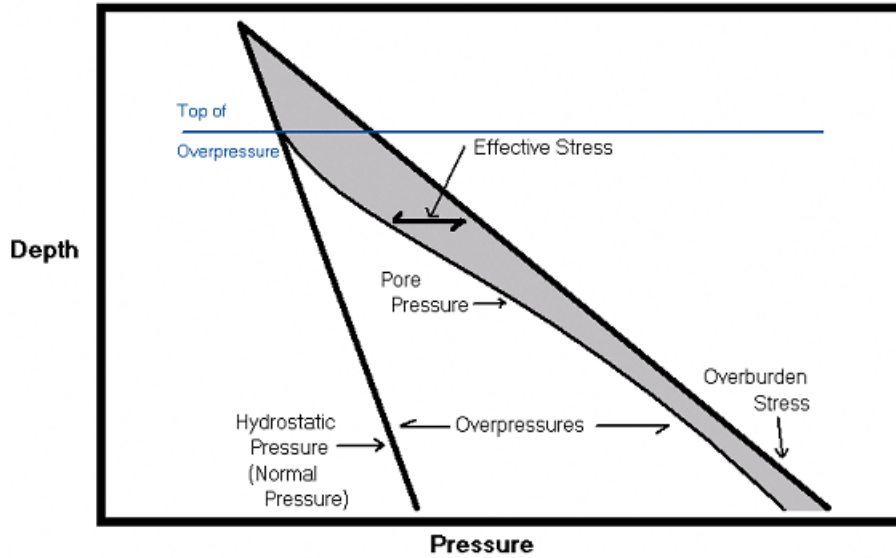


Figure 4.2: Depth vs pressure, different types of pressure and depiction of effective stress. Source: [33]

First one is defined as the difference between pore pressure and normal pressure (HS-pressure) and the effective stress is the difference between overburden pressure and pore pressure. Results for the pore pressure calculations are presented in Chapter 5.5.1.

4.3 Fracture Gradient

Fracture gradient (FG) is one of the inelastic properties (along with formation strength, which will be discussed later) that are related to the mechanical properties of the rock. These properties have to be determined in order to reduce drilling risk (drilling mud design) and maximise oil production from the well. FG can generally be understood as the pressure that will cause fractures in the rock at a certain depth of interest. [45] There are several published mathematical expressions in order to quantify and determine the FG. These include Matthews & Kelly, Eaton, Goldsmith & Wilson, Costley and others. [31]

In the scope of the current thesis, the Eaton approach was implemented. All the FG calculation methods implemented in Techlog[©] were based on the following equation:

$$FG = K \times (\alpha_v - \alpha P_p) + \alpha P_p \quad (4.4)$$

where α is the Biot coefficient³, K is the stress ratio (unitless), which is the horizontal effective matrix stress over the vertical effective stress.

³From Techlog[©] glossary: poro-elastic parameter of rock, which describes how compressible the dry skeletal frame is with respect to the rock matrix.

Different methods for the calculation of FG differ in how the "K" parameter is determined. For our case, Eaton method was of interest. It is based on the following relationship:

$$K = \frac{v}{1 - v} \quad (4.5)$$

where v is the effective Poisson's ratio in shale (Poisson's ratio will be discussed in the following chapter). Results for fracture gradient calculations are presented in Chapter 5.5.2.

4.4 Elastic Properties

Mechanical properties of the rock include the following elastic properties: shear modulus, Young modulus, Poisson's ratio and bulk modulus. They are calculated based on the well logging data and are used to characterize the caprock. They describe how the properties act under certain stress and whether or not the material can fail [68]. This chapter will briefly describe the theory behind each of them. Table 4.2 shows the general relationships (formulas) for the mentioned elastic properties.

Shear Modulus

Shear modulus (also called modulus of rigidity) is applied when a deformation is taking place parallel to one face of the object, while the opposite face of the object is held fixed by another equal force. It is the ratio between shear stress and shear strain. Units are in regular pressure units (e.g. Pa). Bigger shear modulus means bigger rigidity of the material.

Young's Modulus

Young's Modulus (also called elastic modulus) is the ratio between the longitudinal stress of cross section to longitudinal strain. Materials with high Young's modulus are considered rigid. Units are in regular pressure units (e.g. Pa). This ratio is shown in Figure 4.3, where Young's modulus is the slope. [26]

Poisson's Ratio

According to Techlog[©] glossary, Poisson's ratio is an elastic constant that is a measure of the compressibility of material perpendicular to applied stress, or the ratio of latitudinal to longitudinal strain; as shown in Table 4.2. When a material undergoes deformation (stretching), the strain is negative; in case of

Table 4.2: Geomechanical properties and their formulas with nomenclature. Modified after: [24]

Elastic Property	Formula	Nomenclature
Stress	$\sigma = \frac{F}{A}$	σ - stress; F - force; A - area
Strain	$\epsilon = \frac{\Delta L}{L}$	ϵ - strain; ΔL - longitudinal change; L - longitude
Poisson's Ratio	$\nu = \frac{\epsilon_{transverse}}{\epsilon_{axial}}$	ν - Poisson's ratio; $\epsilon_{transverse}$ - transverse strain; ϵ_{axial} - axial strain
Young's Modulus	$E = \frac{\sigma}{\epsilon}$	E - Young's modulus; σ - tensile stress; ϵ - extensional strain
Shear Modulus	$G = \frac{T}{\gamma}$	G - shear modulus; T - shear stress; γ - shear strain
Bulk Modulus	$K = \frac{\Delta p}{\Delta V/V_0}$	K - bulk modulus; Δp - pressure change; ΔV - change in volume; V_0 - initial volume

axial compression (contraction), the strain is positive [68]. Higher ratio indicates higher elasticity. Poisson's ratio is unitless parameter and it is most commonly used to describe the formations plasticity.

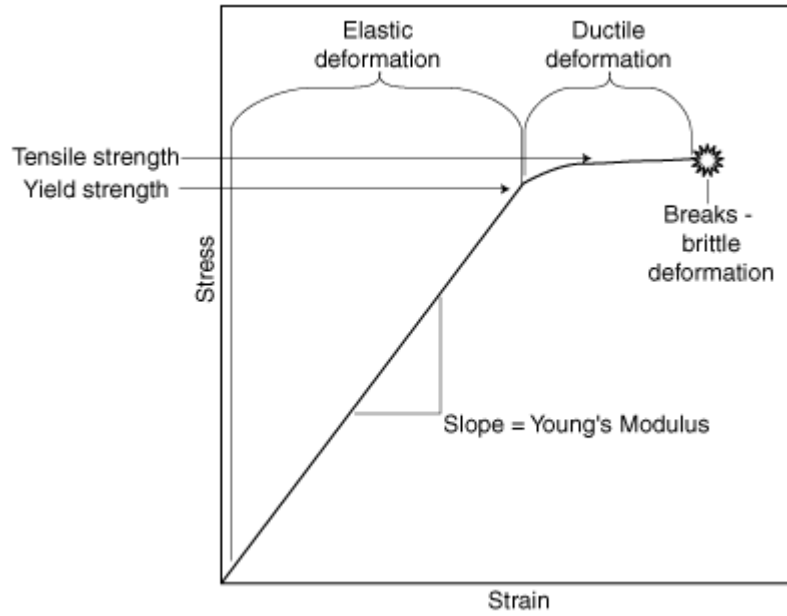


Figure 4.3: Relationship between stress, strain, elastic and ductile deformations. Young's modulus is denoted as the slope between stress and strain. Source: [54]

Bulk Modulus

Bulk modulus illustrates how the materials withstand the compression (isotropic volume change). It can be seen from formula in Table 4.2, that it is the ratio between the pressure change and relative volume change. This means that bulk modulus describes the resistance of the material to volumetric change. The inverse of bulk modulus is the compressibility. [68]

Computation of Elastic Properties

Techlog[©] calculates the elastic properties according to the sonic method, which is a model that relates the sonic and density logs to dynamic elastic moduli. Assuming a homogeneous, isotropic and elastic deformation, dynamic shear and bulk modulus are calculated as shown in Equations 4.6 to 4.7.

$$G_{dyn} = 13474.45 \times \frac{\rho_b}{(\Delta t_{shear})^2} \quad (4.6)$$

$$K_{dyn} = 13474.45 \times \rho_b \times \left[\frac{1}{(\Delta t_{comp}^2)} \right] - \frac{4}{3} \times G_{dyn} \quad (4.7)$$

where ρ_b is formation bulk density [g/cm^3], Δt_{comp} is compressional slowness of the bulk formation [$\mu s/ft$], Δt_{shear} is the shear slowness of the bulk formation [$\mu s/ft$], 13474.45 is conversion factor, K_{dyn} and G_{dyn} are dynamic shear and bulk modulus respectively [Mpsi].

Once parameters K_{dyn} and G_{dyn} are computed, it is possible to calculate the Young's modulus as shown in Equation 4.8.

$$E_{dyn} = \frac{9G_{dyn} \times K_{dyn}}{G_{dyn} + 3K_{dyn}} \quad (4.8)$$

where K_{dyn} and G_{dyn} are dynamic shear and bulk modulus respectively [Mpsi].

Dynamic Poisson's ratio is calculated in Techlog[©] using the following formula:

$$v = \frac{R_{sp}^2 - 2}{2R_{sp}^2 - 2} \quad (4.9)$$

where v is the Poisson's ratio, R_{sp} is the ratio between shear and compressional slowness. This ratio is depicted in Equation 4.10.

$$R_{sp} = \frac{\Delta t_{shear}^2}{\Delta t_{comp}^2} \quad (4.10)$$

4.5 Rock Strength

Rock strength is the property of rock, which illustrates how it behaves under certain loads of forces. If the rock is stressed beyond its limits (strength) it will fail in compression (shear fractures) or tension (tensile fractures) [35]. Different types of stresses present in the subsurface are depicted in Figure 4.4. It can be seen that in case of shear the forces are acting parallel to the surface. In case of compression forces are acting in perpendicular direction and towards the surface. For the case of tension the direction is away from the surface. Uniform stress, which is also called confining pressure, is defined as equal stresses towards the material from all directions.

According to Paterson and Wong [61], rock strength is a function of various parameters, which include: rock type and composition, grain size, rock density, rock porosity, rock anisotropy, temperature, water pore pressure, confining stresses and others. In the scope of our thesis, two important rock strength parameters are analysed: unconfined compressive strength (UCS) and tensile strength.

Unconfined Compressive Strength

According to Techlog[©] glossary, UCS (also called uniaxial compressive strength) is a significant property because it enables the engineers to predict a shear failure and the safe mud weight window is tightly linked to it. It is defined as the strength of a rock when it is crushed in one direction without lateral restraint [13].

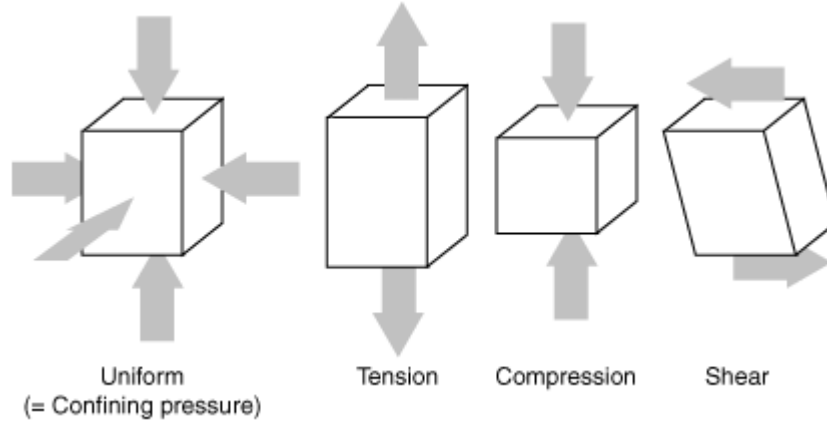


Figure 4.4: Different types of stresses. Source: [54]

In our thesis, Coates Denoo correlation was implemented in Techlog[©]. It is an algorithm that was first introduced in 1960s and is based on the Deere and Miller's sandstone and shale data [27]. The algorithm is shown in Equations 4.11-4.12.

$$C_0 = 0.0866 \times \frac{E_{dyn}}{C_{dyn}} [0.008V_{sh} + 0.0045(1 - V_{sh})] \quad (4.11)$$

where C_0 is the unconfined compressive strength [Mpsi], V_{sh} is the volume of the shale, E_{dyn} is dynamic Young's modulus [Mpsi], C_{dyn} is the dynamic bulk compressibility. It is defined as follows:

$$C_{dyn} = \frac{1}{K_{dyn}} \quad (4.12)$$

where K_{dyn} is dynamic bulk modulus [Mpsi].

Tensile Strength

Tensile strength is the maximum load that the material can withstand without fracturing when stretched. Another definition, according to Merck [54], is the amount of stress that is required to cause the solid to break. As seen in Figure 4.3, tensile strength is the plateau in the ductile deformation before the material will break. Techlog[©] calculates tensile strength based on UCS correlation. It is shown in Equation 4.13.

$$T_{str} = K \times UCS \quad (4.13)$$

where T_{str} is tensile strength [psi], K is the facies and zone factor (default value: 0.1), UCS is the unconfined compressive strength [psi].

Results and Discussion

5.1 Tensleep Reservoir Characterization

Overview

Teapot Dome produces light and sweet oil (sulphur content is less than 0.16%) from nine distinct formations. Tensleep, however, produces sulphurous oil. The main producing mechanism in the reservoir is water drive, which is a primary recovery mechanism in which the pressure from free water is enough to displace the hydrocarbons. [37] A summary of the key Tensleep reservoir and oil properties is shown in Table 5.1. The 3D average depth map of the reservoir is presented in Figure C.1 of Appendix C.

Table 5.1: Tensleep reservoir properties as of 2005. Modified after: [37]

Property	Value
Producing area	1.78 km ²
Average depth	1676 m
Average matrix permeability	80 mD
Oil API gravity	31
Reservoir temperature	87.7 °C
Reservoir pressure	158.6 bar
Average pressure at start of CO ₂ injection	138±6.9 bar
Initial formation volume factor	1.312 RB/BBL
Minimum miscibility pressure	89.6 bar

5.2 General Data

5.2.1 Location and Types of Logs

The results presented are based on the wells shown in Table 5.3. It can be seen that 10 different wells were used for petrophysical and geomechanical analysis

of the reservoir and the caprock. Log data was taken from the US Geological Survey Site (USGS), where it is in public access. As shown in the Table 5.3, 9 different types of logs were available: measured depth, caliper, compressional slowness, deep resistivity, formation temperature, gamma ray, neutron porosity, photoelectric factor and spontaneous potential logs. Thorough discussion of the types of logs (and the working principle) is available in Appendix A. Figure 5.1 shows the relative location of each well in the reservoir region. The northernmost well is 17-WX-21 and the southernmost well is 25-1-X-14 and the furthest distance between them is approximately 25 kilometers.

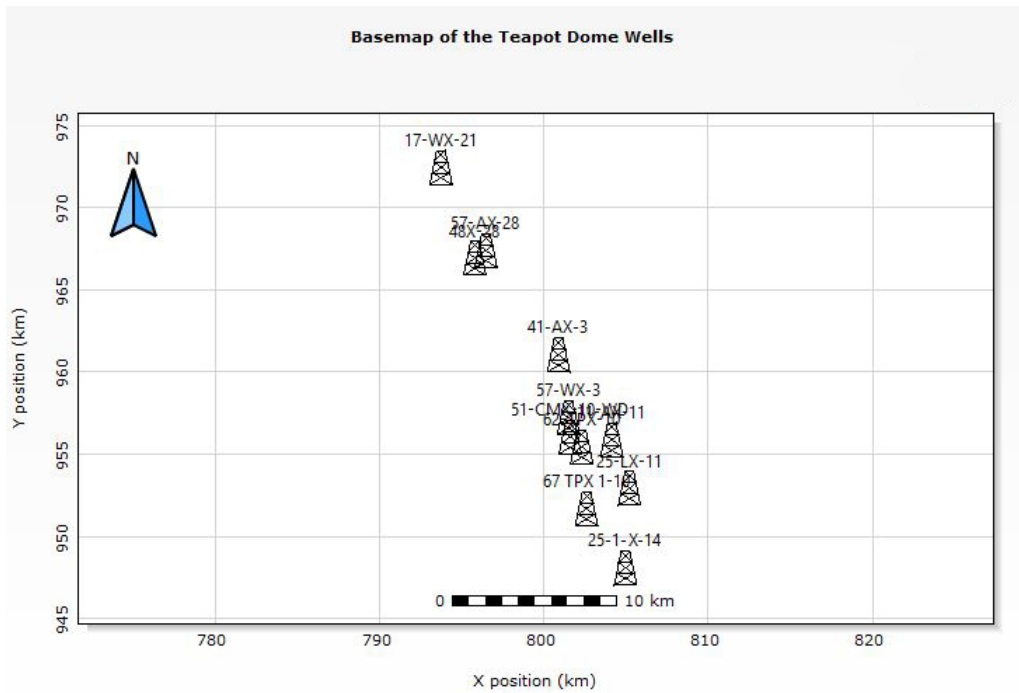


Figure 5.1: Map of the wells in the Teapot Dome region.

5.2.2 Thickness of Zones

The thickness of caprock and reservoir in each well was determined using the logview possibility in Techlog[©]. Average thicknesses of both zones across the wells (Pennsylvanian and Permian) and individual thicknesses are presented in Table 5.2.

5.2.3 Temperature Computation

Temperature of the reservoir and caprock was investigated using the FTEMP log in Techlog Precomputations[©]. FTEMP is a gradient method that is based on following equation:

$$FTEMP = TLT + \left[(depth - TLI) \times (gradFT) \right] \quad (5.1)$$

Table 5.2: Average thicknesses of Permian and Pennsylvanian layers across different wells.

Well Name	Thickness of caprock (ft/m)	Thickness of reservoir (ft/m)
11-AX-11	325.66 / 99.26	246.02 / 74.99
17-WX-21	320.66 / 97.74	277.29 / 84.52
25-1-X-14	296.02 / 90.23	272.64 / 83.10
25-LX-11	306.86 / 93.53	197.76 / 60.28
41-AX-3	282.66 / 86.15	202.89 / 61.84
51-CMX-10-WD	316.4 / 96.44	201.54 / 61.43
57-AX-28	315.79 / 96.25	215.72 / 65.75
57-WX-3	322.74 / 98.37	215.72 / 65.75
62-TPX-10	292.71 / 89.22	208.29 / 63.49
67-TPX 1-10	292.02 / 90.23	272.64 / 83.10
Average	307.55 / 93.74	231.05 / 70.42

where TLT is top log temperature [$^{\circ}\text{C}$], TLI is top log interval [m], depth is the depth of the well [m] and gradFT is gradient formation temperature [$^{\circ}\text{C}/\text{m}$]. In this thesis the temperature gradient used was $0.055\text{ }^{\circ}\text{C}/\text{m}$.

It was concluded that the average temperature in the caprock zone was $89.3\text{ }^{\circ}\text{C}$ and in the reservoir zone $93.7\text{ }^{\circ}\text{C}$, respectively.

Table 5.3: Wells and their wireline logs used in the thesis. Yellow color means that the log was present. Red color means that the log was not available.

Well		<i>Measured Depth</i>	<i>Caliper</i>	<i>Compressional Slowness</i>	<i>Deep Resistivity</i>	<i>Formation Temp.</i>	<i>Gamma Ray</i>	<i>Neutron Porosity</i>	<i>Neutron Porosity</i>	<i>Photoelectric Factor</i>	<i>Spontaneous Potential</i>
		MD	CALD	DT	RT	FTEMP	GR	CNL	NPHI	PEFZ	SP
1	11-AX-11	x	x	x	x	x	x	x	x	x	x
2	17-WX-21	x		x	x	x	x		x	x	x
3	25-1-X-14	x		x	x	x	x		x	x	
4	25-LX-11	x	x	x	x	x	x	x	x	x	x
5	41-AX-3	x		x	x	x	x		x	x	x
6	51-CMX-10-WD	x	x	x	x	x	x	x	x	x	x
7	57-AX-28	x	x	x	x	x	x		x	x	x
8	57-WX-3	x	x	x	x	x	x		x	x	x
9	62-TPX-10	x		x	x	x	x	x	x	x	x
10	67-TPX 1-10	x		x	x	x	x		x	x	

5.2.4 Pressure Computation

Pressure in reservoir and caprock was calculated in a similar manner to temperature, where Techlog Precomputations[©] were used. FPRESS can be computed in two ways, using either: mud density method or gradient method. In the scope of our thesis, the gradient method was implemented. It is based on the following equation:

$$FPRESS = depth \times gradFP \quad (5.2)$$

where gradFP is gradient formation pressure [Pa/m] and depth is the depth of interest [m].

Formation pressure gradient (gradFP) used in the thesis was 0.385 psi/ft (2650 Pa/m). The average result of this calculation was 148.27 bar for reservoir and 141.32 bar for caprock.

5.3 CO₂ Solubility Modelling

As mentioned in Chapter 2.2.3, CO₂ solubility in formation water is a significant aspect of the trapping mechanisms when performing injection. It is predominantly affected by three crucial factors: pressure, temperature and the ionic strength of the water. Figures 5.2 to 5.4 illustrate these dependencies. Figure 5.2 presents the solubility of CO₂ as a function of increasing pressure at a constant temperature. It can be seen that the solubility of CO₂ is proportional to the increase of pressure. This is described by Henry's law which states that the solubility of gases increases as the partial pressure of the gas over the solution increases (concentration of gas molecules increases with increasing pressure) [16]. The value of soluble CO₂ at reservoir conditions (P=148 bar and T=366 K) is 0.9912 mol CO₂ per kg of FW.

Figure 5.3 describes the change of CO₂ solubility at constant pressure, while the temperature increases. An opposite trend can be observed: as the temperature increases, more heat is added to the solution, which overcomes the attractive forces between the gas and the solvent molecules, and consequently reduces the solubility. [16].

Last part of solubility modelling was carried out by implementing the same online-accessible model (Duan *et al.* [30]) and changing the salinity of the formation water. Reference for the Tensleep formation salinity was taken from Morrow and Carlisle [56], where it is mentioned that the formation water salinity in Tensleep ranges from 3300 to 38650 ppm. An average value of the two was taken - 20975 ppm. It can be seen from Figure 5.4 that solubility of CO₂ decreases linearly as the salinity of the formation water increases. This is due to the so-called "salting-out" effect, which was described in Chapter 2.2.3. It has to do with the fact that the presence of electrolytes decreases the solubility of gases due to the mutual attraction between water molecules and salt ions [70].

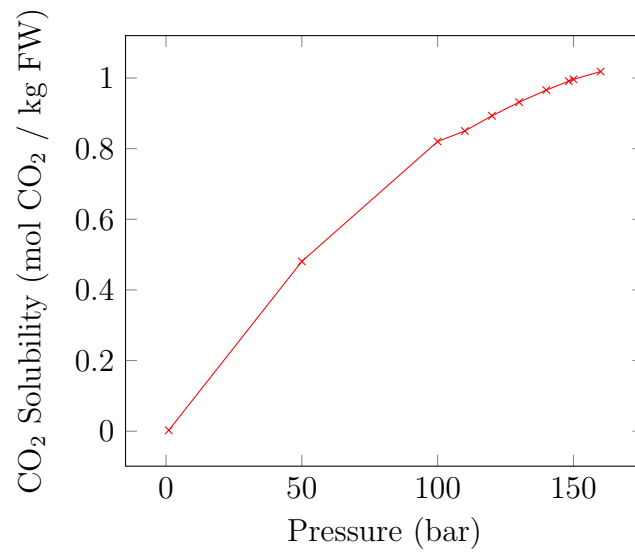


Figure 5.2: Solubility of CO₂ as a function of pressure at constant T=94 °C and FW salinity of 20975 ppm.

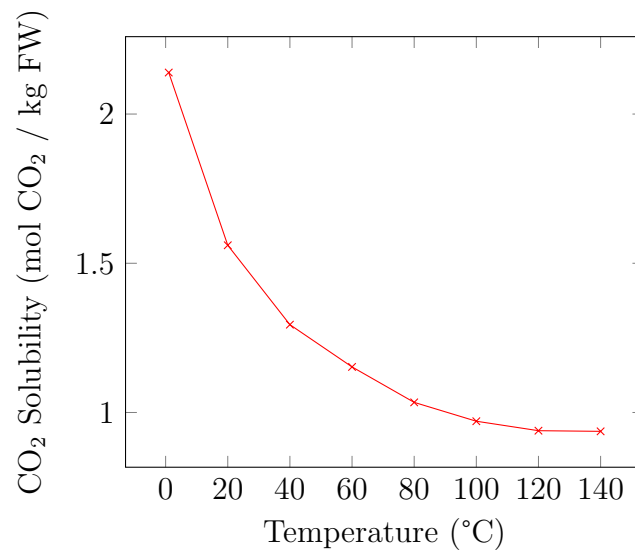


Figure 5.3: Solubility of CO₂ as a function of temperature at constant P=148 bar and FW salinity of 20975 ppm.

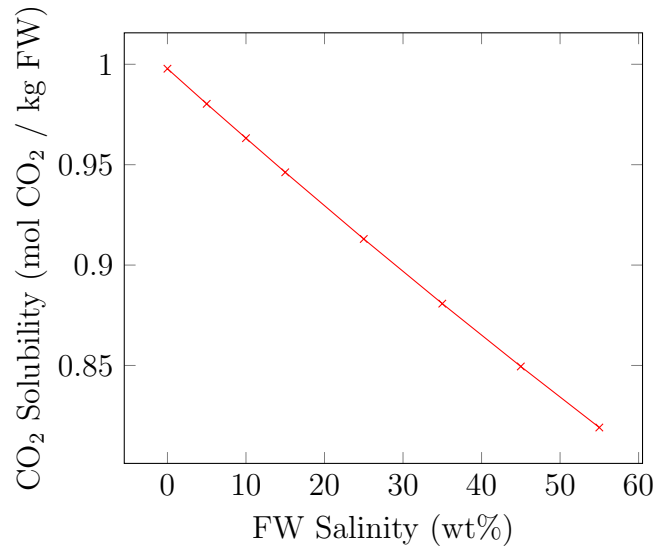


Figure 5.4: Solubility of CO₂ as a function of FW salinity at P=148 bar and T=94 °C.

5.4 Petrophysics

The discussion of the results for various petrophysical properties that were obtained in Techlog[©] will be presented in this chapter.

5.4.1 Total and Effective Porosity

Caprock

Figure 5.5 shows the boxplots of total and effective porosity for the caprock across the 10 wells of interest. It can be seen that for each individual well, the average total porosity in the caprock (Permian layer) is $6.489 \pm 4.172\%$ with the maximum of 39.19% in well number 62-TPX-10.

What pertains to effective porosity, which is the depicted next to the total porosity in Figure 5.5, it is clearly visible that there is non-existent effective porosity in the caprock with average value being $0.1375 \pm 0.0810\%$ with the maximum value of 21.46% in well 67-TPX 1-10.

Figure 5.7 shows the cumulative histogram of the total porosity for the caprock across the 10 wells. The peak of the data is around 0.084 to 0.089 v/v. This illustrates the region where most of the porosity are located. Maximum value of total porosity is 0.3918 v/v. Skewness is 0.3962 and kurtosis 1.4093. Average deviation is 0.034 v/v.

Reservoir

Furthermore, similar analysis for the reservoir was carried out. Figure 5.6 illustrates the total and effective porosities in the reservoir area across the wells under investigation. The average value for total porosity in the reservoir (Pennsylvanian layer) is $9.008 \pm 6.025\%$ and the maximum value is encountered for the well 57-WC-28, where it is 65.1%.

Effective porosities in the reservoir can similarly be seen in the Figure 5.6, where they are plotted next to the total porosities. Average effective porosity in the reservoir (Pennsylvanian layer) is $4.932 \pm 4.310\%$ with the maximum value obtained from well 57-AX-28, where it reaches 50.01%.

Figure 5.8 shows the cumulative histogram of the total porosity for the reservoir across the 10 wells. The peak of the data is around 0.042 to 0.047 v/v. This illustrates the region where most of the total porosity is located. Maximum value of total porosity is 0.6509 v/v. Skewness is 2.7702 and kurtosis 15.9268. Average deviation is 0.044 v/v.

It can be concluded that reservoir has both higher effective and higher total porosity due to different mineralogy. Figure 5.9 shows the porosity log for Permian and Pennsylvanian zone, showcasing the higher total porosity in the reservoir area.

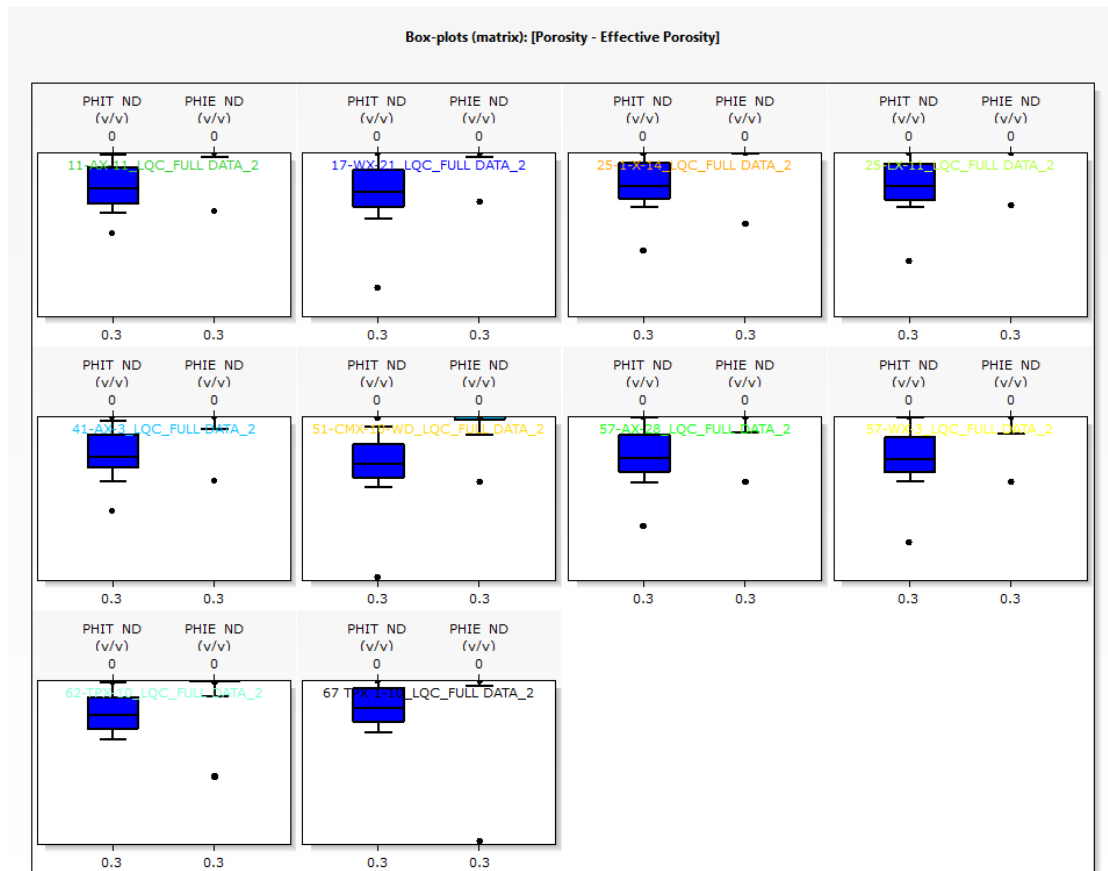


Figure 5.5: Depiction of total and effective porosity values for all the 10 wells in the caprock (Permian layer).

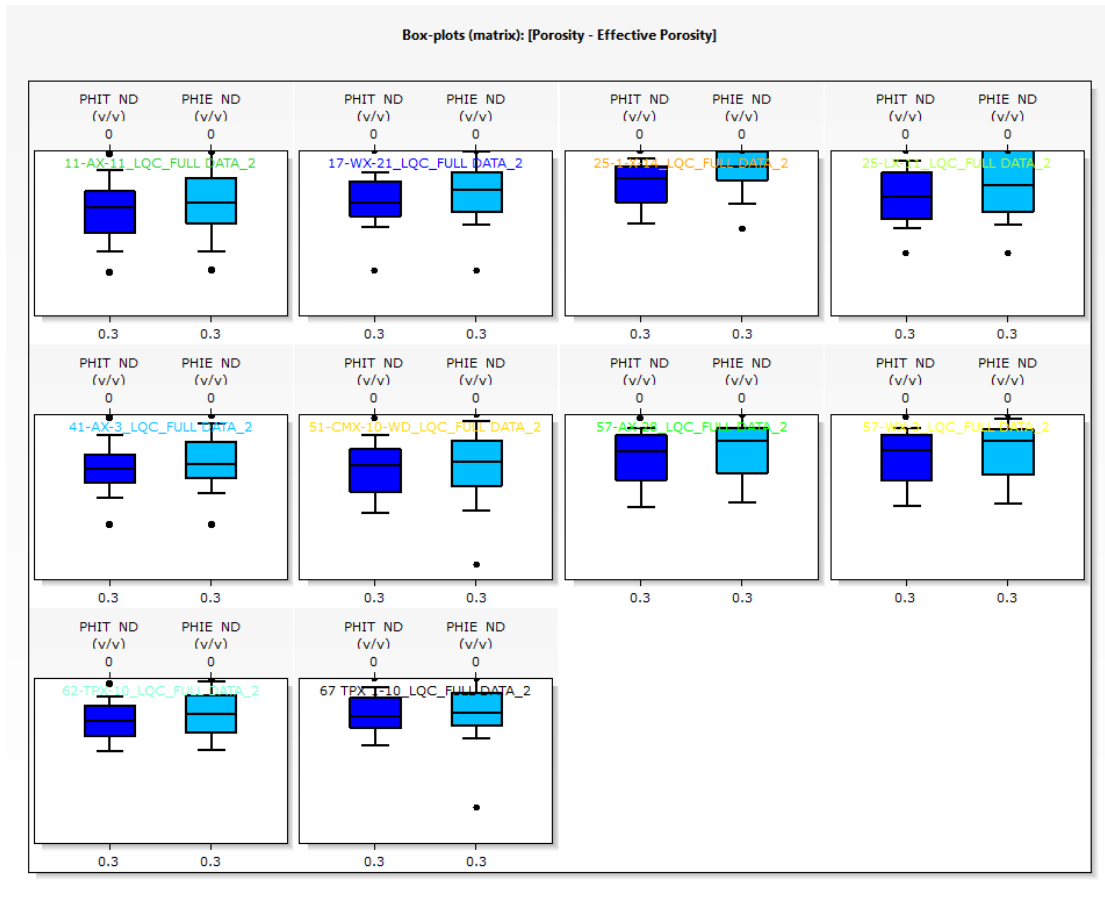


Figure 5.6: Depiction of total and effective porosity values for all the 10 wells in the reservoir (Pennsylvanian layer). Dark blue indicates the total porosity. Light blue indicates the effective porosity.

5.4.2 Water Saturation

Caprock

Figure 5.11 illustrates the cumulative histogram of the water saturations across the caprock (Permian layer). Peak of the data is around 0.34-0.36 v/v. The average water saturation for the caprock is 0.5141 ± 0.2677 v/v, which means that roughly half of the pores are filled with water. Skewness is 0.839 and kurtosis -0.763. Logview for well 67 TPX 1-10 can be seen in Figure 5.10. Results for all the wells are presented in Appendix B (Figure B.7).

Reservoir

Figure 5.12 illustrates the cumulative histogram of the water saturation across the reservoir (Pennsylvanian layer). Peak of the data is around 0.1595 v/v. The average water saturation for the reservoir is 0.2146 ± 0.1231 v/v. Skewness is 3.453 and kurtosis 14.9407. Figure B.8 in Appendix B illustrates the reservoir water saturation histograms for each well. Additionally, cross-plot for water saturation and porosity across all the wells can be seen in Figure B.11 of Appendix B.

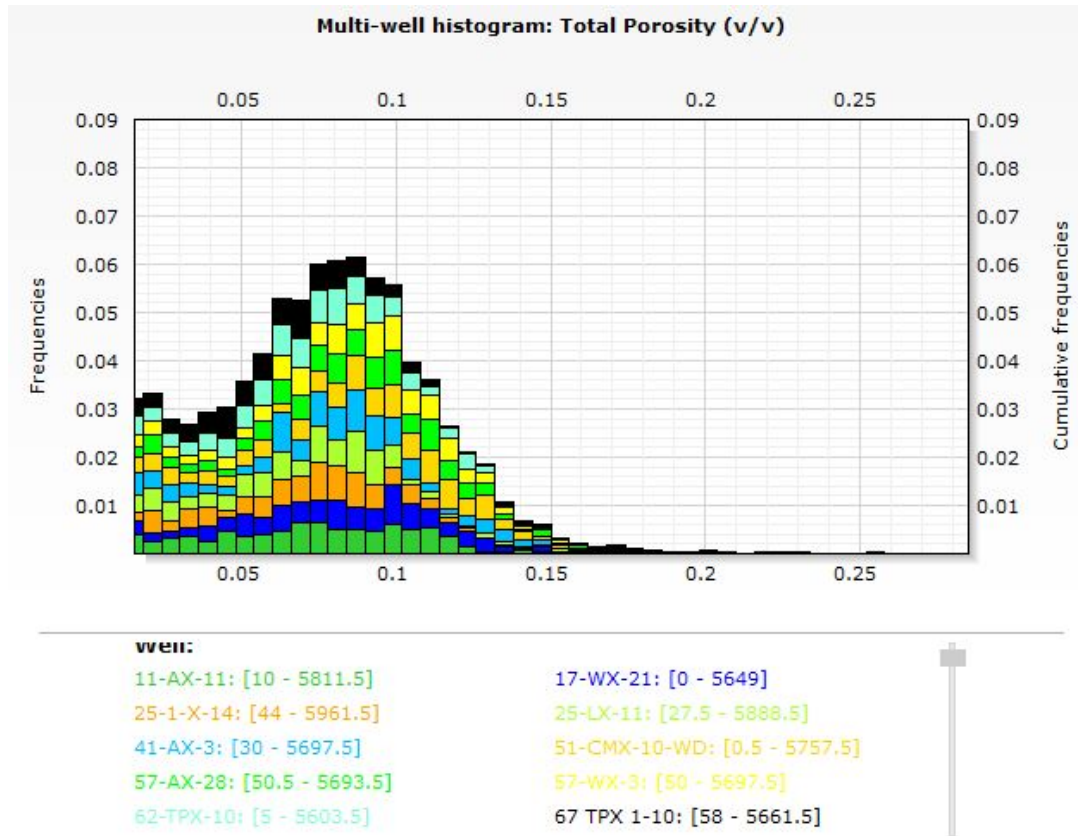


Figure 5.7: Depiction of a cumulative porosity values for all the 10 wells in the caprock (Permian layer).

Figures B.12 - B.13 show the distribution (logview) of the water saturations across both reservoir and caprock area. Figures B.9-B.10 in Appendix B show box plots of water saturations.

5.4.3 Permeability

Based on the computational steps that were described in Chapter 3.1.3, the results of permeability for caprock and reservoir were obtained.

Caprock

Cumulative histogram depicting the permeability in Permian layer using Coates method is shown in Figure 5.13. Mode across all the wells is 0.0594 mD and median value of 0.00232 mD. Skewness factor is 19.93 and kurtosis factor is 436.88. It can be noticed that the values are very left-skewed (positively skewed distribution), hence indicating a strong clusterization of samples in the region of 0.01 to 0.1 mD.

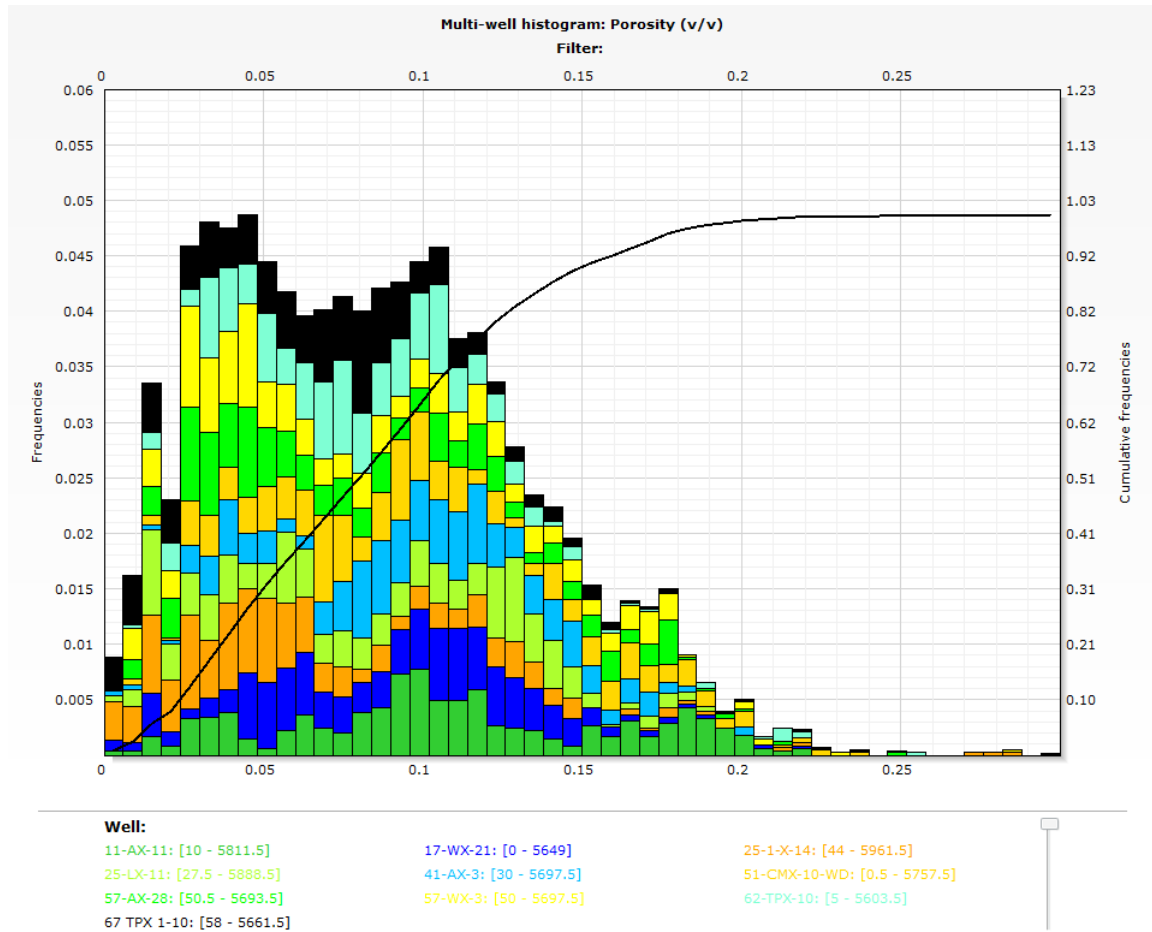


Figure 5.8: Depiction of a cumulative porosity values for all the 10 wells in the reservoir (Pennsylvanian layer).

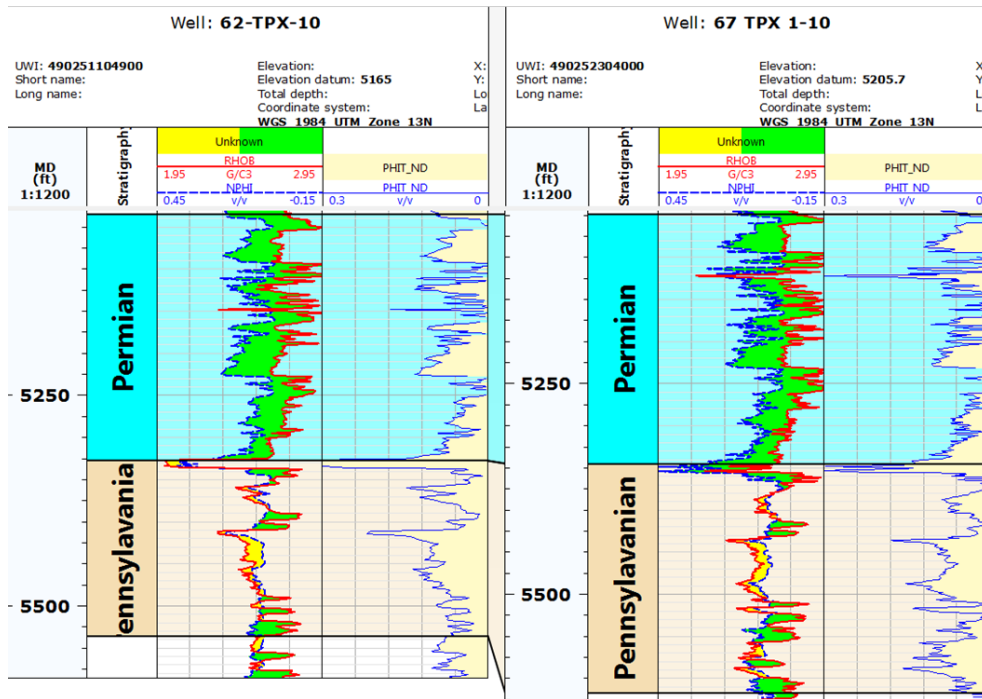


Figure 5.9: Total porosity logs across the Permian (Caprock) and Pennsylvanian (Reservoir) layers for Wells 62-TPX-10 and 67-TPX 1-10.

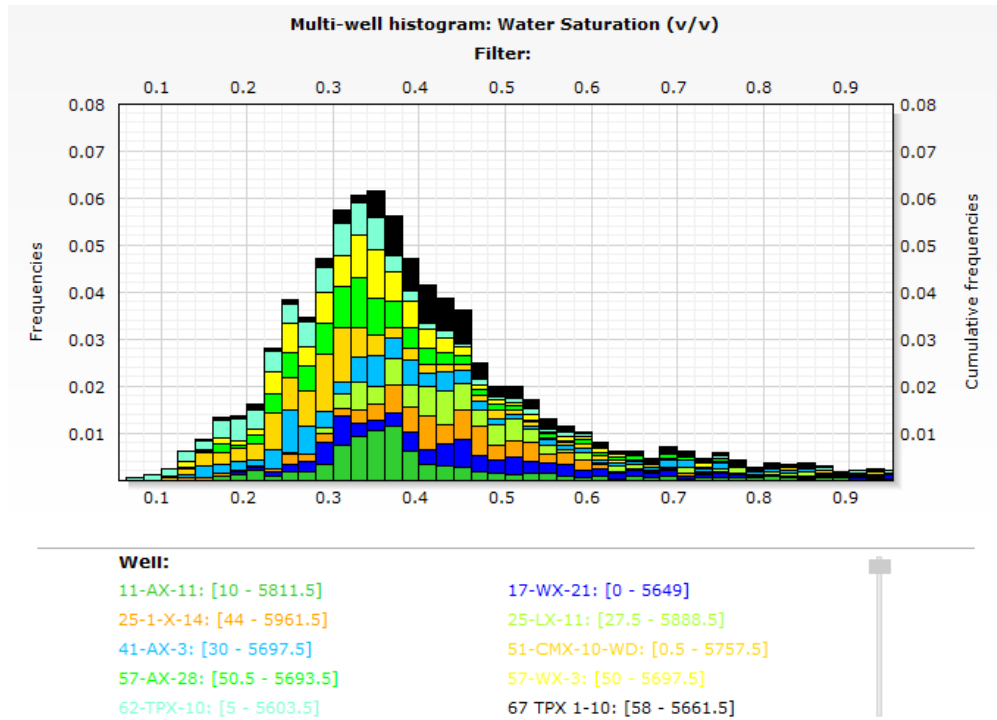


Figure 5.11: Depiction of cumulative water saturation of all the 10 wells in the caprock (Permian layer).

permeability and the porosity.

It can be noticed that higher permeabilities generally mean higher porosity values with the best match to the regression line in the highest data density area around 0.5-0.6 mD with some clusterization.

5.4.4 Volume of Shale

As mentioned in Chapter 3.1.4, for the purposes of calculating VSH the GR logs were used. They can be seen in Figure B.16. Before allowing Techlog[©] to perform the calculations of VSH, gamma ray matrix and gamma ray shale lines were adjusted manually to achieve a more precise result. Gamma ray index is then calculated using Formula 3.7. When Techlog[©] compiles the data, it is used to make a linear correlation to achieve a value of the volume of the shale, which is presented as a fraction of volume as seen in Figure B.16.

Caprock

Results of volume of the shale in the caprock area (Permian layer) leads to a conclusion that the caprock can be labeled as *"very shaly"*, since the calculated average volume of shale in the caprock region across all the wells is 0.5188 ± 0.3923 v/v. This shows that more than a half (52%) of the caprock is shale, while the remaining volume is left for the different rock layers as seen in the Figure 5.19. Figure 5.17 shows a cumulative histogram for the VSH. It can be seen that the

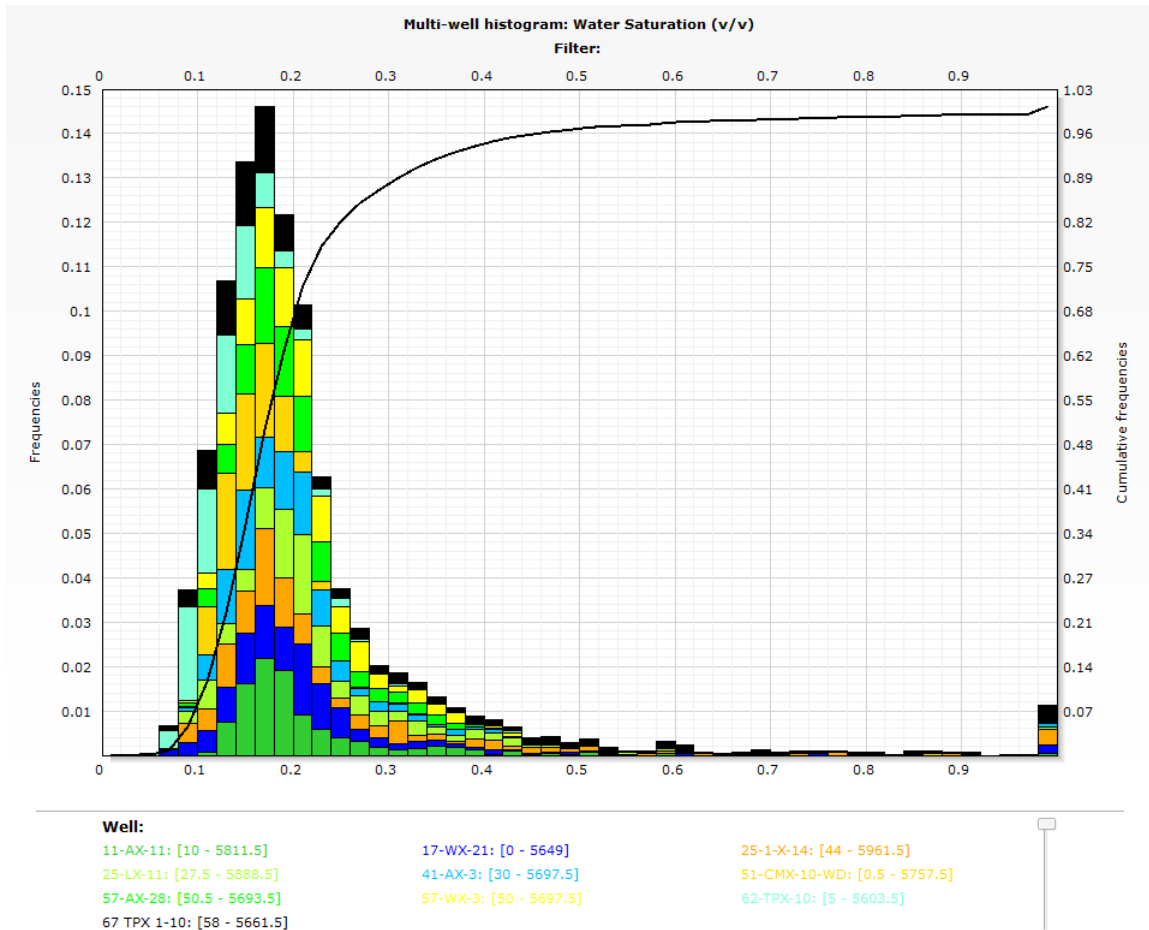


Figure 5.12: Depiction of cumulative water saturation of all the 10 wells in the reservoir (Pennsylvanian layer).

peak of the data is around 0.759-0.779 v/v, which means that is the area where most of the values are located. Skewness is -0.1702 and kurtosis -1.579. The volume of shale for each of the 10 wells in the caprock area can be seen in Figure B.15 in Appendix B.

Reservoir

VSH results in the reservoir are (Pennsylvanian layer) in line with the theoretical knowledge and an average VSH value across all the wells was 0.0841 v/v. Hence, the average volume of the shale present in the reservoir is around 8-9%, labeling it as *"not shaly"*. As discussed before, the remaining volume of the reservoir (91-92%) is occupied by different rock types as depicted in Figure 5.20.

As for the reservoir area, a cumulative histogram was plotted (Figure 5.16), illustrating the distribution of the VSH across the Pennsylvanian zone. The peak of the data is located around 0.059-0.079 v/v. Arithmetic mean is 0.0816 v/v. Skewness is 2.749 and kurtosis 8.247. The volume of shale for each individual well in the reservoir zone can be seen in Figure B.14 in Appendix B.

Overall conclusion can be made that the caprock is significantly more shaly than

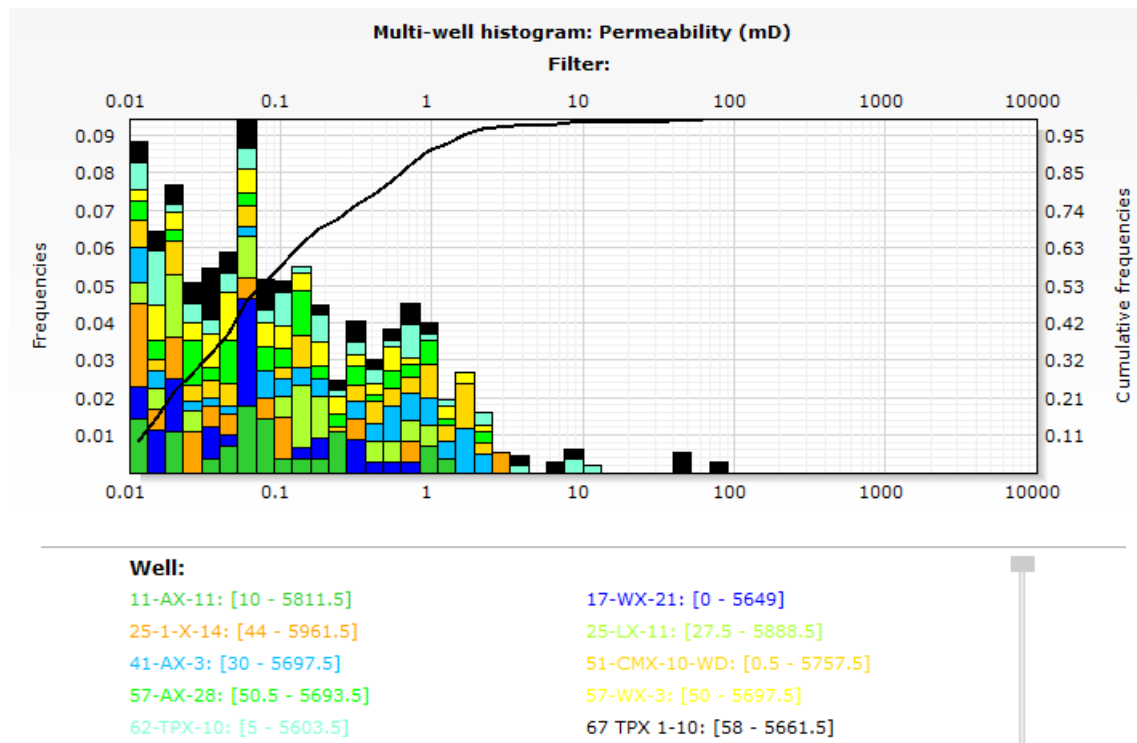


Figure 5.13: Depiction of cumulative permeability in the 10 wells in the caprock (Permian layer).

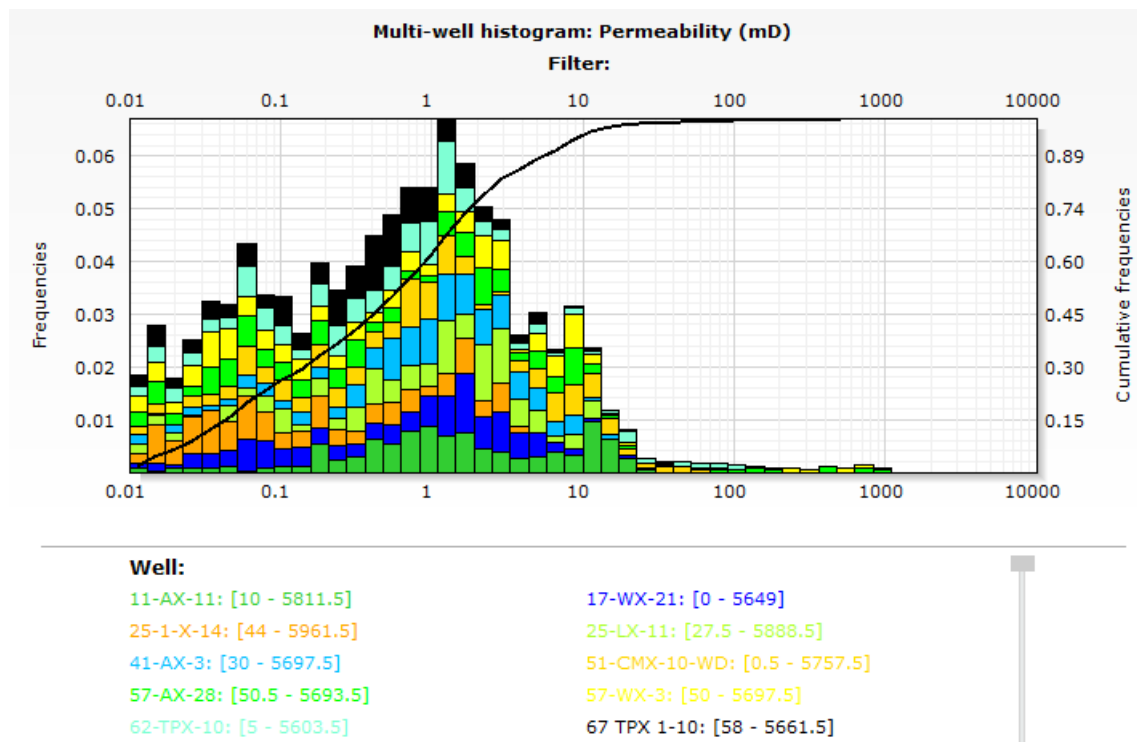


Figure 5.14: Depiction of cumulative permeability in the 10 wells in the reservoir (Pennsylvanian layer).

the reservoir, providing favourable geomechanical properties for CCS process. The overall difference of the shale volumes in the caprock and reservoir can be seen in Figure 5.18.

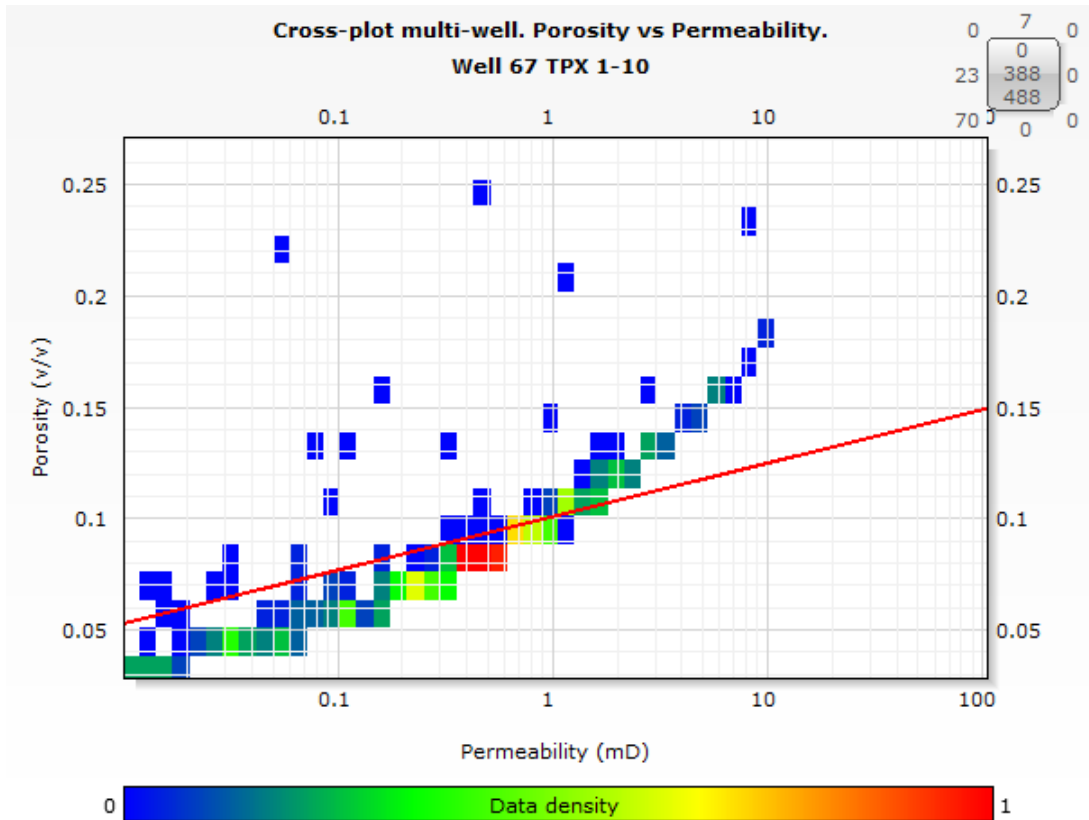


Figure 5.15: Permeability vs porosity crossplot for well 67 TPX 1-10. Red line indicates the trendline.

Table 5.4: Default densities used for computation of lithologies in Techlog[©]. Source: Techlog[©]

Lithology	Density (g/cm^3)
Quartz	2.65
Calcite	2.71
Dolomite	2.85
Anhydrite	2.98

5.4.5 Lithology

Lithology computation was performed in Techlog[©], which provided an crucial insight about the mineralogy of the caprock and the reservoir zones. Mineralogy computation is based on the inspection of the density at specific depth in a well (in this case: the Permian and Pennsylvanian layers). Using the catalog data, Techlog[©] identifies specific densities and assigns them to a specific mineralogy type. In most cases 4 different mineralogy types are found: sandstone, limestone, dolomite and anhydrite. Typical values of densities for the most common lithology types can be seen in Table 5.4.

Figures 5.21 and 5.22 illustrate the results of mineralogy in the caprock and reservoir regions. The full view of the mineralogy for all wells in caprock and reservoir can be seen in Appendix B (Figure B.17).

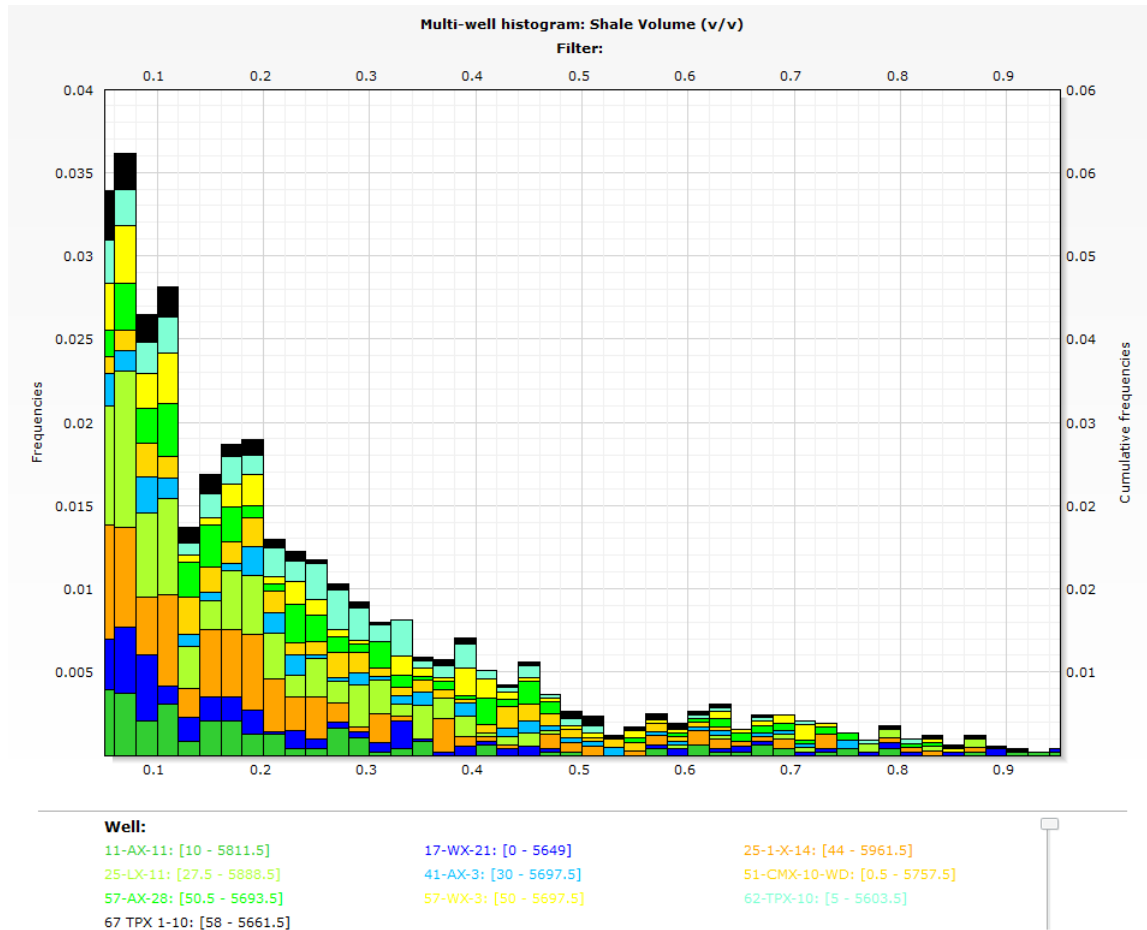


Figure 5.16: Depiction of cumulative volume of the shale of all the 10 wells in the reservoir (Pennsylvanian layer).

As seen in Figures 5.21 and 5.22, the mineralogy is given as volume fractions for each type of rock layer. It is important to mention that this volume fraction does not include the shale volume. This means that if, for example, one of the wells contains 15% shale (exact values of shale volume can be found in Chapter 5.2.3), the lithology computation is given in the remaining 85% of the volume. From the logview it is possible to determine the percentage of each rock type at a specific depth. The trend across all the wells is similar and as it can be seen in Figure 5.21, for the caprock area (Permian layer), the dominant rock type is dolomite, followed by limestone. There are small layers of anhydrite present at certain depths as well. It can be seen from Figure 5.22 that for the reservoir area (Pennsylvanian layer), the mineralogy is predominantly composed of limestone and sandstone. At certain depths smaller layers of dolomite are present, as well. As mentioned above, the overall trend across all the well in both layers is similar, so to have an overall look at the lithology, the averages of each rock type in each well were taken and plotted as pie charts.

As seen in Figure 5.19 about 78% of the volume is occupied by dolomite, followed by 14% of limestone and 8% of anhydrite. The values for sandstone were minuscule for most of the wells.

It can be seen from Figure 5.20, which depicts the lithology in the reservoir, that

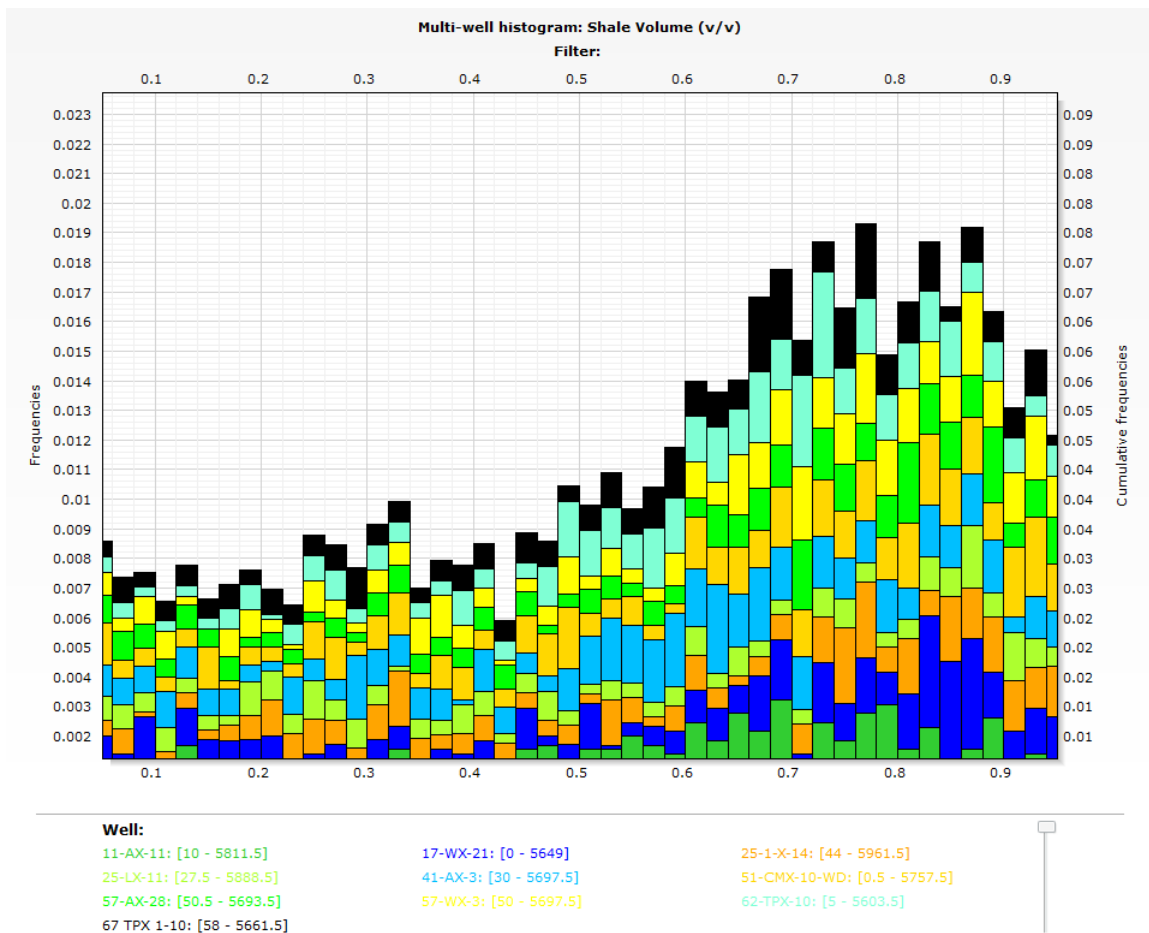


Figure 5.17: Depiction of cumulative volume of the shale of all the 10 wells in the caprock (Permian layer).

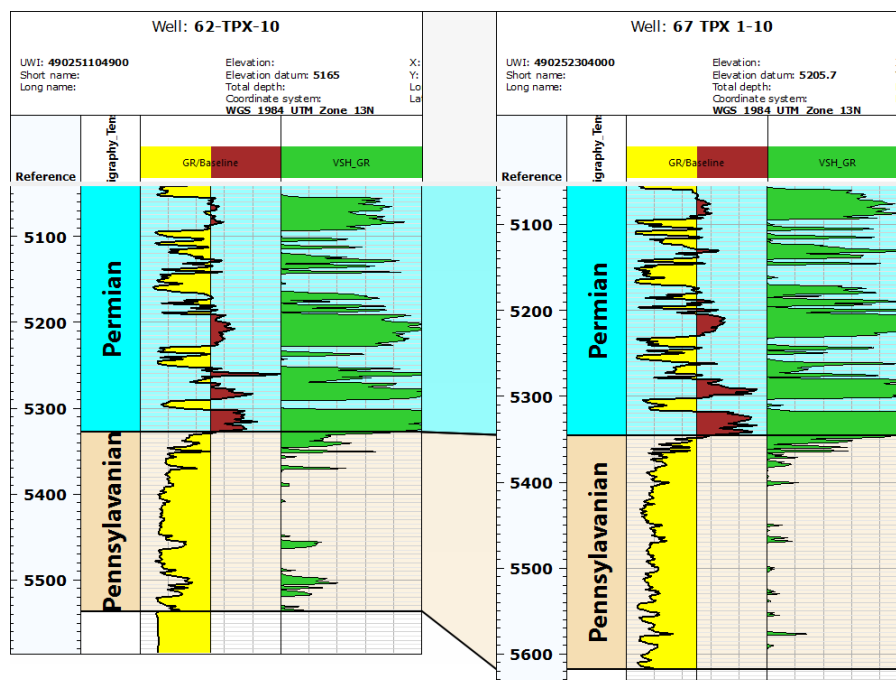


Figure 5.18: GR and VSH logs for wells 62-TPX-10 and 67-TPX-1-10 showcasing the calculation of VSH.

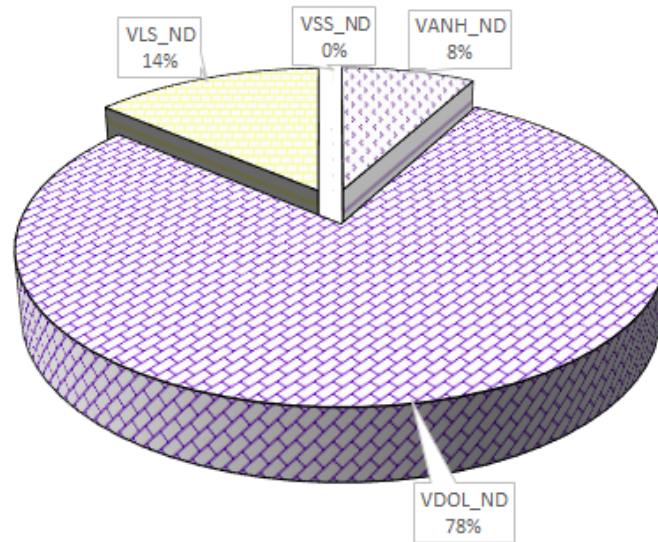


Figure 5.19: Average lithology composition of caprock (Permian layer) of all the wells.

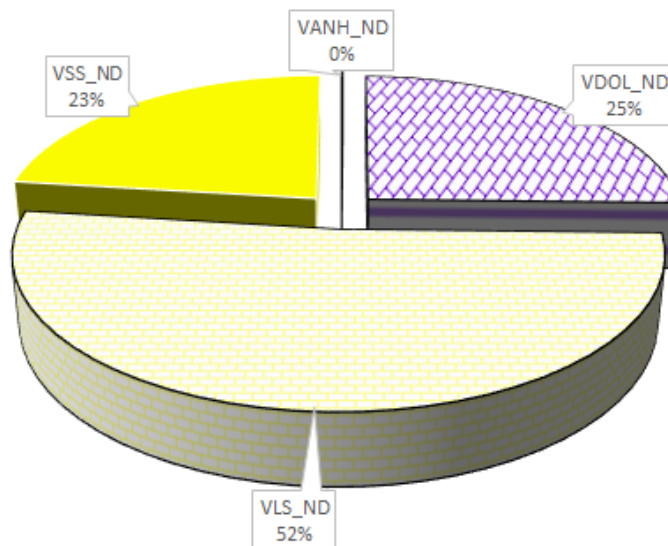


Figure 5.20: Average lithology composition of reservoir (Pennsylvanian layer) of all the wells.

more than half of the volume (52%) is occupied by limestone, followed by 25% dolomite and 23% of sandstone. The values of anhydrite are minuscule, thus in the overall view depicted as 0%.

The overall conclusion can be made that the caprock is predominantly composed of dolomite, showing several smaller layers of limestone and anhydrite, which provide favourable elastic characteristics for the caprock. Moving into the Pennsylvanian layer, the transitional change can be seen - the values of dolomite decrease by more than a half, while the values of limestone increase to more than 50% of the volume. Favourable layers of sandstone occupy more than 20% of the volume, while in the caprock the value is approximately 0%.

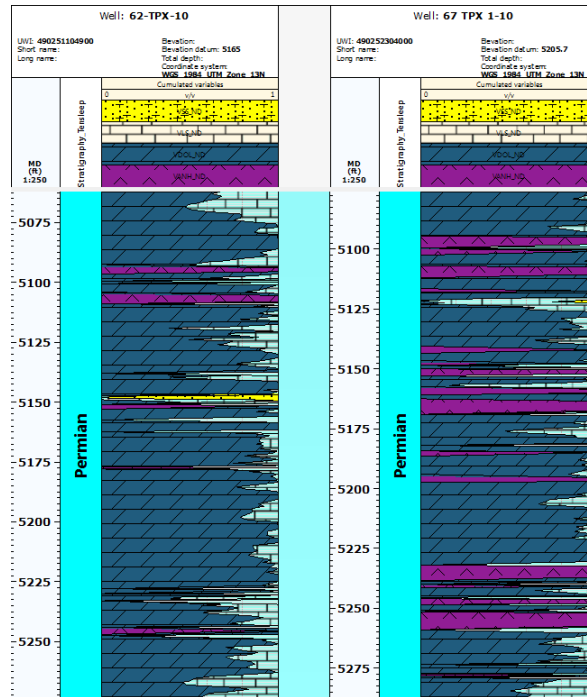


Figure 5.21: Mineralogy for wells 62-TPX-10 and 67 TPX 1-10 in the Permian layer.

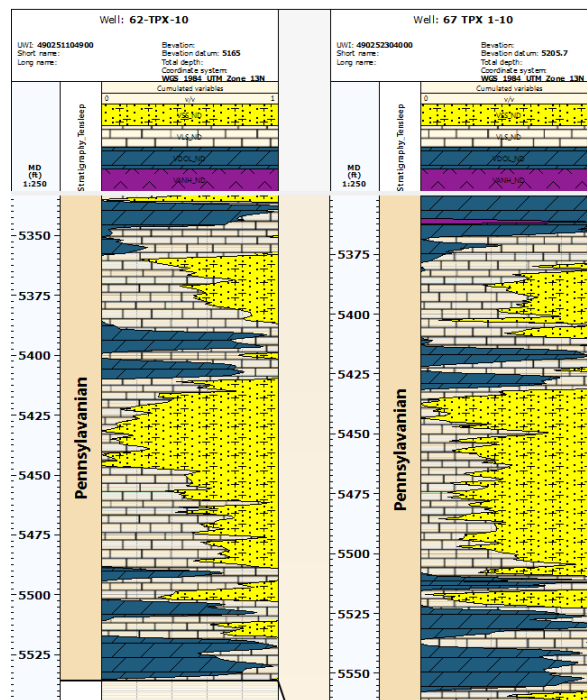


Figure 5.22: Mineralogy for wells 62-TPX-10 and 67 TPX 1-10 in Pennsylvanian layer.

5.5 Geomechanics

This chapter presents the geomechanical results that were obtained in Techlog[©]. It is divided into four main parts: pore pressure, fracture gradient, elastic properties and rock strength properties.

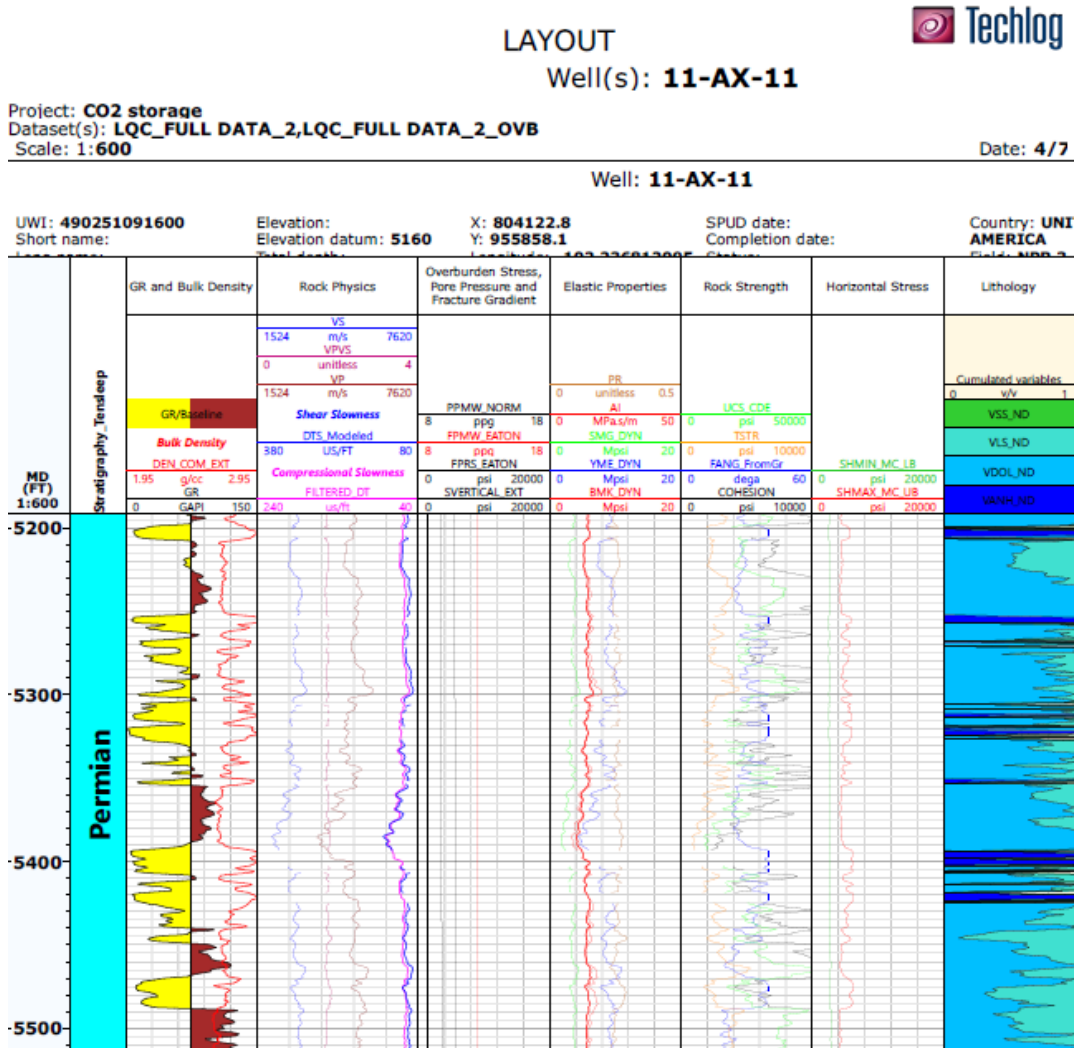


Figure 5.23: Logview for Well 11-AX-11: determination of rock physics, overburden stress, elastic properties, rock strength, horizontal stress and lithology.

5.5.1 Pore Pressure

Pore pressure calculations were performed in Techlog[©] to gather information about the average values in the reservoir zone (Pennsylvanian layer). It must be noted that the computation of the pore pressure was performed only for the reservoir zone, as it is the area of interest regarding the storage of CO₂. Calculation showed that the average pore pressure across all ten wells is 2515.947±28.773 psi. This provides vital information regarding the injection pressure of CO₂, as it should be higher than the pore pressure, for CO₂ enter the pore. Figure 5.24 presents the pore pressure across the 10 wells.

5.5.2 Fracture Gradient

Fracture gradient calculations were carried out, providing vital pressure values regarding the fracturing of the caprock (Permian layer). The average value seen across all the wells is 3444.161±62.011 psi. This value indicates the limit of

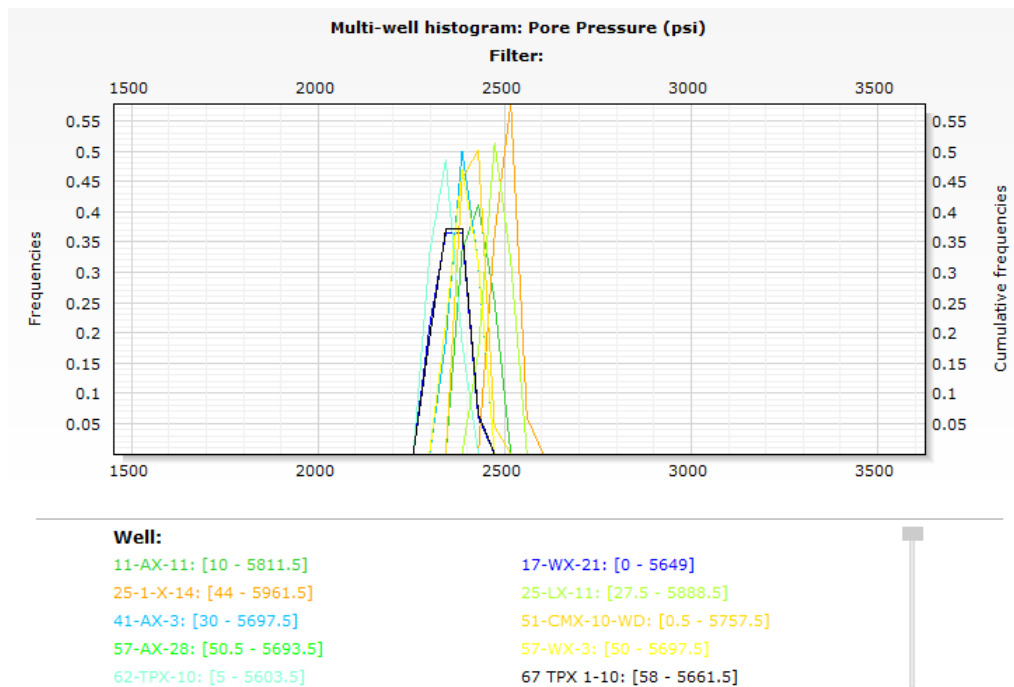


Figure 5.24: Multi-well histogram of pore pressure values across 10 wells in the reservoir zone (Pennsylvanian layer).

pressure for the caprock. If the pressure exceeds this average value, the caprock area might undergo fracturing, thus increasing the chances of CO₂ leaks from the reservoir into the adjacent formations. Figure 5.25 shows the change in pressure across all 10 wells. It must be noted that increasing depth increases the pressure values. Sharp cuts at the start and the end of the graph indicate the beginning and end of the caprock zone (Permian layer) with the lowest pressure values at the top of the layer and the highest values at the bottom of the layer.

5.5.3 Elastic Properties

Computation of elastic properties of the caprock (Permian layer) were performed in Techlog[®] providing the following properties described in the upcoming chapters. Computational methods used to obtain the elastic properties are presented in Chapter 4.4.

Shear Modulus

Calculation of the shear modulus was completed providing an average value for all the ten wells of 3.473 ± 0.683 Mpsi. This value indicates the rigidity of the caprock. In this case the value is somewhat low, indicating that the caprock has some elasticity that is most likely provided by the presence of anhydrites within the caprock as seen in Figure 5.19. Figure 5.51 depicts the shear modulus across 10 wells. Data has a leptokurtic distribution, which indicates strong clusterization of samples, which means higher peak (kurtosis) around the center of the distribution.

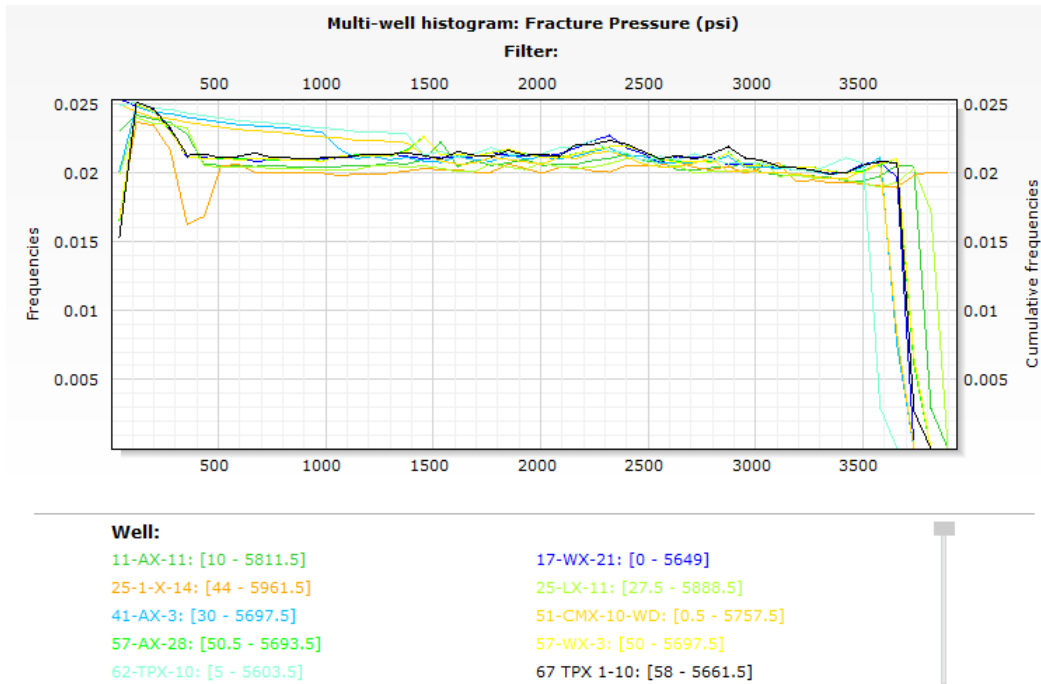


Figure 5.25: Multi-well histogram of fracture pressure across 10 wells in the caprock zone (Permian layer).

It can be seen that the majority of values are based around the mentioned average of 3.473 Mpsi.

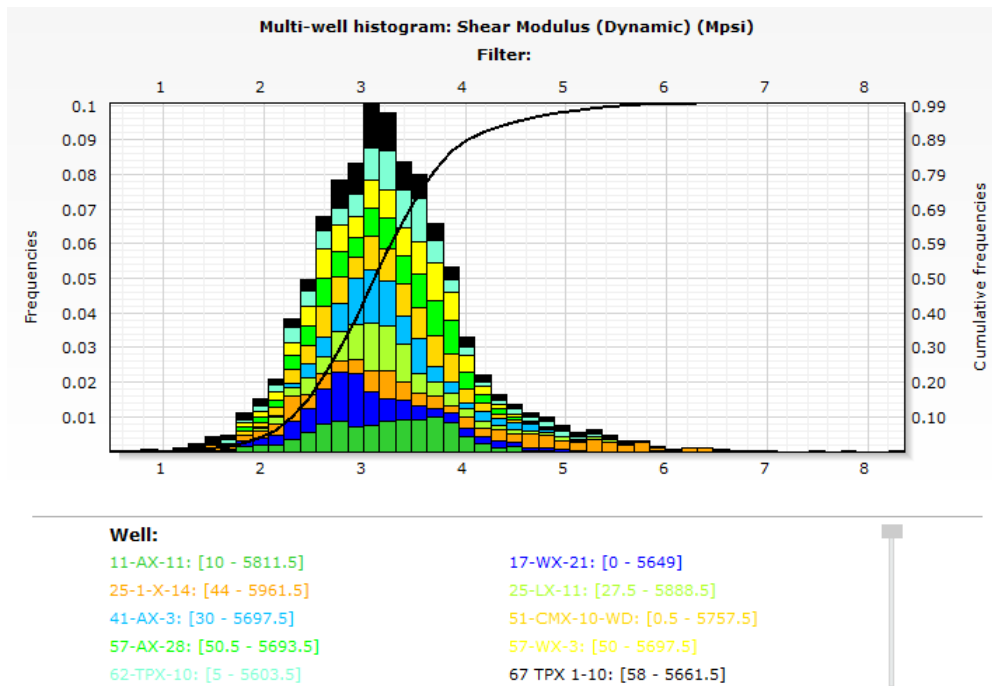


Figure 5.26: Shear modulus multi-well histogram depicting pressure values across 10 wells in the caprock zone (Permian layer).

Young's Modulus

Young's modulus calculations were completed and they provided the average pressure values for all the wells in the caprock zone (Permian layer). Average values across the ten wells is 8.699 ± 1.668 Mpsi. As it was noticed with shear modulus, higher value of the property illustrates the rigidness of the caprock. In this case, Young's modulus is indicating a somewhat lower value, indicating that the caprock has elastic properties. Depiction of the pressure values collected for Young's modulus can be seen in Figure 5.27. As noticed with shear modulus, the data has leptokurtic distribution with higher peak in the middle of the distribution (distribution mean).

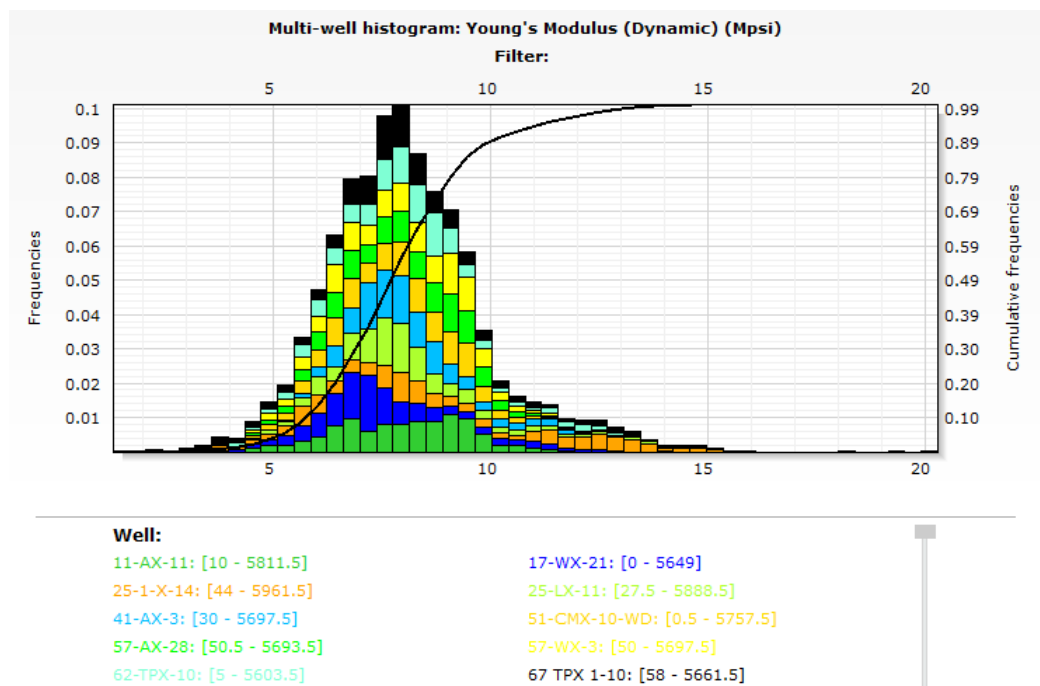


Figure 5.27: Multi-well histogram of Young's modulus in the caprock zone (Permian layer).

Poisson's Ratio

Completing the calculation for the Poisson's ratio, the unitless average value within the caprock zone (Permian layer) across the 10 wells is 0.253 ± 0.013 . As mentioned in Section 4.4 the higher the value of the ratio, the more elastic the caprock is. Thus, it can be concluded that the calculated Poisson's ratio for the caprock is describing somewhat elastic tendencies. Poisson's ratio shows asymmetry with right-skewed distribution. Graphical depiction of the Poisson ratio values in all the 10 wells can be seen in Figure 5.28.

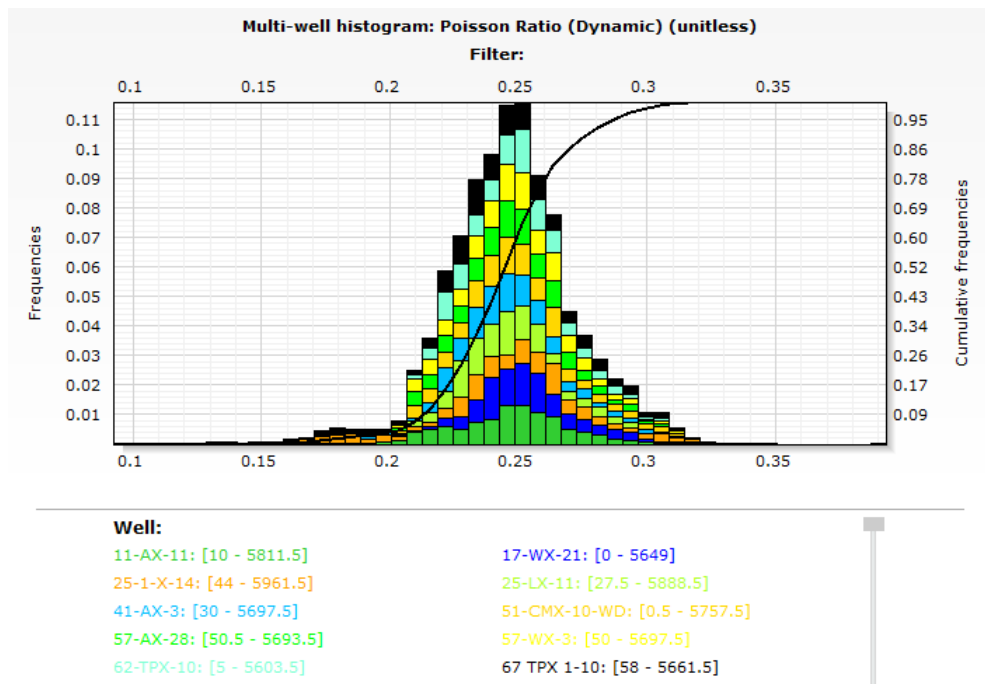


Figure 5.28: Multi-well histogram of Poisson’s ratio in the caprock zone (Permian layer).

Table 5.5: Statistical properties of the elastic parameters.

Elastic Property	StDev	Average	Range of Values
Shear Modulus [Mpsi]	0.7656	3.4730	0-8.3556
Young’s Modulus [Mpsi]	1.8411	8.6993	0-20.2872
Poisson’s Ratio [unitless]	0.0251	0.2537	0-0.39275
Bulk Modulus [Mpsi]	1.2354	5.8724	0-12.1073

Bulk Modulus

Calculations of the bulk modulus were carried out, providing additional information regarding the elastic behaviour of the caprock. Average value across the ten wells for the bulk modulus is 5.872 ± 1.038 Mpsi. Generally, the higher the bulk modulus value, the more resistant it is to deformation, or in other words - less elastic is the caprock. Conclusion can be drawn that the caprock (Permian layer) is predominantly elastic. Bulk modulus shows asymmetry with left-skewed distribution. Graphical depiction of the bulk modulus for each well can be seen in the multi-well histogram in Figure 5.29. It can be seen that most of the recorded values are close to the average value across all the wells. Table 5.5 shows the standard deviation, average and the range of the values for the four investigated elastic properties.

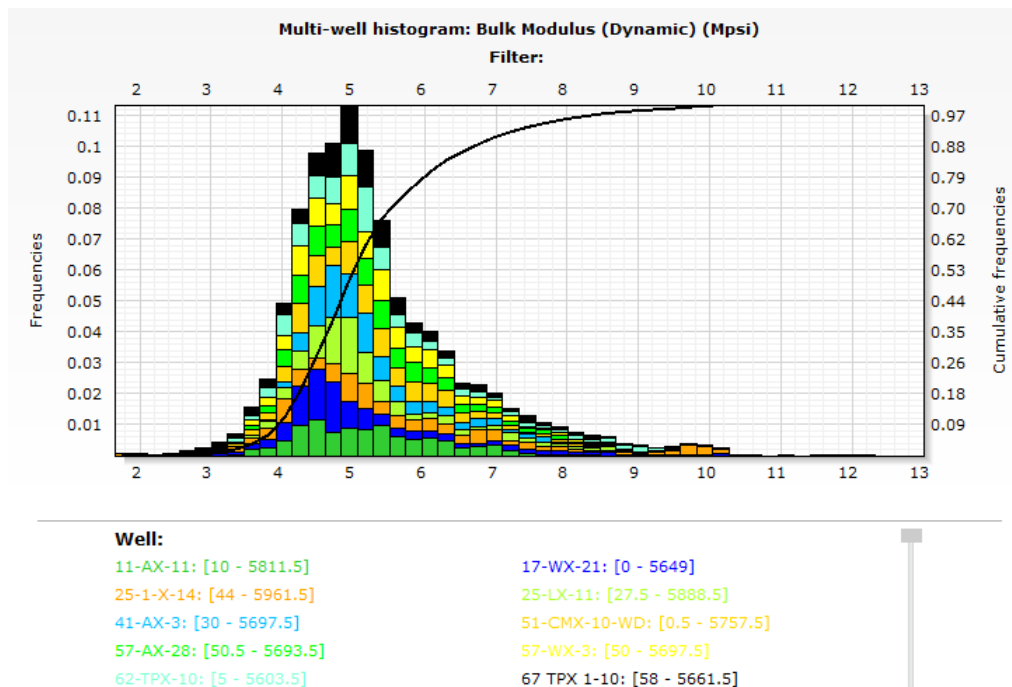


Figure 5.29: Multi-well histogram of bulk modulus in the caprock zone (Permian layer).

Table 5.6: Statistical properties of the rock strength parameters

Rock Strength Property	StDev	Average	Range of Values
UCS [MPa]	71.08	168.745	0-1145.58
Tensile Strength [MPa]	7.108	15.8745	0-114.558

5.5.4 Rock Strength

Unconfined Compressive Strength

UCS calculations were completed and the average pressure value for all the 10 wells is 168.745 MPa as seen in Table 5.6. The value indicates that the caprock can withstand the given average pressure before breaking. Figure 5.30 depicts the values for each of the 10 wells.

Tensile Strength

Tensile stress calculations were performed and the average value for all the wells was 15.87 MPa as seen in Table 5.6. Graphical depiction of tensile strength values for all the wells can be seen in the multi-well cumulative histogram Figure 5.31.

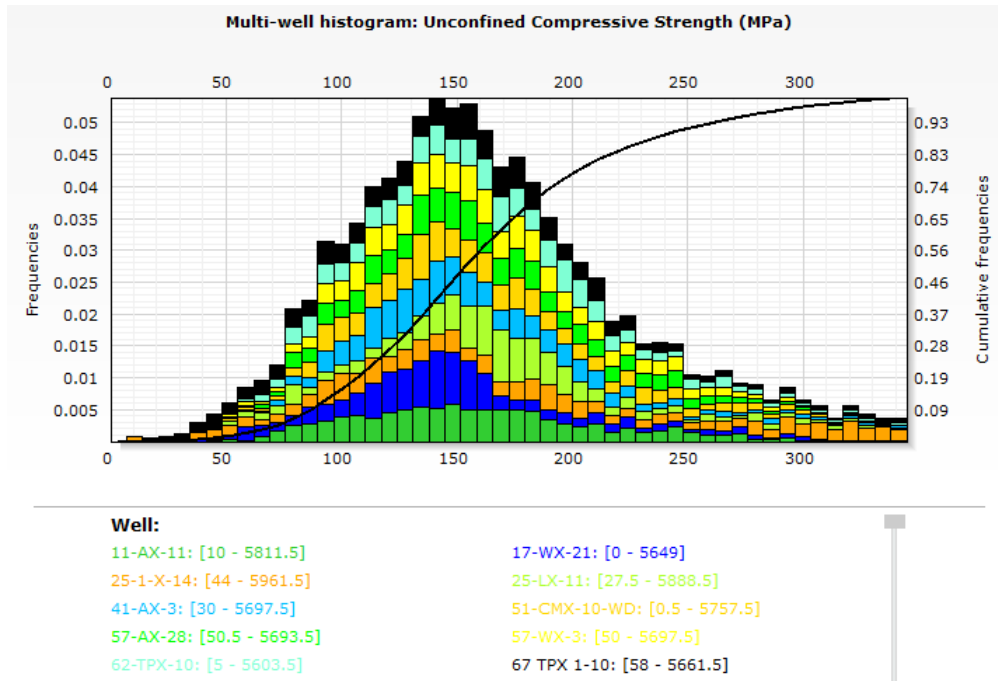


Figure 5.30: Unconfined Compressive Strength of all the 10 wells in the caprock zone (Permian layer).

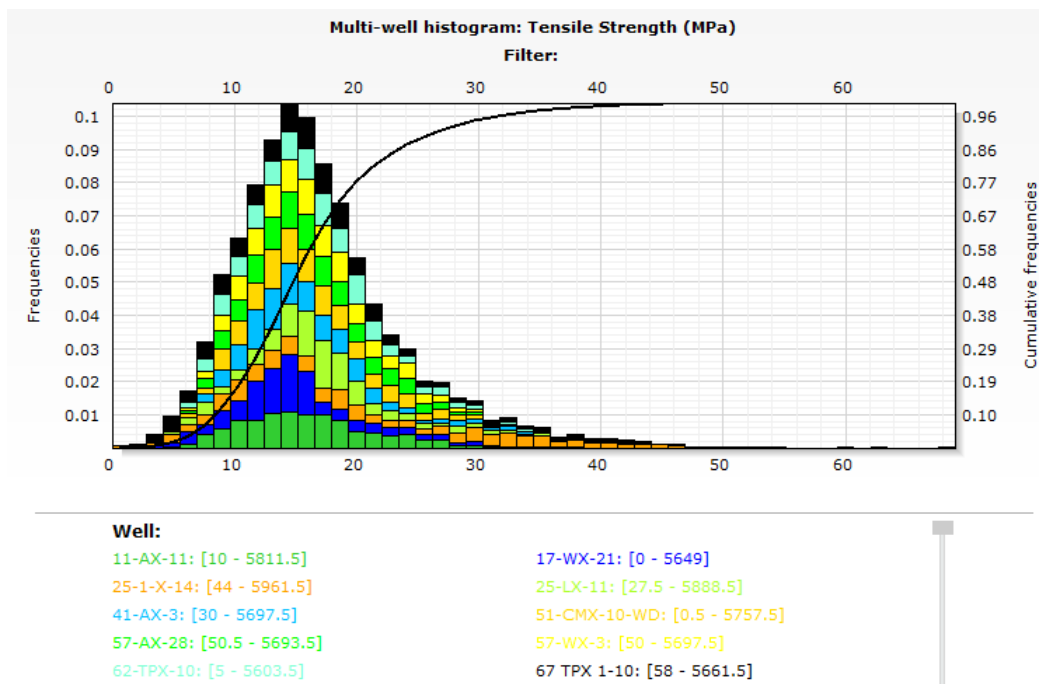


Figure 5.31: Tensile strength of all the 10 wells in the caprock zone (Permian layer).

5.5.5 Brittleness-Ductility Analysis

As described in various works [63, 42], rocks with low Young’s modulus and high Poisson’s ratio are considered ductile and rocks with high Young’s modulus and low Poisson’s ratio are considered brittle. According to Perez [62], ductility is significantly affected by mineralogy, and the content of calcite and quartz makes

the caprock more brittle. However, zones with higher clay content are considered more ductile. Brittleness-ductility analysis was carried out in Techlog[®] and the result for well 67 TPX 1-10 is seen in Figure 5.32. Well 67 TPX 1-10 was selected because of its complete data. Distinction between brittleness and ductility can be observed. Most of the data for that specific well is concentrated in the ductile region.

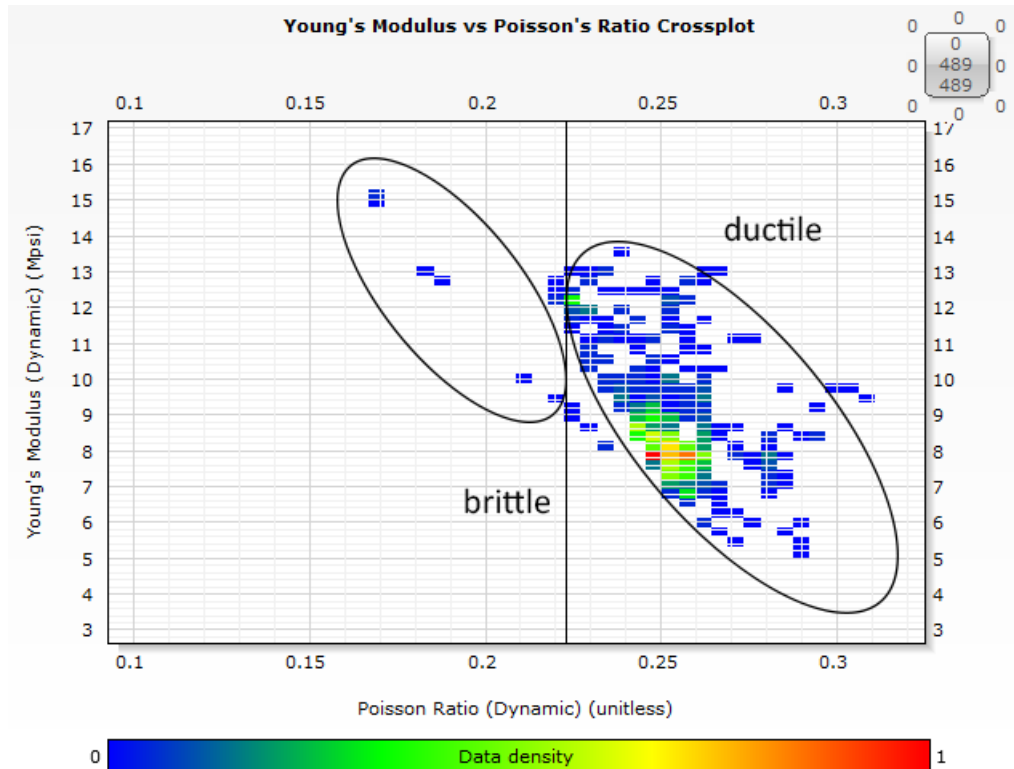


Figure 5.32: Relationship between Young's modulus and Poisson's ratio for Well 67 TPX 1-10 (Permian zone).

5.6 Petrel[©] Model

In the scope of our thesis, Petrel[©] 2017.1 was implemented for the 3D visualization and analysis of the Tensleep reservoir. The methodology, computational techniques and results are presented in this section.

5.6.1 Problem Set-Up and Limitations

The objective of the analysis in Petrel[©] was to create a static model and analyse the distribution of the petrophysical and geomechanical properties over the area of both reservoir and the caprock. As mentioned in the beginning of the thesis, the following assumptions were made:

1. the reservoir is depleted (depleted volume is equal to the volume of oil);
2. the wells are not plugged;
3. wells are vertical (i.e. not directionally drilled wells);
4. the 3D model of the caprock (Permian layer) is based on the geometry of the reservoir (Pennsylvanian layer).

Additionally, a number of uncertainties are present in the model. Most significant of them is the uncertainty at the edges of the the model, which is due to the lack of reference points for the calculation (the wells are mostly located in the inner part of the area) when the properties are being interpolated-extrapolated with a mathematical technique in Petrel[©]. We also assume that there is an uncertainty in the well tops values and wireline log indications, although latter ones can be considered negligible. In the scope of our thesis the seismic data was not available due to technical complications. This also creates uncertainties, because seismic data is especially helpful in providing information between the wells. Consequently, we estimate that within 2 km range of each well the model describes the property distribution in an accurate manner and the uncertainty of well positioning is very low.

The analysis in Petrel[©] started with the gathering the well top data, horizons etc. data from open sources. Furthermore, the well log data was imported from Techlog[©], that was the essential basis for the Petrel[©] analysis. Consequently, the well tops, well depths, well logs were incorporated to produce the skeleton model of the Tensleep formation. Next step was to create four distinct surfaces that is presented in Figure 5.34. It can be seen that the cross-section is divided into: (i) Triassic layers and above, (ii) Caprock (Goose Egg formation, Permian period), (iii) Reservoir (Tensleep formation, Pennsylvanian period) and (iv) Mississippian layers and below as can also be seen in Figure 2.1.2. An important part of the numerical analysis in Petrel[©] is the upscaling part. This method creates a different resolution (from smaller to higher) for the properties in order to reduce the

computational load. The process of upscaling is shown in Figure 5.33. It can be seen that the red parts of the distribution (well logs) are redistributed among the upscaled cells.

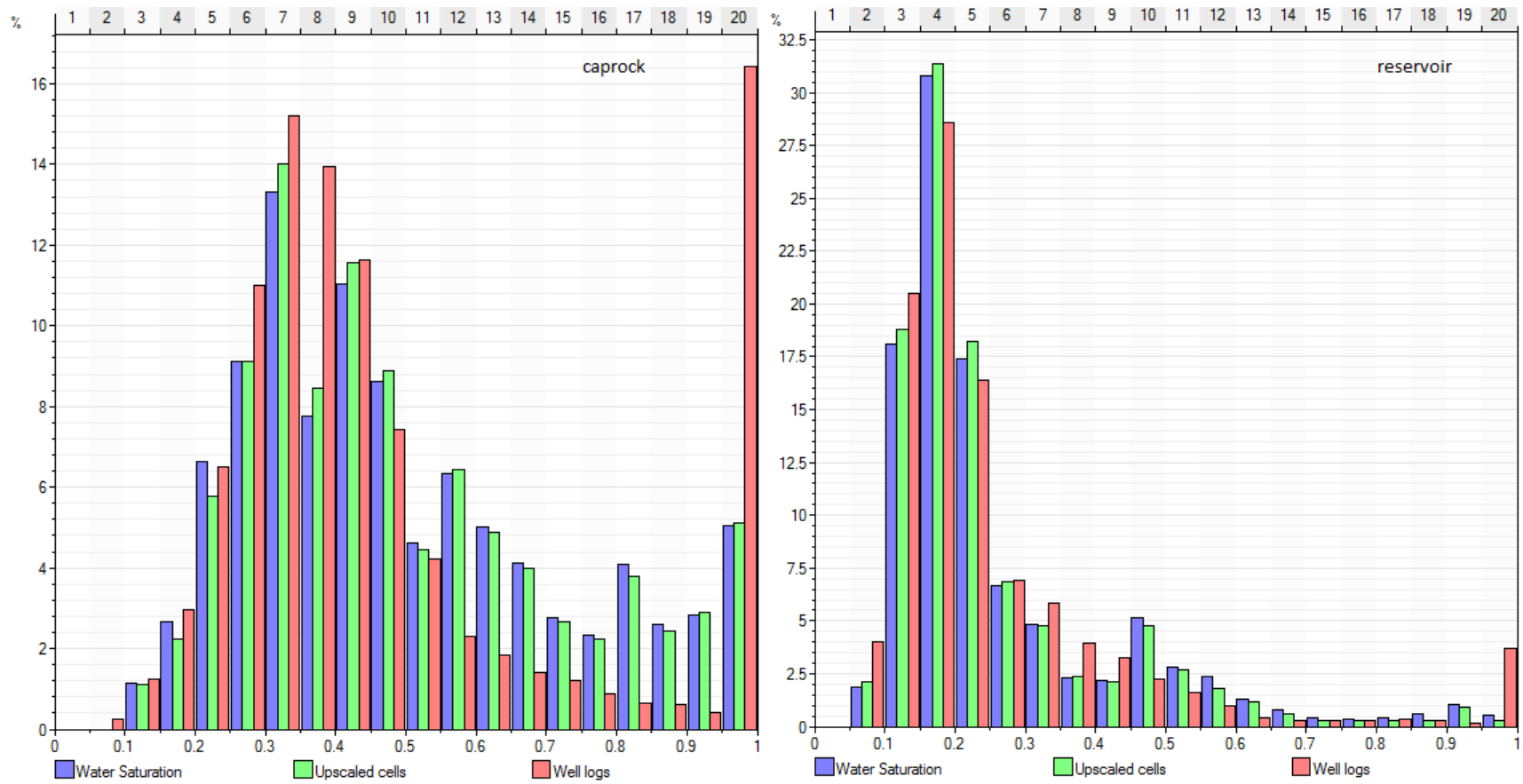


Figure 5.33: Upscaled and non-upscaled distribution of water saturation for the caprock (on the left) and the reservoir (on the right). Red color shows the well logs, green color the cells after the upscaling process.

Table 5.7: Cell properties for reservoir and caprock layers in the simulation model.

Description	Reservoir	Caprock
Cells (nI x nJ)	418 × 759	418 × 759
Total number of 2D cells	318440	317262
Total number of 3D cells	11104170	14276790
Average thickness of one cell (ft)	7.444	6.875

Two regions of interest: reservoir and caprock were populated with a grid, where the individual cells were created. The data can be seen in Table 5.7

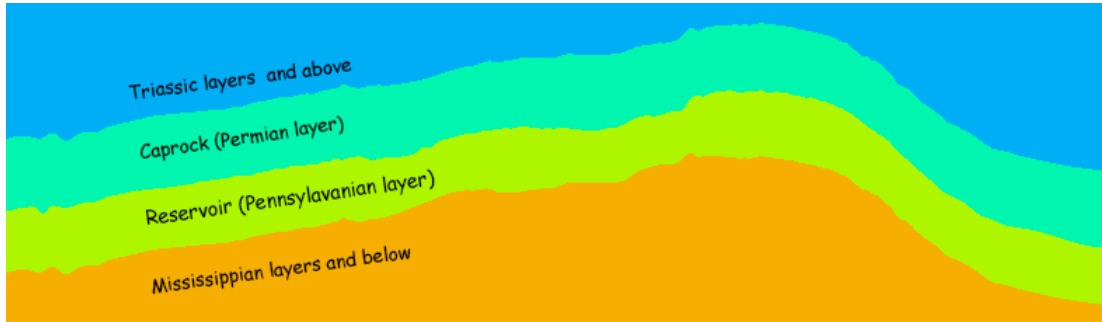


Figure 5.34: Cross-section of the area of interest. Layers' thickness is not correlated to actual thickness.

5.6.2 Property Modelling

As mentioned in previous section, a skeleton model for the layers was made. The next step was filling this model with interpolated data, based on the upscaled properties and Gaussian distribution. Figures 5.35 - 5.52 present the 2D and 3D figures for the selected properties.

Pore Pressure

Figure 5.35 indicates that the pore pressure values in the reservoir range from approximately 2400 to 2550 psi (color scale: light blue to red). As can be observed, the top and bottom of the reservoir are shown, and it is apparent that the lower part of the reservoir delineates higher pore pressure values, especially around the central-south region of the reservoir. Tops of the reservoir indicate lower pore pressure values, as the zone is more shallower than the bottom of the reservoir. With respect to CO₂ injection, an area of smaller pore pressure (color scale: light blue/green) is preferred.

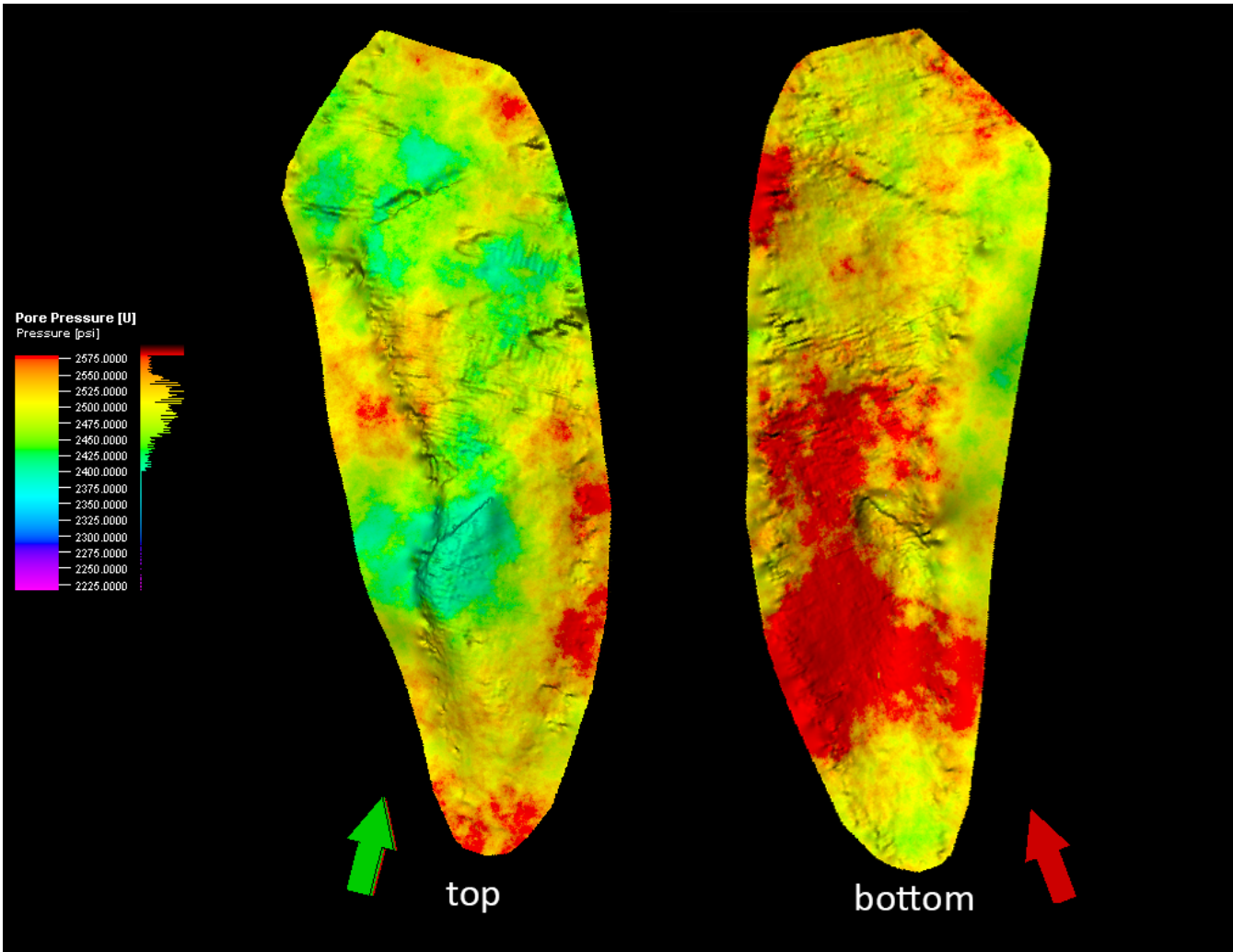


Figure 5.35: 3D property model for pore pressure in the reservoir area with views from the top and the bottom.

Permeability

Figures 5.36 and 5.37 characterise the distribution of permeability on the tops of the caprock and the reservoir. By inspecting the top of the caprock model, it can be seen that the permeability values range mainly from extremely low values (approximately 1×10^{-10} mD) to fairly high values (approximately 0.1 mD). With respect to CO₂ injection process, the caprock with a lower permeability is desirable, so the points of interest in the caprock model are coloured with the scale of purple/blue/light blue/green/yellow. The central and southern parts of the caprock represent the lowest permeability values.

By inspecting reservoir model and comparing it to the top of the caprock model, it is apparent that the reservoir has more permeable zones. The permeability values on the top of the reservoir range from green to red (0.0001 to 10 mD), and with respect to CO₂ injection the high permeability zones are more suited. Most of the reservoir area has a high permeability value (color scale: red/orange), except the middle-central part (color scale: purple/green/yellow).

Figure 5.38 indicates the change of permeability by looking at the cross section from the west view. The change of permeability can be seen as the layers go from the caprock zone to the reservoir zone, with a distinctive line in the center, marking the end of the caprock and the start of the reservoir. As mentioned before, the majority of the caprock is practically impermeable (color scale: purple/blue/green/yellow), while the reservoir is predominantly orange and red, indicating a higher permeability, thus favourable flow characteristics.

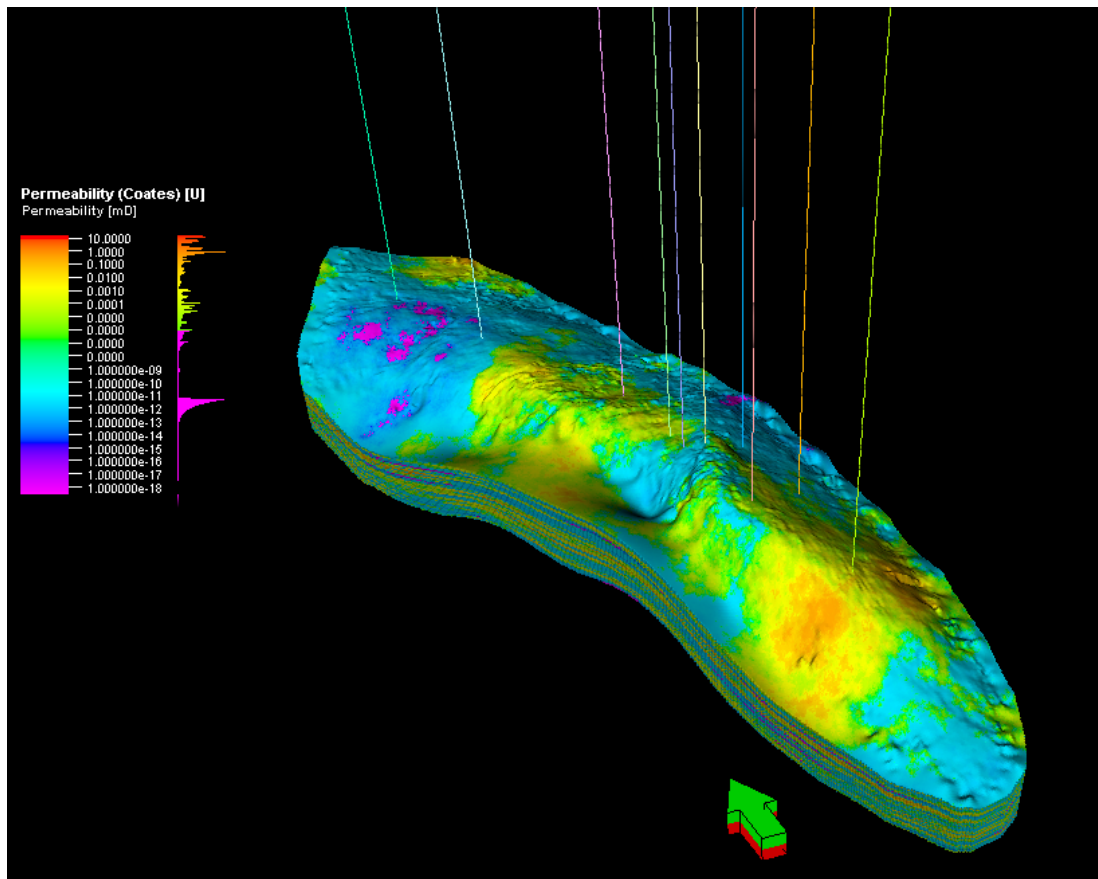


Figure 5.36: 3D property model for permeability in the caprock (Permian layer). North to South direction with all the well locations.

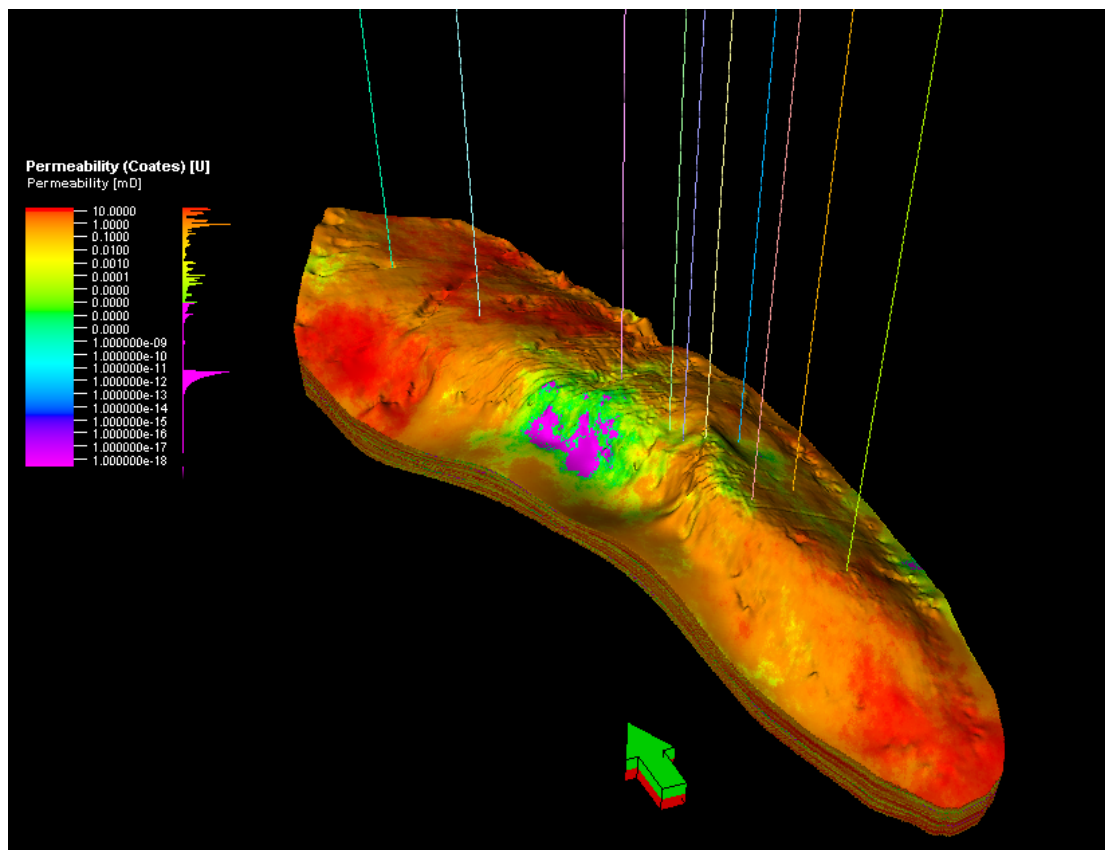


Figure 5.37: 3D property model for permeability in the reservoir (Pennsylvanian layer). North to South direction with all the well locations.

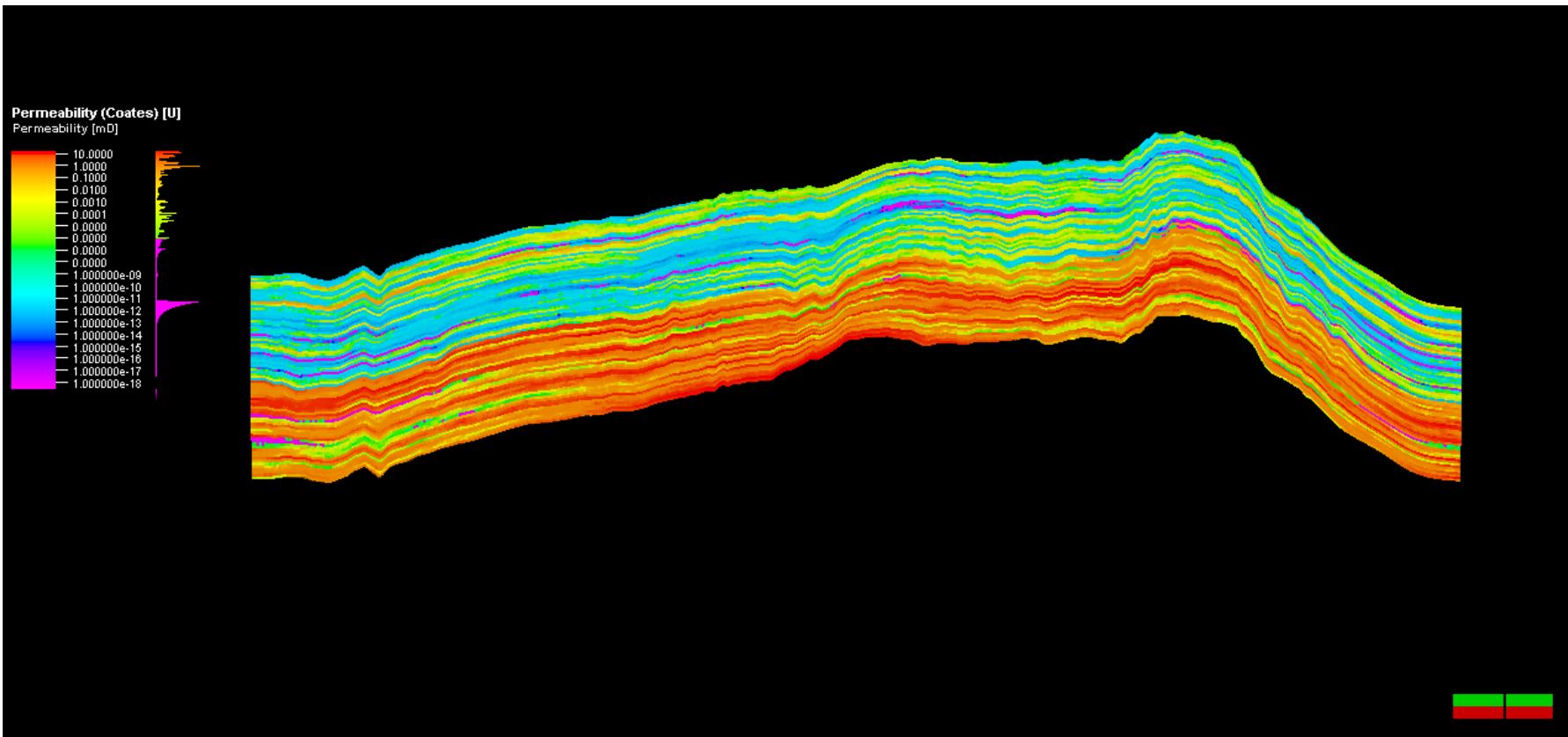


Figure 5.38: Cross-section for permeability in the caprock (Permian layer) and reservoir (Pennsylvanian layer). West view.

Porosity

Figures 5.39 and 5.40 depict the change of porosity across the area of the caprock and the reservoir. As can be inspected in the legends, the majority of values span between 2 to 17 % (color scale: purple to light blue/green). By looking at the area of caprock, it can be seen that the northern part of the area has a low porosity, and only the top peak in the center is slightly higher than the average porosity. The very southern tip indicates small areas of much higher porosity values 30% (color scale: yellow/red).

By inspecting the reservoir model, it is clear that the reservoir has much more porous areas than the caprock. The most porous area can be seen in the middle of the formation ranging from north to south. A higher porosity area can also be seen in the very southern tip of the reservoir area. When choosing an injection location, the porosity of the reservoir would be of crucial importance, and the aim would be to inject in the most porous areas (color scale: red/yellow/green).

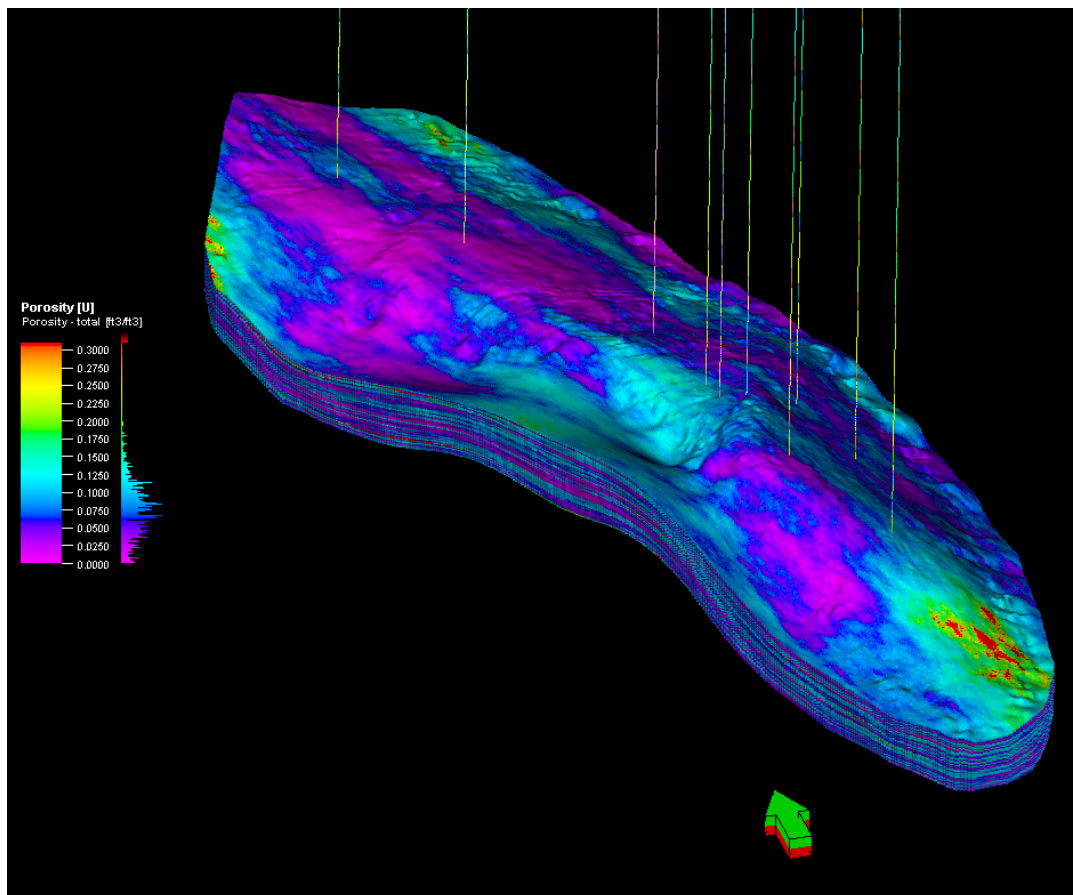


Figure 5.39: 3D property model for porosity in the caprock (Permian layer). North to South direction and the location of all 10 wells.

Volume of Shale

3D model and cross-section for the caprock and reservoir were computed, displaying the zones of the shale volumes. Figure 5.41 is the top of the reservoir and it

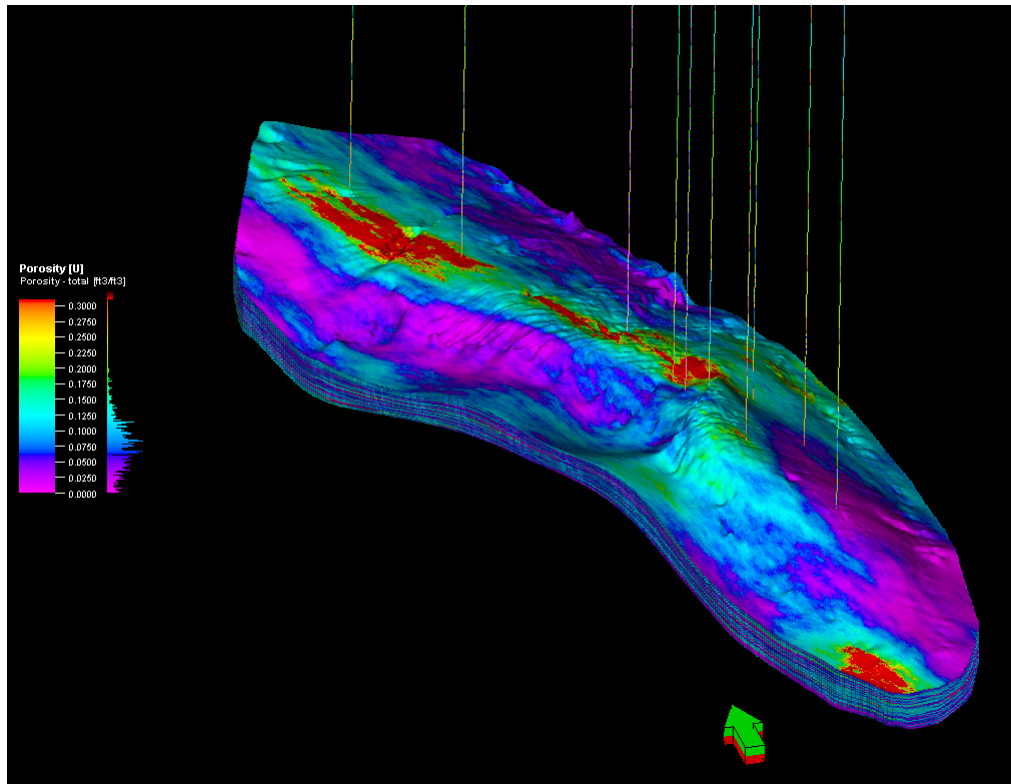


Figure 5.40: 3D property model for porosity in the reservoir (Pennsylvanian layer). North to South direction and the location of all 10 wells.

can be seen that the volume of shale ranges in a wide range from 0 to 1 (v/v) and according to the color scale from blue to red (red being the highest shale volume). It can be seen from the model that the north to south central region has multiple small pockets of high volumes of shale (color scale: red/yellow/green), but the rest of the reservoir is showing no volumes of shale.

It can be observed from Figure 5.42 that the caprock area has a much higher volume of shale present (color scale: green/yellow/red), while the reservoir mainly illustrates lower values of shale volume (color scale: light blue/blue/purple). For CO_2 injection the most important part is the shale volume within the caprock, as shale provides desirable elastic properties, which increases the caprock integrity. With respect to CO_2 injection, the aim should be the injection in the zones below the caprock region with the highest shale volume values (color scale: green/yellow/red).

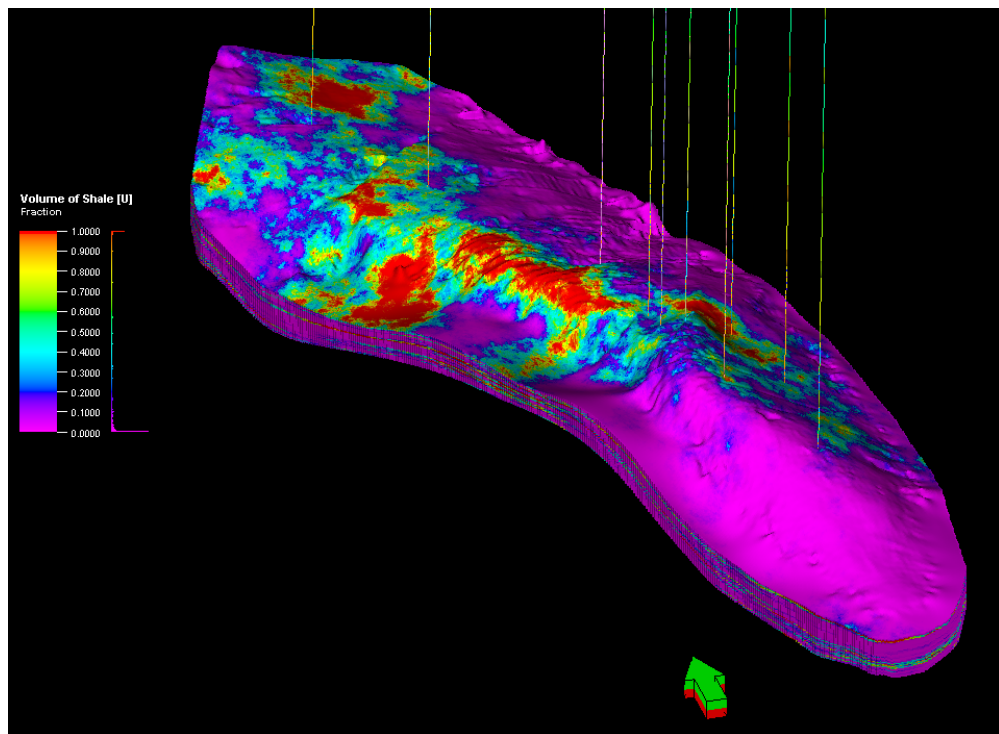


Figure 5.41: 3D property model for the volume of shale in the reservoir (Pennsylvanian layer). North to South direction with the locations of the 10 wells.

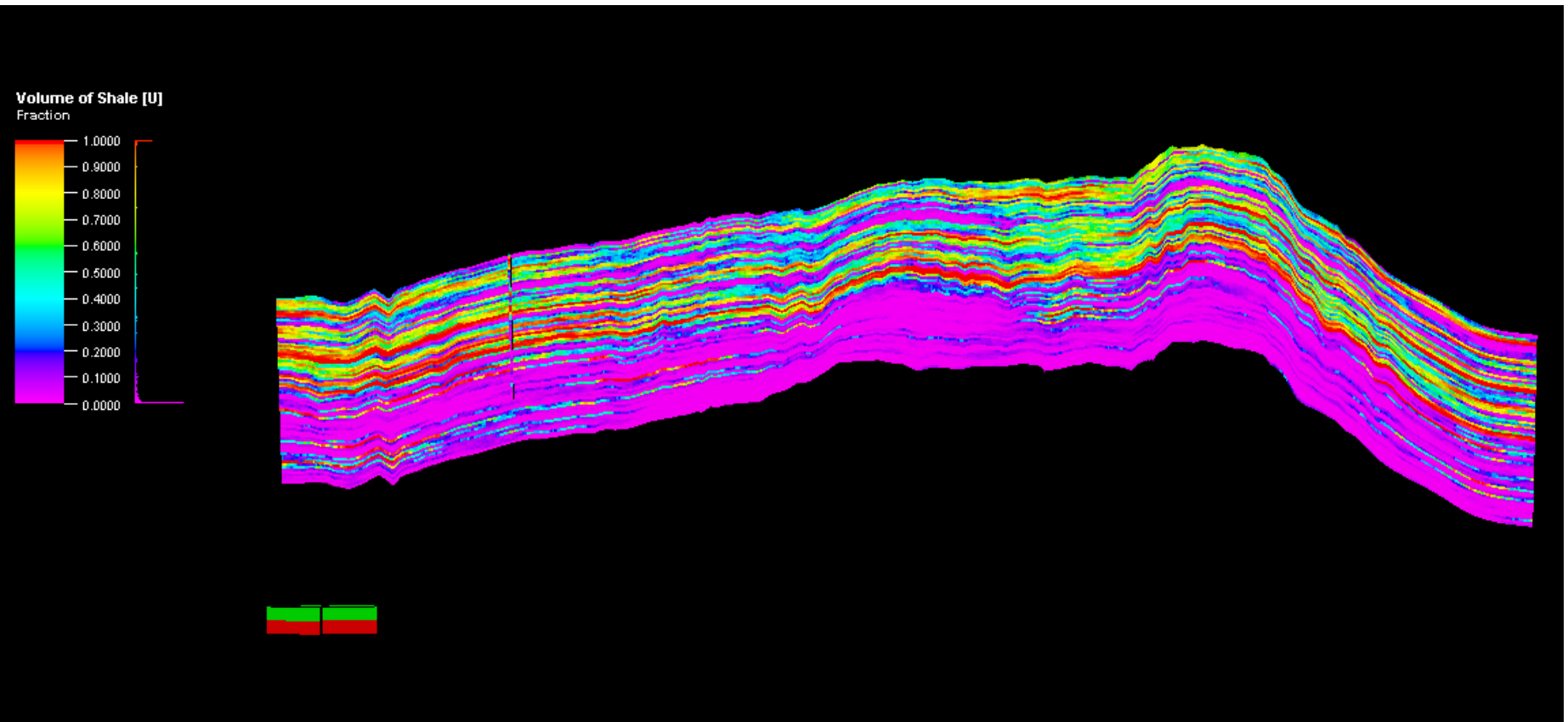


Figure 5.42: Cross-section of the volume of shale in the caprock (Permian layer) and reservoir (Pennsylvanian layer). West side view.

Water Saturation

Figures 5.43 and 5.44 present water saturation and how it changes as a function of area and depth. Figure 5.43 provides a view on the top layers of the reservoir, and as can be seen according to the legend, the majority of values range between from 0.1 to 0.7 (color scale: purple/blue/light blue/green/yellow). However, there are several areas that show higher values of water saturation from 0.7 to 1.0 (color scale: yellow/orange/red). Only the western and southern parts of the reservoir surface indicate high water saturation values (color scale: yellow/orange/red), while the rest of the reservoir area has mainly lower water saturation values (color scale: purple/blue/light blue). By inspecting the cross-section for both the caprock and reservoir in Figure 5.44, it can be noticed that the caprock displays higher values of water saturation (color scale: green/yellow/orange/red), in comparison to the reservoir values (color scale: purple/blue/light blue). Higher water saturation values in the caprock are due to the higher volume of shale present, as presented in Figure 5.42.

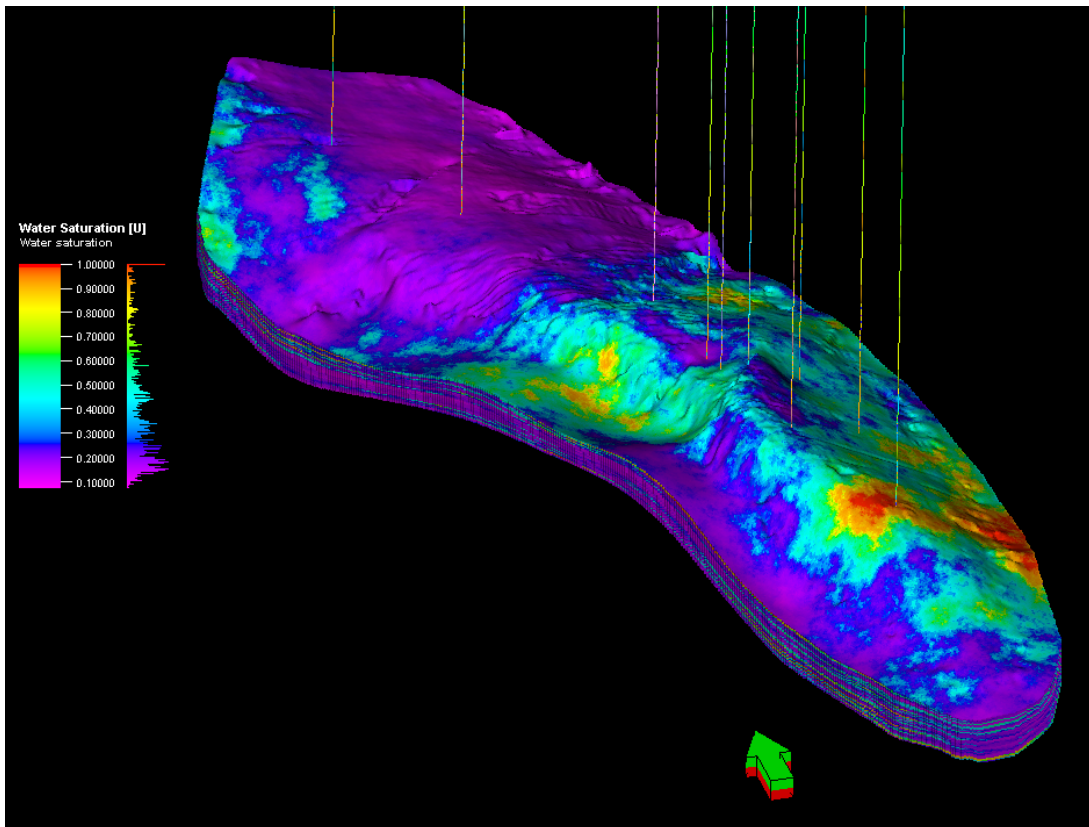


Figure 5.43: 3D property model for water saturation in the reservoir (Pennsylvanian layer). North to South view with all the locations of the wells.

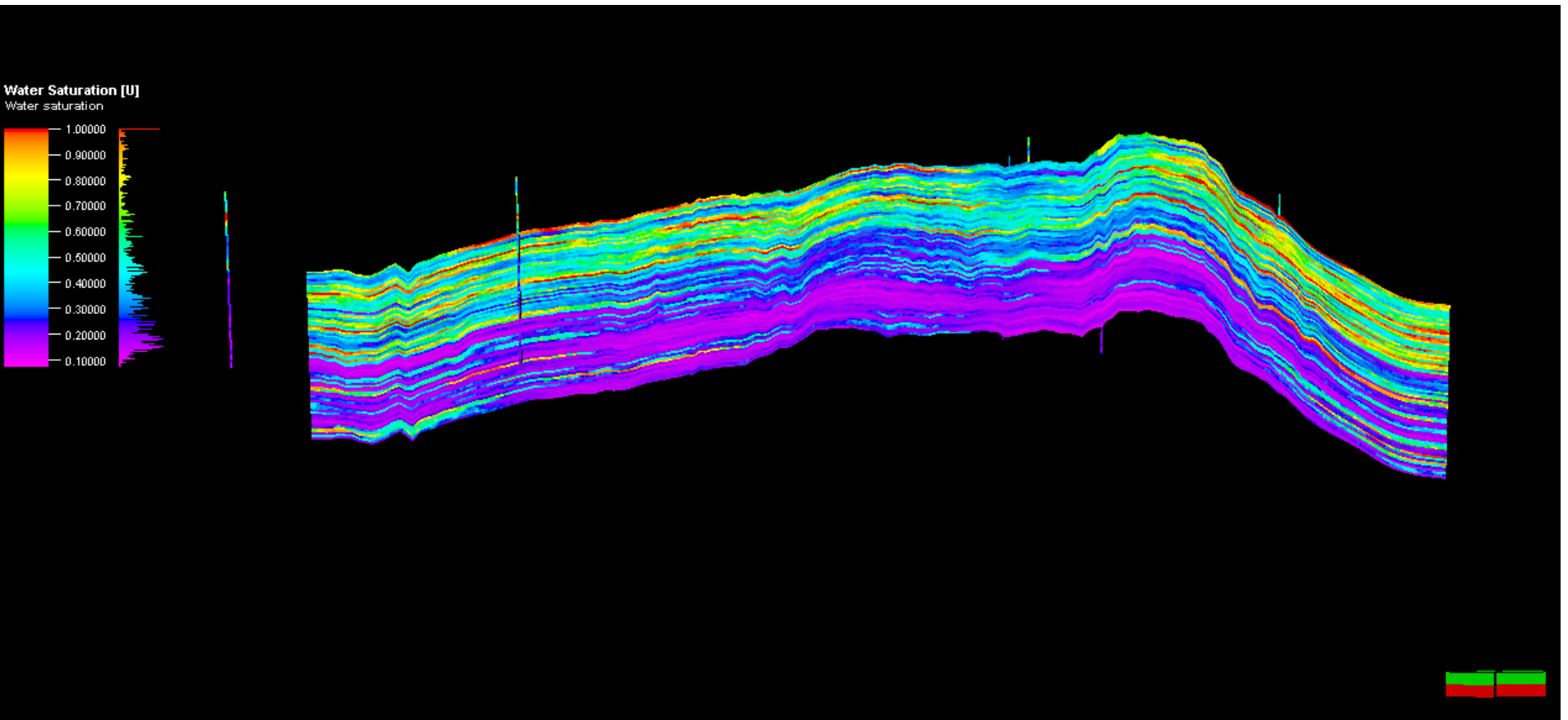


Figure 5.44: Cross-section of water saturation in the caprock (Permian layer) and reservoir (Pennsylvanian layer). West side view.

Fraction Gradient

Figure 5.45 illustrates a significant property of the caprock, which is the fracture gradient. As seen in the legend, the change of values is not remarkable (from 12.05 to 12.70 psi/ft), however it is still of importance to see which zones are more resistant to fracturing. The majority of the top of the caprock is in the range of 12.5 to 12.6 psi/ft (color scale: green/yellow/orange). The highest values can be seen in the southern part of the caprock, while the mid-center and northern part depicts slightly lower values (color scale: purple/blue/ light blue). Regarding CO₂ injection, the area with the highest fracture gradient is most preferable, because of the possibility to have a higher injection pressure for CO₂.

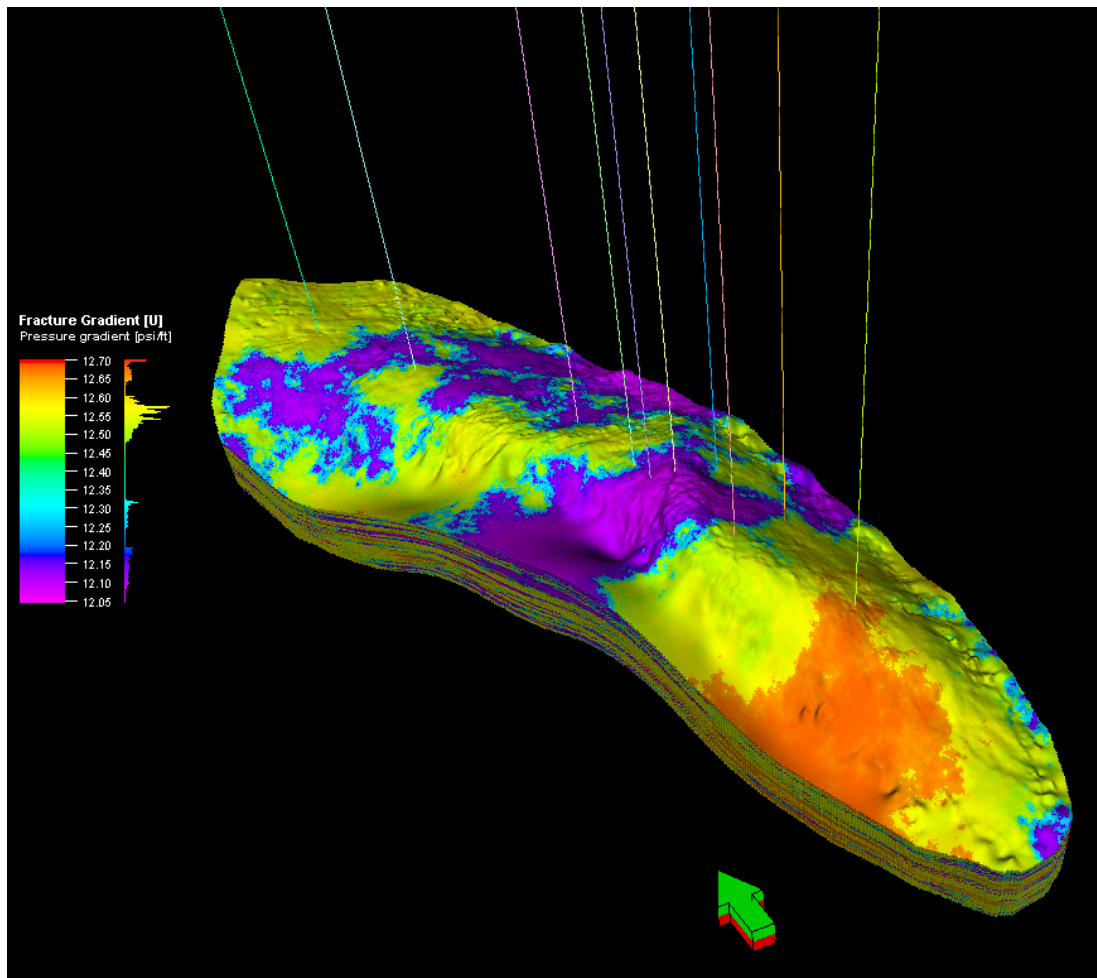


Figure 5.45: 3D property model for fracture gradient in the caprock zone (Permian layer). North to South view with all the locations of the wells.

Vertical Stress

Figure 5.46 illustrates the vertical stress values for the top of the caprock zone. It can be seen that the values vary mainly from 5000 to 6200 psi (color scale: purple/blue/light blue/ green/yellow/orange/red). As can be observed, the majority of the caprock is blue/light blue/green/yellow, with only the southern and easternmost peripheral parts exhibiting higher vertical stress values (color scale:

green/yellow), while the rest of the caprock indicates slightly lower vertical stress values (color scale: purple/blue/light blue). Areas of higher vertical stress are more viable for drilling and CO₂ injection, as they can sustain higher stress. By inspecting the cross section in Figure 5.47, it can be seen that as the depth increases in the caprock, the vertical stress does not change significantly and varies in the color range of blue/light blue/green.

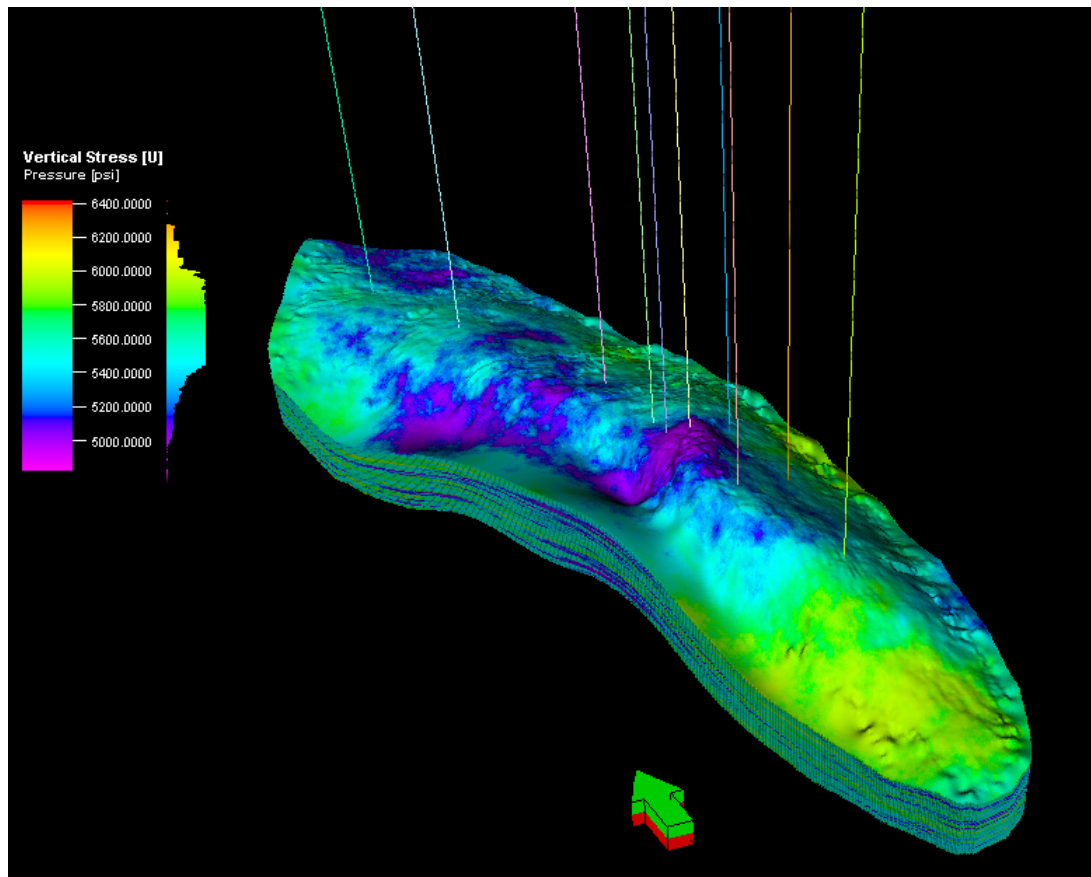


Figure 5.46: 3D property model for vertical stress in the caprock zone (Permian layer). North to South view with all the locations of the wells.

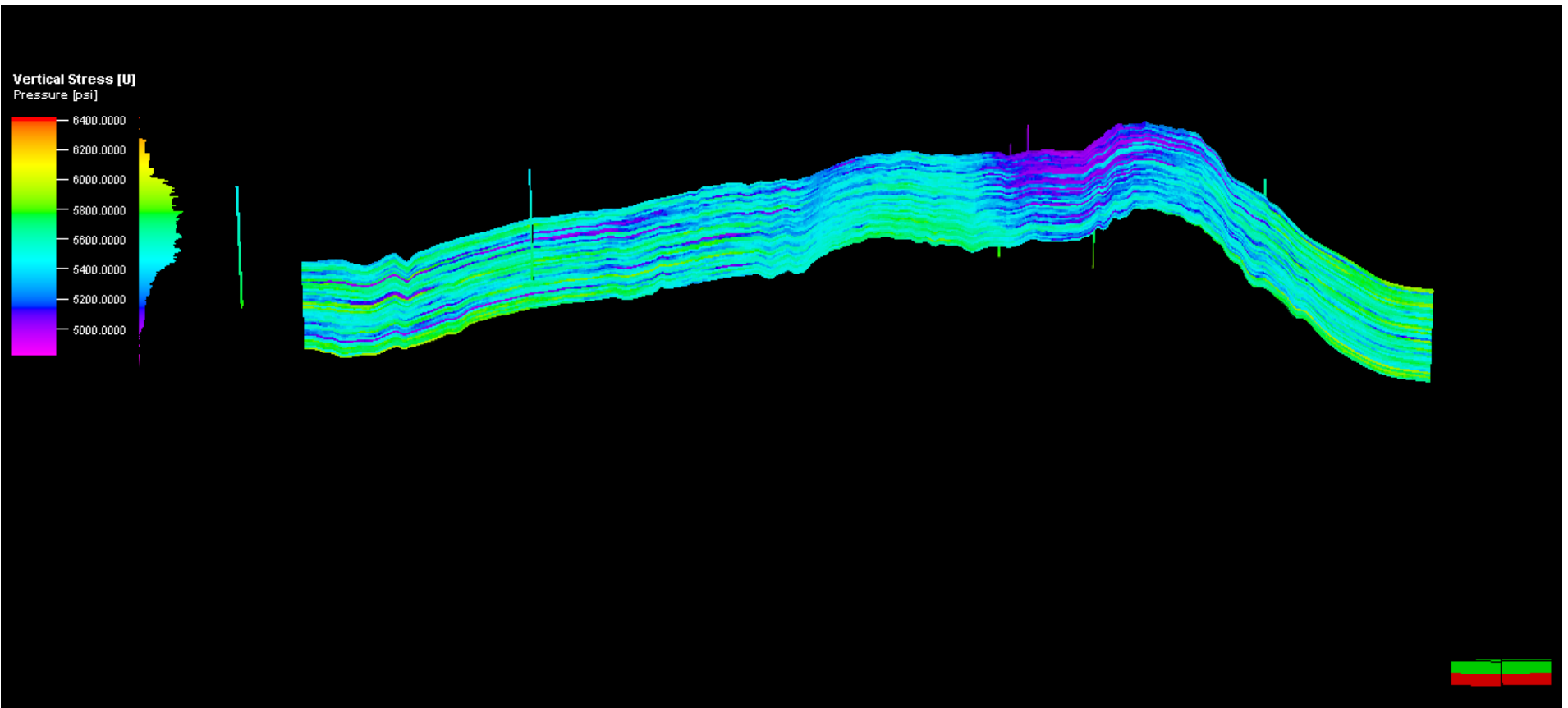


Figure 5.47: Cross section for vertical stress in the caprock zone (Permian layer). West view.

Maximum Horizontal Stress

The values of maximum horizontal stress in the caprock are illustrated in Figure 5.48. Numerical range spans from 3700 to 5200 psi (color scale: purple/blue/light blue/green/yellow/orange). The majority of the caprock ranges around the values of 4500-4800 psi (color scale: green/yellow). Only the northern and east-central parts portray higher values (color scale: yellow/orange) and the west central area has the lowest values (color scale: purple/blue/light blue). Areas with higher maximum horizontal stress values (color scale: yellow/orange) are of bigger interest, as the risk of fracturing, shear failures and cracks is significantly lower in these areas.

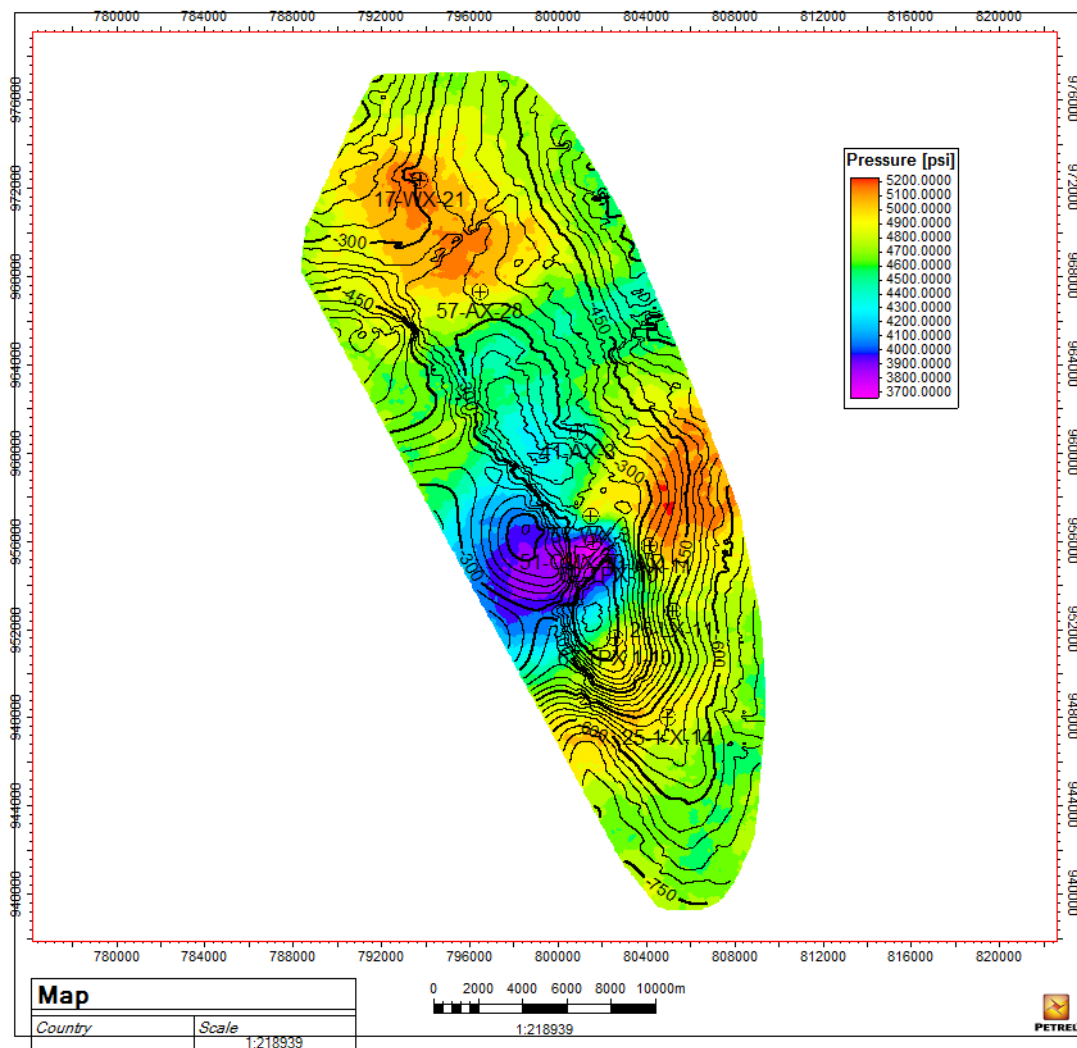


Figure 5.48: 2D property model for the maximum horizontal stress in the caprock zone (Permian layer). North to South view with all the locations of the wells.

Minimum Horizontal Stress

Figure 5.49 depicts the distribution of minimum horizontal stress in the caprock. It can be seen from the 2D map that the majority of values range between 2580 to 2680 psi (color scale: blue/light blue). Only the area in the south-east area has

higher values (color scale: green/yellow/orange/red) while the area to the west of it characterizes the lowest values (color scale: purple/blue). With respect to CO₂ injection, areas with the lowest values (color scale: purple/blue) are preferred.

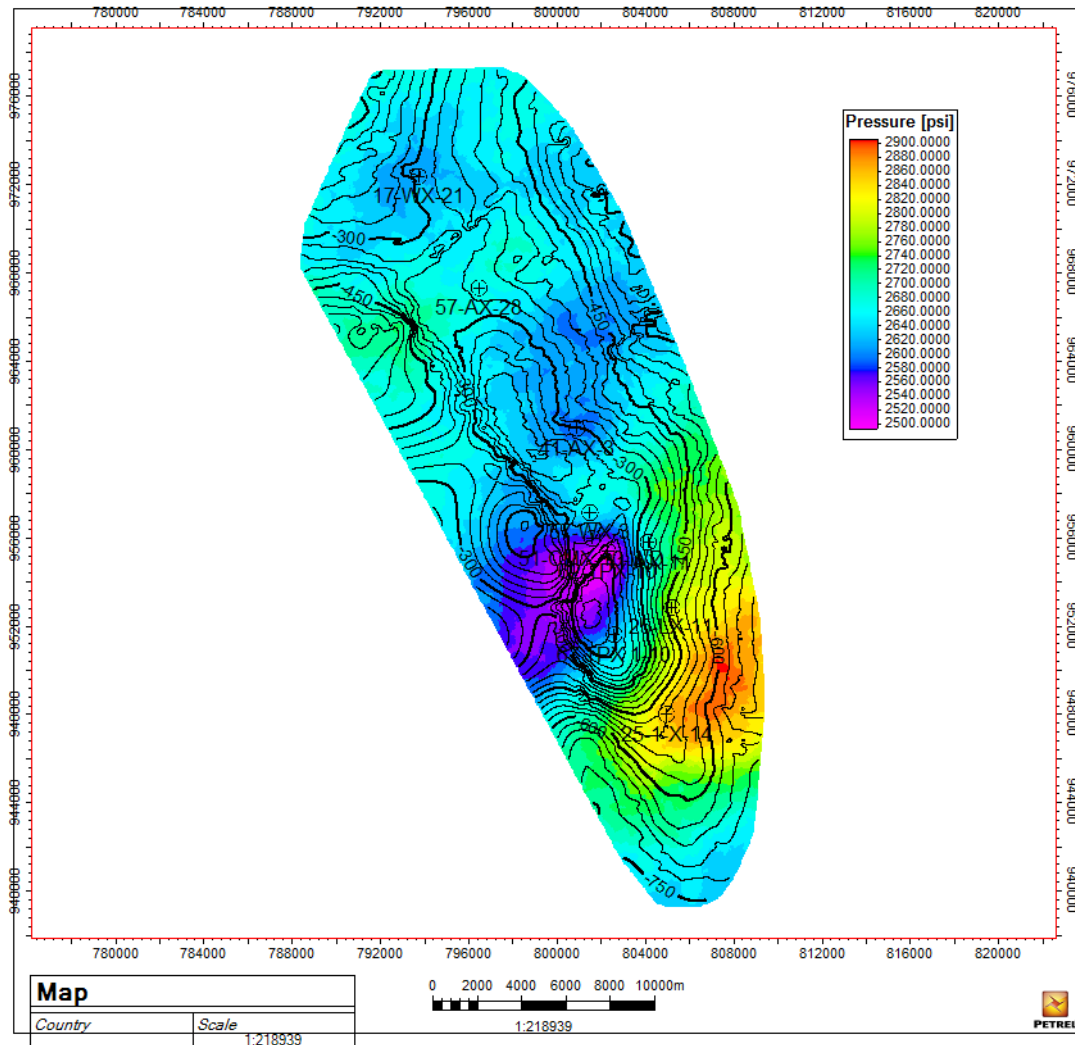


Figure 5.49: 2D property model for the minimum horizontal stress in the caprock zone (Permian layer). North to South view with all the locations of the wells.

Poisson's Ratio

3D model of Poisson's ratio can be seen in Figure 5.50, where it is evident that the majority of values in the caprock ranged from 0.22 to 0.28 (color scale: blue/light blue/green/yellow). Dominant part of the caprock, except a small area in the west-center and east-center depict lower values (color scale: purple/blue/light blue), is more or less homogeneous (color scale: green/yellow). Regarding CO₂ injection, the area with a higher Poisson's ratio (color scale: green/yellow) is more beneficial and desirable, since the seal is more ductile and can withstand more external stress.

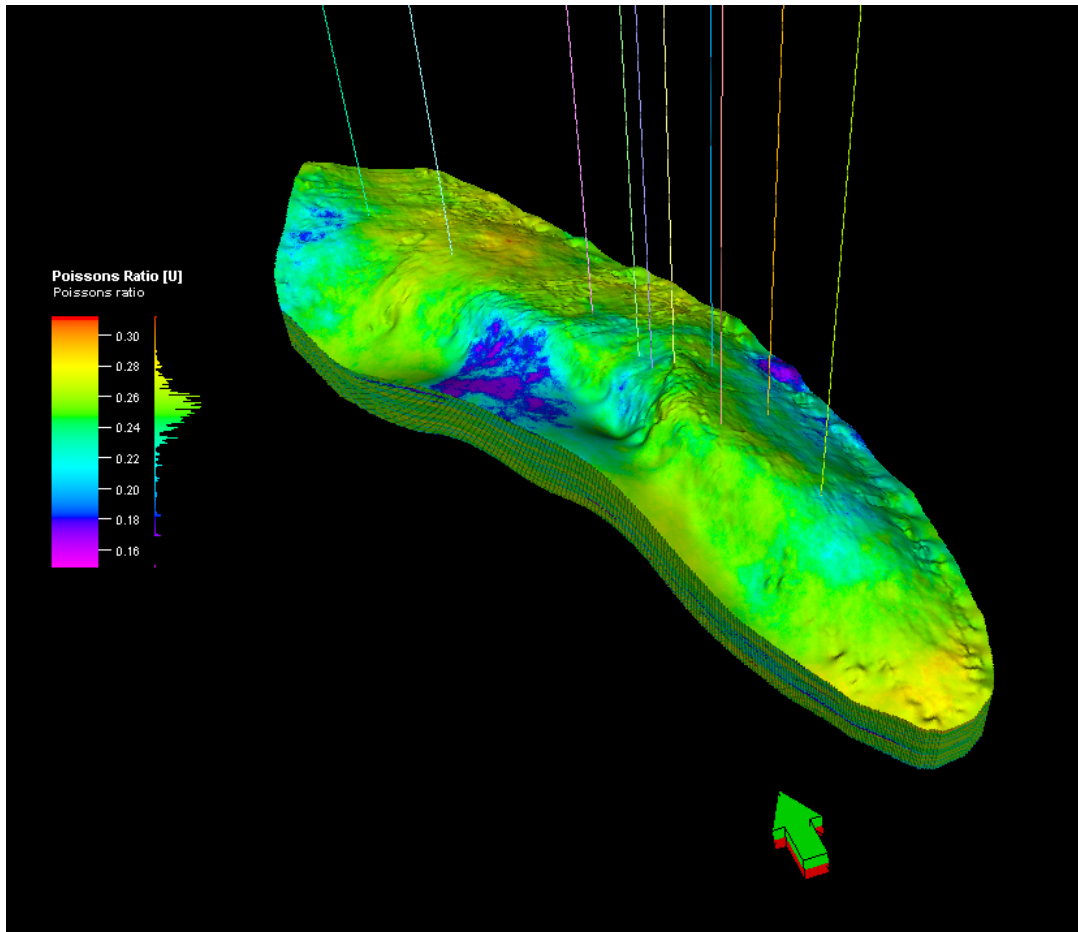


Figure 5.50: 3D property model for Poisson's ratio in the caprock zone (Permian layer). North to South view with all the locations of the wells.

Shear Modulus

From the 3D shear modulus model, it can be seen that for the caprock majority of values ranged from 2 to 5 Mpsi (color scale: blue/light blue/green/yellow). Only the area north of the center of the caprock indicated higher shear modulus values (color scale: yellow/orange/red), while the rest of the caprock is in the same value range (color scale: light blue/green). The area coloured in light blue/green is considered less rigid, and more suitable for CO₂ injection and storage.

Young's Modulus

Figure 5.52 describes the change of Young's modulus as a function of the caprock's area. The values varied mainly in the range of 5 to 12 Mpsi (color scale: blue/light blue/green/yellow). Only the most southern part and a small area in the north-east section indicated higher values (color scale: yellow), while the rest of the caprock is more or less in the same range (color scale: light blue/green). Areas of lower values for Young's modulus are more preferable for CCS due to significantly better elastic properties.

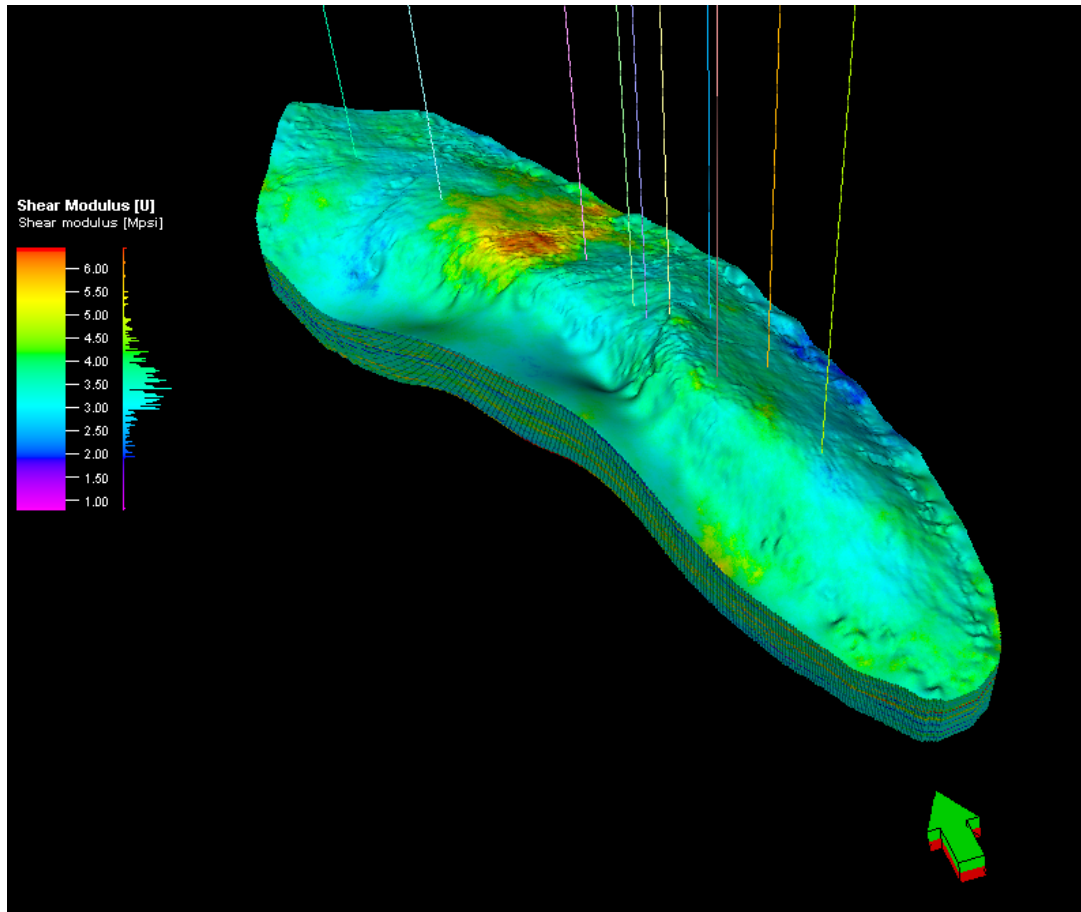


Figure 5.51: 3D property model for shear modulus in the caprock zone (Permian layer) north to south view with all the locations of the wells.

5.6.3 Volume Calculation

The properties that were used are described in Table 5.8. It can be seen that OWC was used in order to describe the correct amount of free space in the depleted reservoir. Final calculated volume was decreased by a factor of 10% to take into account the amount of formation water that is replacing the void space in the anticline. The final results of the volume calculation are presented in Table 5.9.

Table 5.8: Key properties used for volumetric calculation in Petrel[©].

Property	Value
NTG	0.9353
Bo	1.1 RB/STB
RF	0.5
OWC	-400 ft

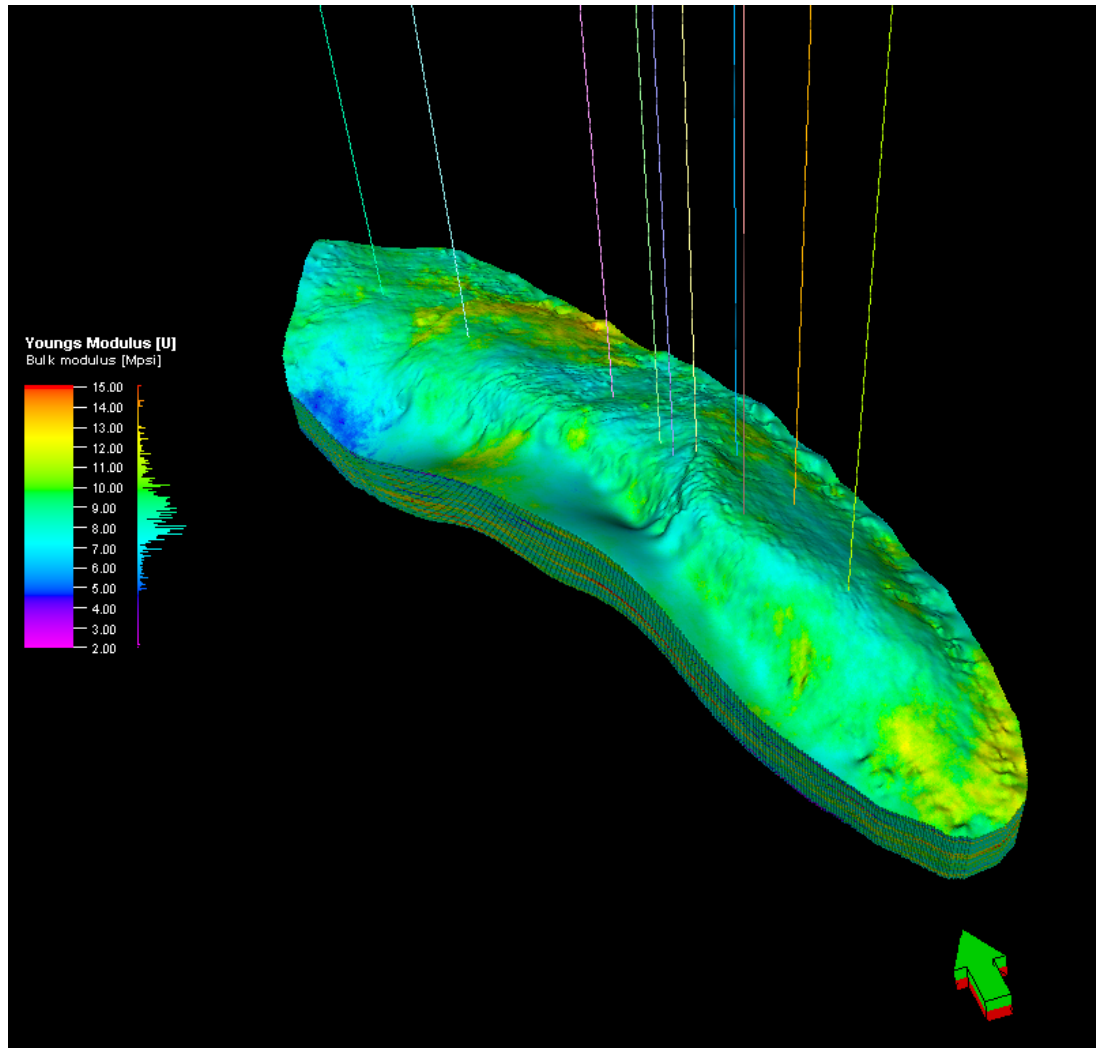


Figure 5.52: 3D property model for Young's modulus in the caprock zone (Permian layer) north to south view with all the locations of the wells.

5.6.4 Well Selection Process

Well selection is based on both the properties of the caprock and the reservoir. By developing a suitable algorithm and taking into account the two, most optimal CO₂ injection location can be estimated. In the scope of our thesis it was decided that the properties of the caprock will play a more indicative role in well selection, in order to ensure the safety of the injection process and the integrity of the caprock. It was decided, based on the 2D property maps, which of the existing wells meet the criteria set by us and are suitable to carry out CO₂ injection and its consequent storage. Figure 5.54 graphically illustrates the selection process flow diagram. It can be seen that the selection process is divided into criteria of (i) the caprock and the criteria of (ii) the reservoir. In case of the caprock, brittleness and ductility is estimated by the means of elastic properties. Consequently, the ductility maps are generated. At the same time the reservoir constraints are evaluated - by means HCPV and volume calculation. These two values are put together on a single map and after which the effectiveness of the constraints is evaluated.

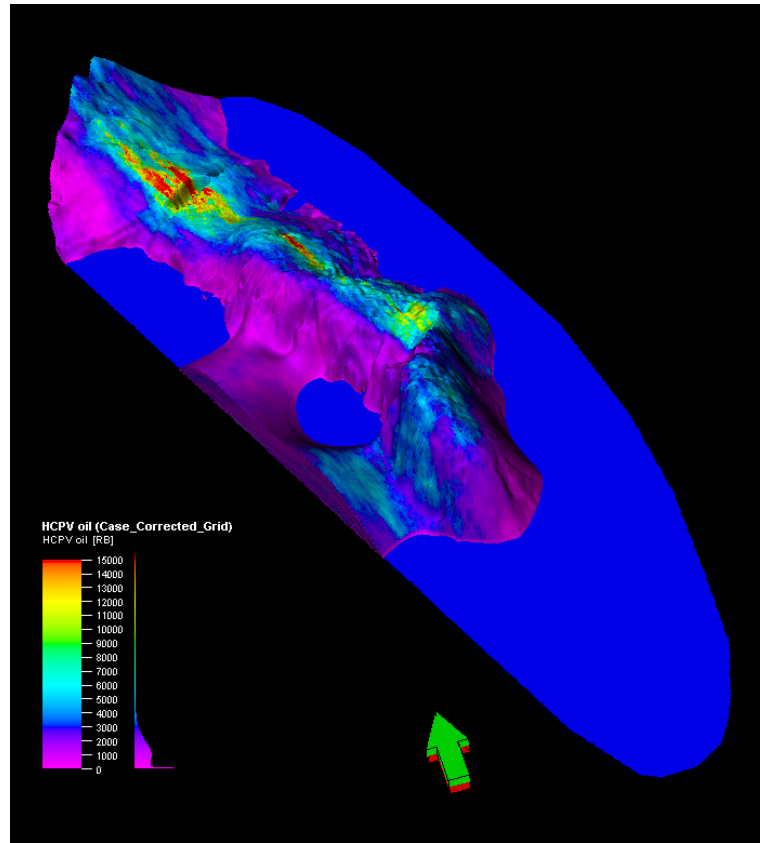


Figure 5.53: Volume calculation with OWC. Blue plane depicts the OWC. Area above the plane is the basis for the volume calculation.

Table 5.9: Results of the volume calculation for reservoir area in Petrel[©].

Property	Value	Unit
Bulk Volume	6.378×10^9	m^3
Net Volume	6.629×10^9	m^3
Pore Volume	5.12×10^8	sm^3
HCPV oil	2.417×10^9	RB
STOIIP	2.197×10^9	STB

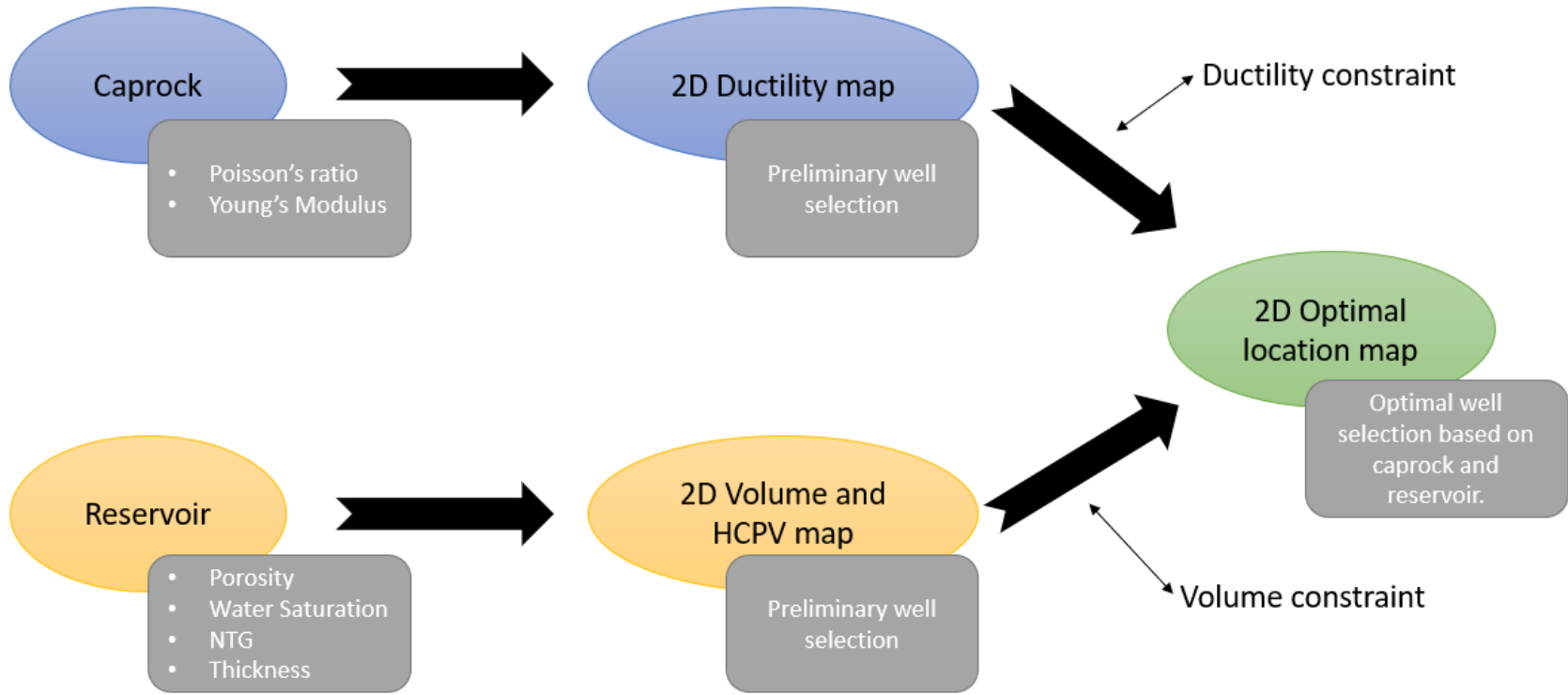


Figure 5.54: Process flow diagram explaining the procedure for the selection of the optimal injection well.

Caprock

As mentioned previously, the integrity of the caprock was considered more important than the conditions in the reservoir. Regarding the selection of the well, taking into account the caprock's properties (Young's modulus, Poisson's ratio etc.) a 2D map (Figure 5.55) illustrating the ductility and brittleness of the caprock was made in Petrel[©]. This map illustrates the most ductile regions of the caprock (color scale: green/yellow/orange). Color change from yellow to purple, the ductility decreases, indicating a more brittle caprock. This also signifies the fact that Poisson's ratio decreases, as was depicted in Figure 5.32. As the map also shows the locations of the well, first step of the selection process (which is based on the caprock properties) can be carried out, and as depicted on a 2D map, only wells 11-AX-11, 41-AX-3, 57-AX-23, 17-WX-21 should be considered for CO₂ injection, as these wells are in the most ductile regions of the caprock. Out of the selected wells, 17-WX-21 (color scale: yellow/orange) and 11-AX-11 (color scale: yellow/green) have the highest ductility. Note the cut-off of the legend at 0.42 (maximum value).

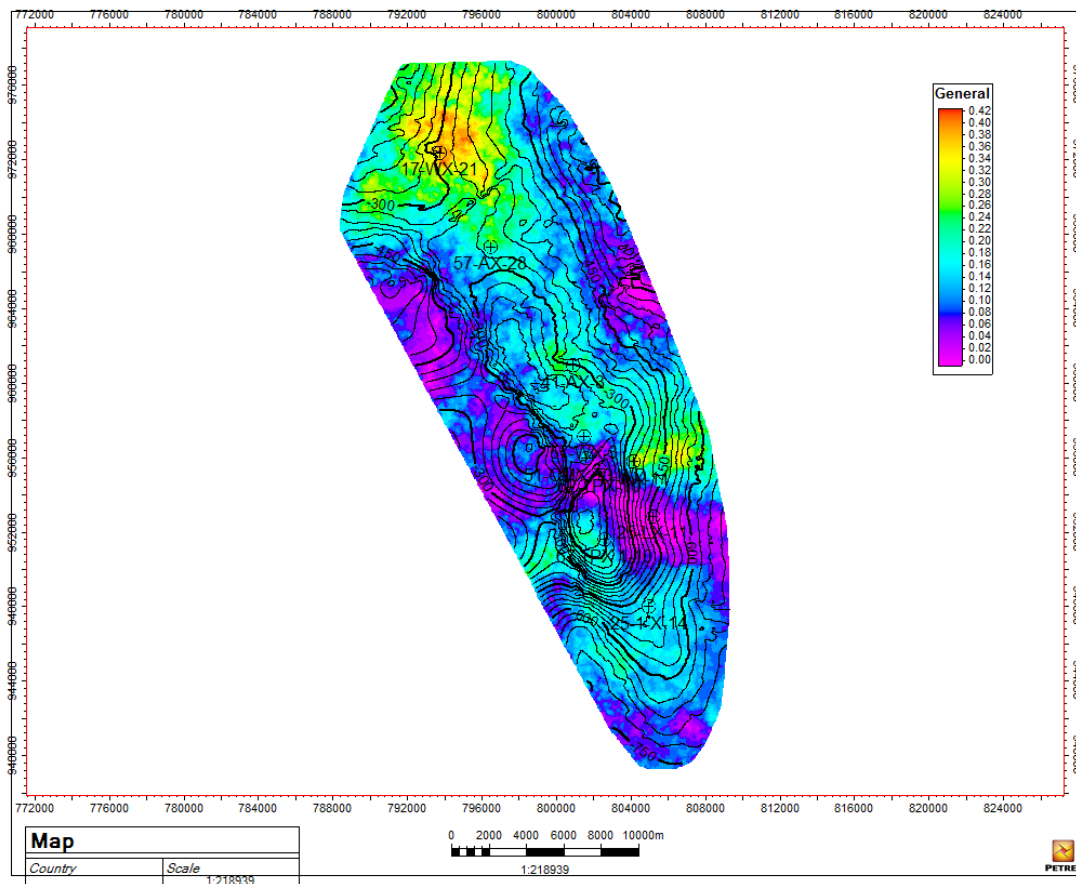


Figure 5.55: 2D map showcasing the areas of ductile and brittle zones in the caprock (Permian layer).

Reservoir

Well selection based on the reservoir properties was carried by implementing the volume calculation technique explained in Chapter 5.6.3. Volume maps are eligible for optimum well selection due to the fact that the calculation of the volume involves important parameters for oil reservoirs, such as: porosity, water saturation and NTG. Two 2D maps (Figures 5.56-5.57) were made presenting the overall volume in the reservoir and the HCPV. Both of these maps also illustrate the structures within the reservoir, that have the highest volume. Looking at Figure 5.56, the distribution of volume above the OWC can be seen, with three distinctive structures at the north, middle-center, middle southern areas (color scale: green/yellow/orange/red).

With the well locations in place, first base selection on the highest volume area can be made. With respect to that, wells 67-TPX 1-10, 41-AX-3, 17-WX-21 look most suitable for CO₂ storage. Figure 5.57 shows HCPV that indicates the locations where the most oil was accumulated within the volume of the reservoir. Comparing HCPV map with the reservoir volume map, it can be seen that the HCPV map also depicts 3 distinctive structures within the reservoir. Within these structures it can be seen the the HCPV is higher than in the rest of the reservoir (color scale: green/yellow/orange/red). Taking that into account, a more precise selection of the wells can be made, aiming for the volumes that had the most oil within them. Based on that the most optimal well for CO₂ storage are 67-TPX 1-10, 57-WX-3, 41-AX-3, 57-AX-28 and 17-WX-21 as they are all in the highest HCPV range (color scale: green/yellow/orange).

Well Selection by Integrating Estimated Caprock and Reservoir Properties

Figures 5.58-5.63 display the optimal areas for CO₂ injection and storage. The optimal area is displayed in red colour, while the yellow colour indicates areas that do not meet the set constraints. For all the 2D maps, values are created to be binary (1 or 0), where 1 is red (favourable conditions) and 0 is yellow (cautionary conditions). These scales apply to all the six constraints that are used in the scope of our thesis (shown in Table 5.10) and 2D maps combine the ductility-brittleness map (Figures 5.55) and the HCPV map (Figure 5.57) into one piece.

It was decided to keep one variable constant while changing the other one. Thus, cases 1, 2 and 3 have a constant constraint for ductility, while the HCPV is changing. Cases 4, 5, 6 have a constant constraint of HCPV, but a changing ductility value. It must be noted that the values for HCPV and ductility have been set according to the scales from the 2D maps for HPCV and ductility (Figure 5.55 and 5.57). The values of all the applied constraints for all the six cases can be seen in Table 5.10.

By comparing Figures 5.58-5.63, it becomes evident that mainly the northern part of the region is suitable for CO₂ injection and storage, according to the mentioned

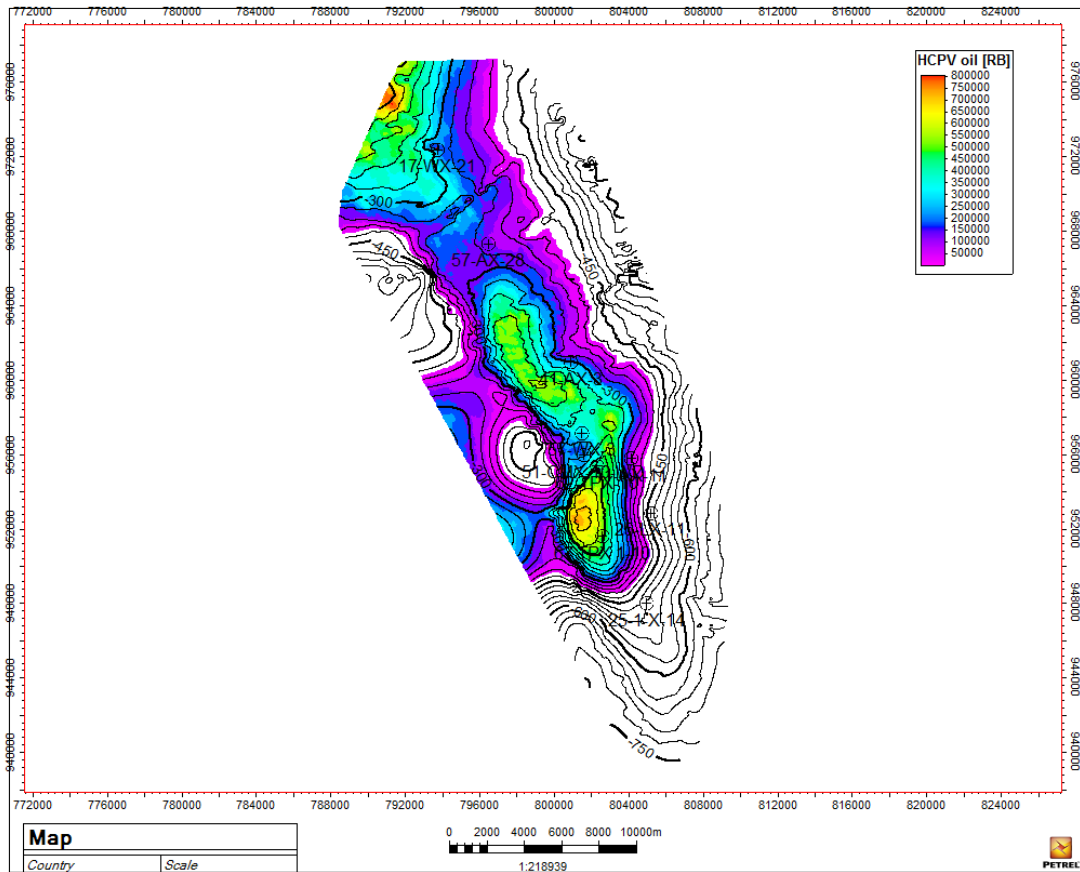


Figure 5.56: 2D map of the areas with the highest volumes in the reservoir (Pennsylvanian layer).

constraints. As mentioned beforehand, the integrity of the caprock was considered of utmost importance, hence the ductility constraint does not go below 0.20 (green coloured areas in Figure 5.55). Cases that had the highest constraints (cases 1 and 4) illustrated very small red areas that are optimal for injection and storage of CO_2 , while cases with the smallest constraints presented much bigger red areas (case 3 and 6). The widest red zone (favourable location) is achieved in case 3, while the narrowest red zone is seen in case 1.

With respect to the well selection, it is indisputable from cases 2, 3, 4, 5, 6 that only well 17-WX-21 is suitable for CO_2 injection, as it is the only well in the area, that is considered to have optimal conditions for both the caprock and the

Table 5.10: Constraint values for well selection

Case Nr.	HCPV	Ductility
1	≥ 3000	≥ 0.20
2	≥ 2500	≥ 0.20
3	≥ 2000	≥ 0.20
4	≥ 2250	≥ 0.35
5	≥ 2250	≥ 0.30
6	≥ 2250	≥ 0.25

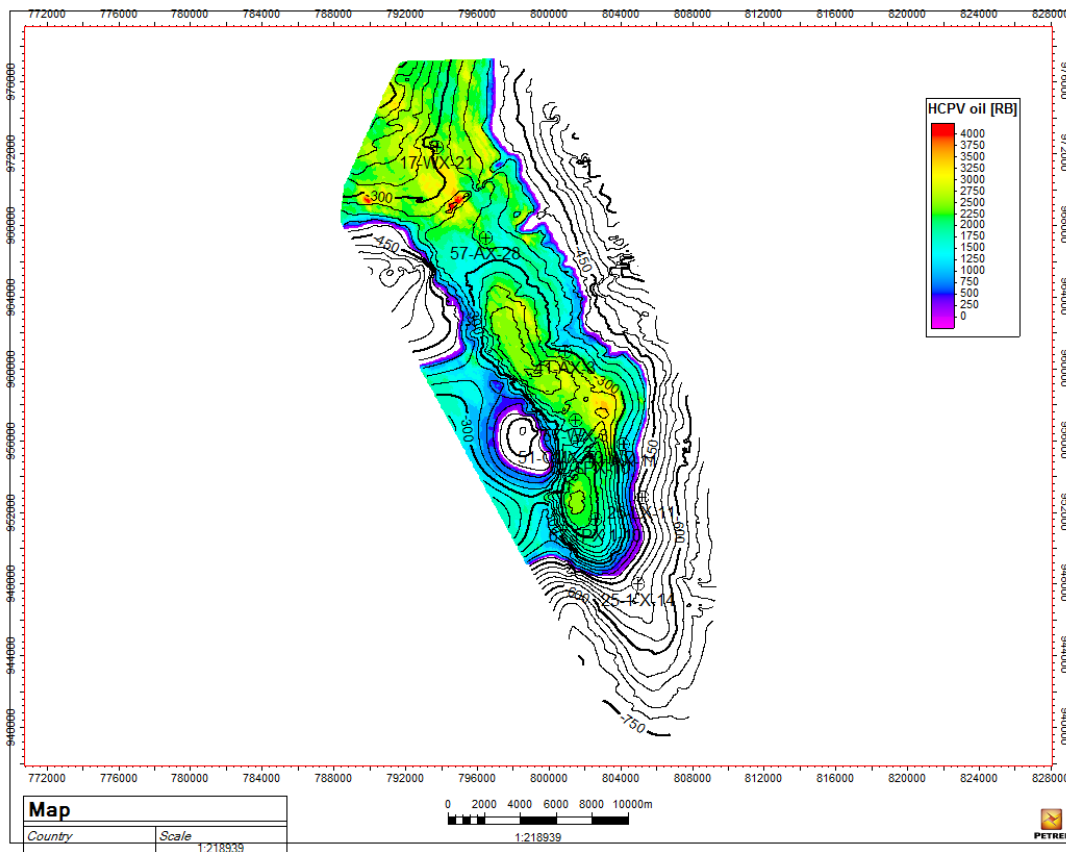


Figure 5.57: 2D map of the areas with the highest hydrocarbon pore volumes in the reservoir (Pennsylvanian layer).

reservoir, taking into consideration the presented constraints.

5.6.5 Capacity Calculation

Capacity calculation was performed based on the methodology described in Chapter 5.6.5. The values used in Equation 2.4 are shown in Table 5.11. CO_2 density was assumed to be 700 kg/m^3 , based on Schuppers *et al.* [8]. Additionally, it was decided that a probabilistic (range of probabilities) approach describes the nature of the value better than a deterministic approach (one calculated value), due to a stochastic nature of all the properties involved. Thus, the cumulative probability figure depicting the P10, P50 and P90 percentiles (which show a statistical confidence level for an estimate) was obtained using the SipMath v3.4.9 MS Excel Add-On [51] and Myerson distribution, which is a generalisation of normal and lognormal distribution. P10, P50 and P90 values are 84.4, 168.7 and 253.3 Mt, respectively. P50 is considered a good middle estimate.

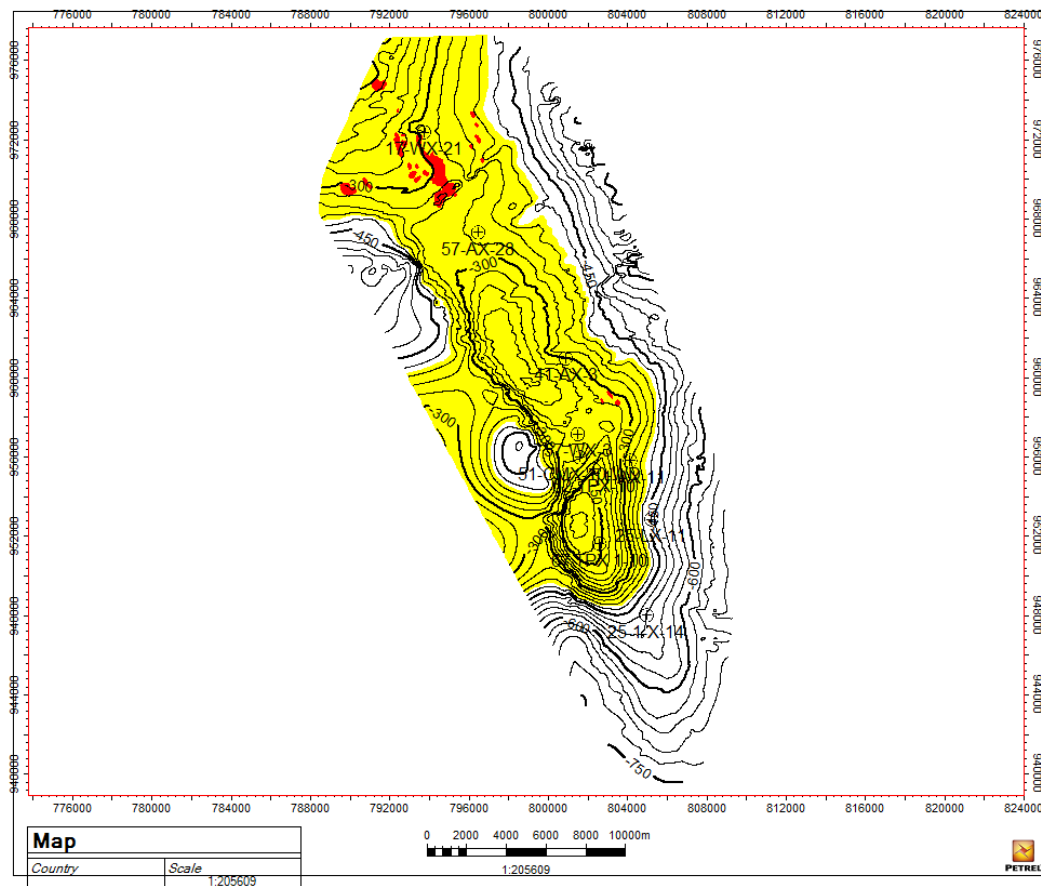


Figure 5.58: 2D map of the areas with the most optimal conditions for CO₂ injection and storage for Case 1. High HCPV constraint, constant ductility.

Table 5.11: Properties used for the computation of storage capacity in Equation 2.4.

Property	Value
Average porosity	0.09
Bulk volume	$6.378 \times 10^9 m^3$
Recovery factor	0.5
CO ₂ density	700 kg/m ³
Average S_w	0.1595

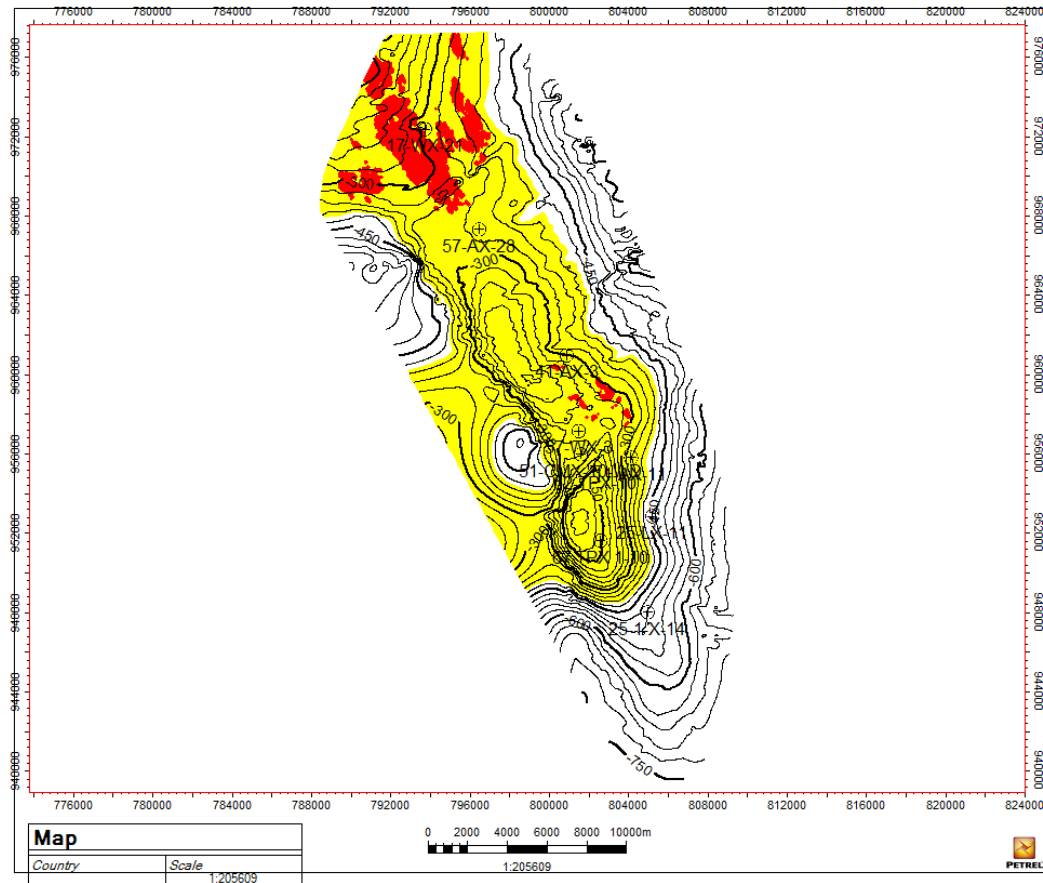


Figure 5.59: 2D map of the areas with the most optimal conditions for CO₂ injection and storage for Case 2. Medium HCPV constraint, constant ductility.

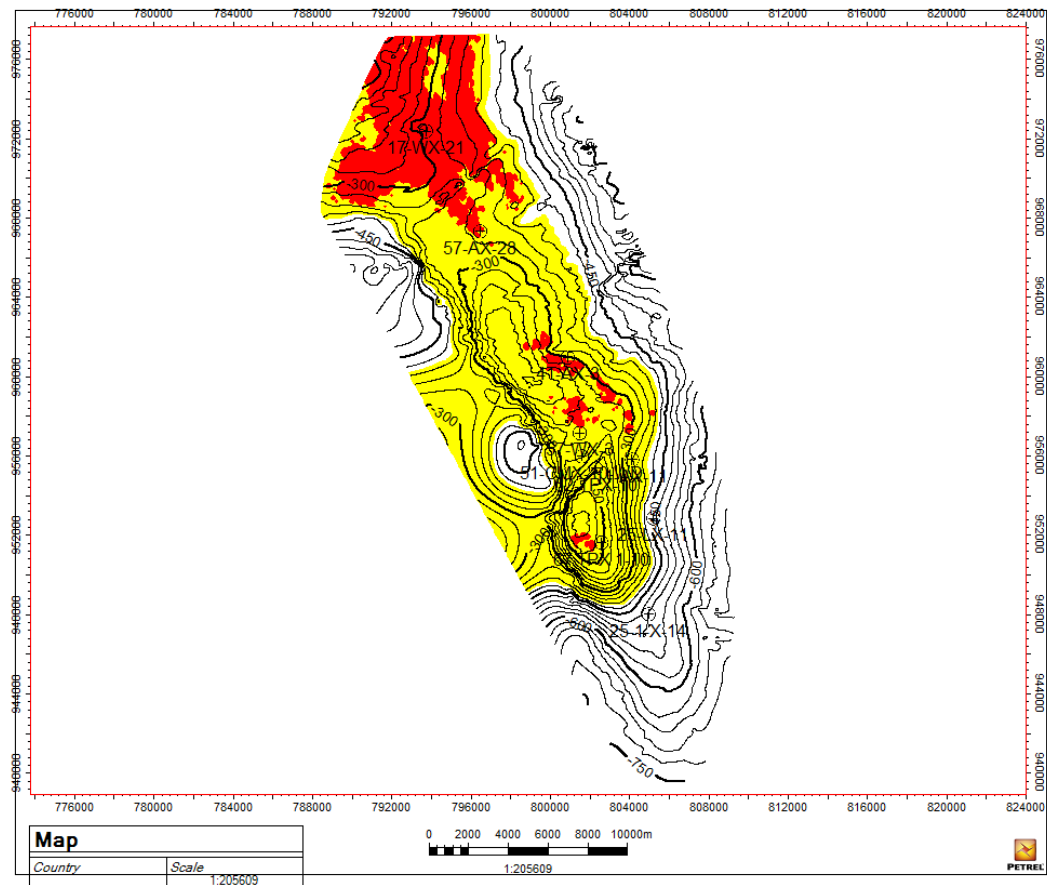


Figure 5.60: 2D map of the areas with the most optimal conditions for CO₂ injection and storage for Case 3. Low HCPV constraint, constant ductility.

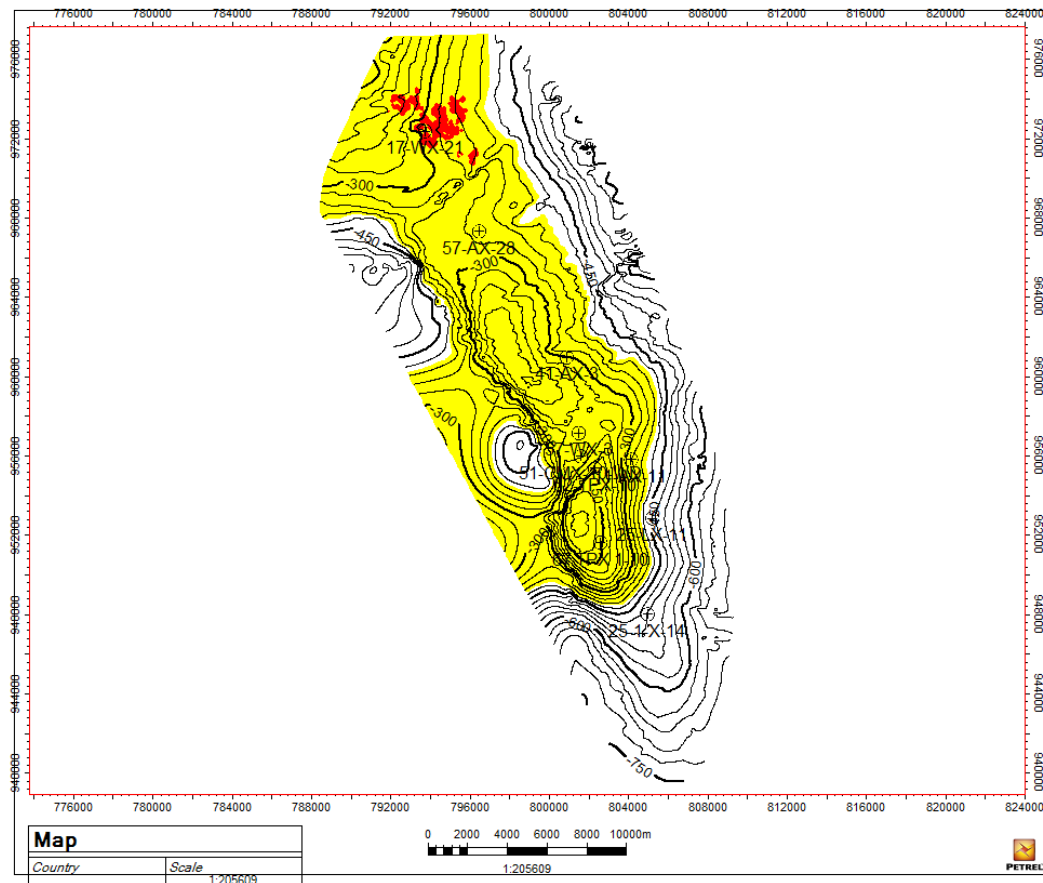


Figure 5.61: 2D map of the areas with the most optimal conditions for CO₂ injection and storage for Case 4. High ductility constraint, constant HCPV.

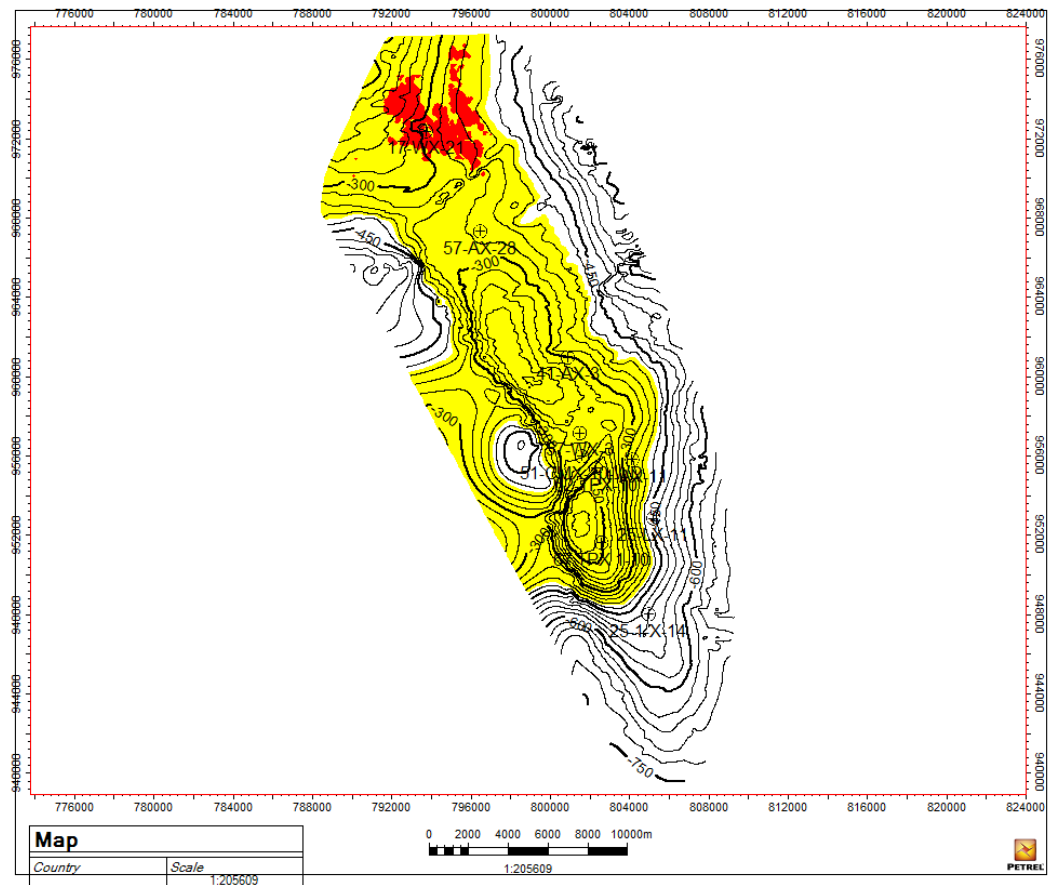


Figure 5.62: 2D map of the areas with the most optimal conditions for CO₂ injection and storage for Case 5. Medium ductility constraint, constant HCPV.

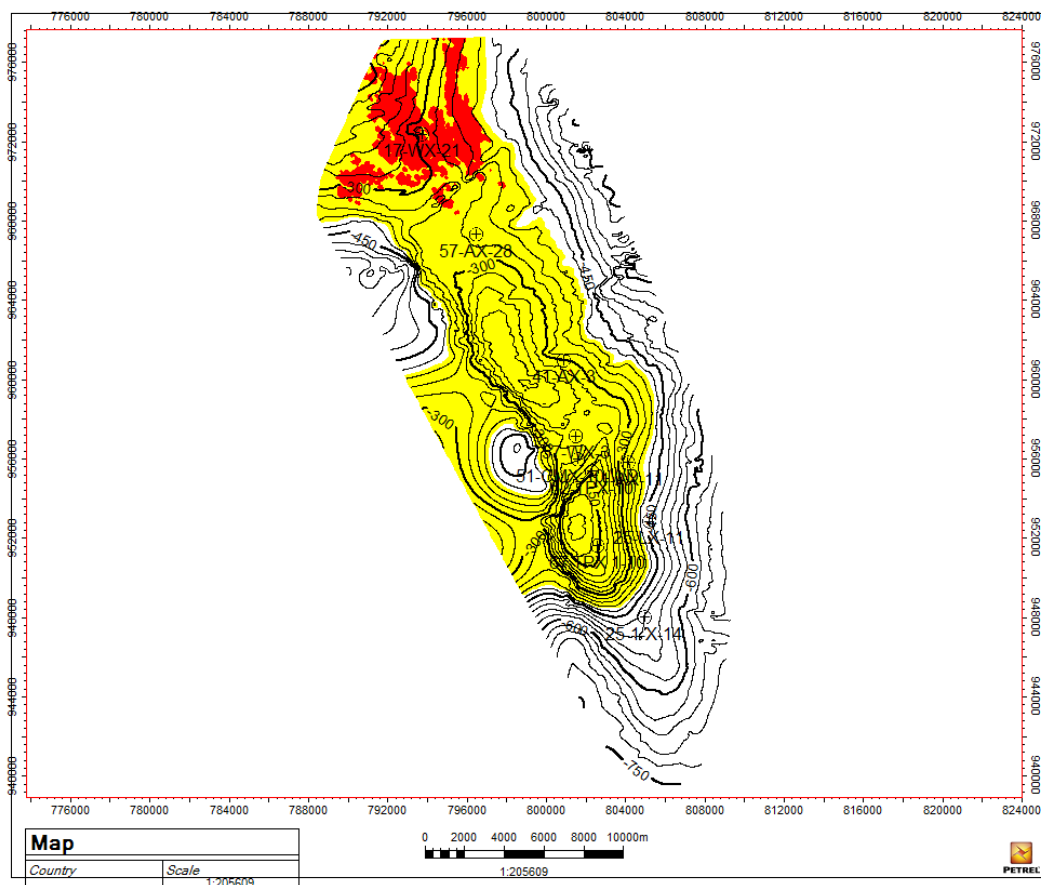


Figure 5.63: 2D map of the areas with the most optimal conditions for CO₂ injection and storage for Case 6. Low ductility constraint, constant HCPV.

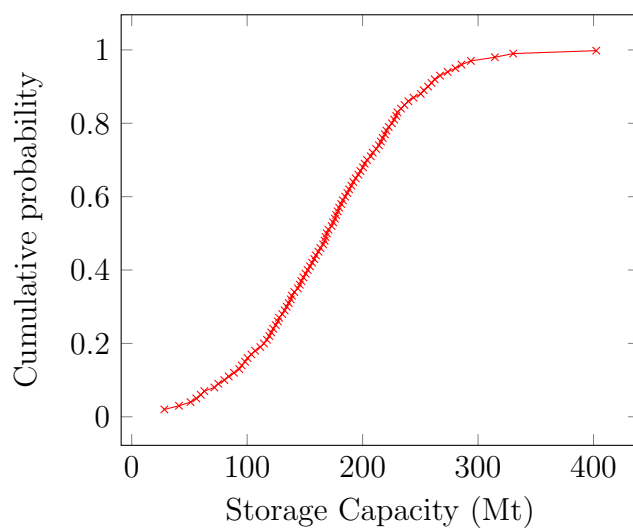


Figure 5.64: Cumulative probability plot of the storage capacity calculated with Equation 2.4 and cumulative probability with SipMath Excel Add-On.

Conclusions

Based on the performed work, the following key conclusions were drawn:

General Characteristics

1. Average thickness was recorded from the log data. Average thickness of the caprock is 93.74 m and reservoir's average thickness is 70.42 m.
2. Using the temperature gradient method, average temperatures were calculated, providing average values of 89.3 °C and 93.7 °C for the caprock and the reservoir, respectively.
3. Pressure computation was performed based on gradient method, providing average pressure of 141.32 bar for the caprock and 148.3 bar for the reservoir.

Petrophysics

1. Calculated average total porosity for all the wells in the caprock is $6.489 \pm 4.172\%$ and $9.008 \pm 6.025\%$ in the reservoir. Effective porosity in the caprock is $0.1375 \pm 0.0810\%$ and in the reservoir it is $4.923 \pm 4.310\%$.
2. Water saturation in the caprock zone is 0.5141 ± 0.2677 v/v, and in the reservoir zone 0.2146 ± 0.1231 v/v.
3. Permeability values for both zones were calculated with Coates' method, resulting values of 0.0594 mD for the caprock and 3.83 mD for the reservoir.
4. Volume of shale was calculated and the average V_{SH} in the caprock is 0.5188 v/v, while in the reservoir the value is 0.0841 v/v. The caprock was concluded to be shaly, and the reservoir - not shaly.
5. Lithology analysis from the logs was completed providing mineralogy in the caprock and reservoir. Average lithology composition for the caprock is 78% dolomite, 14% limestone, 8% anhydrite. The average composition of the reservoir is 52% limestone, 25% dolomite, 23% sandstone.

Geomechanics

1. Average pore pressure in the all the wells for the reservoir is 2515.947 ± 28.773 psi.
2. Fracture gradient calculation for the caprock was performed, providing an average value for all the wells of 3444.161 ± 62.011 psi.
3. Average shear modulus value was calculated to be 3.473 ± 0.683 Mpsi in the caprock area.
4. Young's modulus calculation provided an average value for all wells of 8.699 ± 1.668 Mpsi in the caprock area.
5. Calculated average Poisson's ratio value is 0.253 ± 0.013 in the caprock area.
6. Average bulk modulus in the caprock was calculated to be 5.872 ± 1.038 Mpsi.
7. Unconfined compressive strength (UCS) for the caprock was calculated and the average value is 168.745 MPa.
8. Tensile strength calculation in Techlog[©] yielded an average value of 15.87 MPa.
9. Brittleness-ductility analysis was performed in Techlog[©], depicting that the majority of data (Well 67-TPX 1-10) was in the ductile region (Figure 5.32, leading to our conclusion that the caprock is predominantly ductile, has good integrity and can be used to inject and store CO₂).

Petrel[©] Modelling

1. 3D model of the Tensleep formation with the overlying Goose Egg caprock was carried out and 3D models for the caprock and reservoir areas were populated by the following properties: pore pressure (caprock); permeability (caprock and reservoir); porosity (caprock and reservoir); volume of shale (caprock and reservoir); water saturation (caprock and reservoir); fracture gradient (caprock); vertical stress (caprock, with an average value of 5700 psi); maximum and minimum horizontal stresses (caprock, with average values of 4650 psi and 2600 psi, respectively); Poisson's ratio (caprock); shear modulus (caprock); Young's modulus (caprock).
2. Volume calculation was performed based on the OWC that was found in the literature, providing the following results: bulk volume 6.378×10^9 m³; net volume 6.629×10^9 m³; pore volume 5.12×10^8 sm³; HCPV 2.417×10^9 RB; STOIP 2.197×10^9 STB.
3. 2D area maps of volume and ductility were made, providing constraints for well selection maps (constraints can be seen in Table 5.10).

4. Six 2D maps to illustrate the six constrained cases were obtained, to locate the optimal area for CO₂ injection. Based on these, well 17-WX-21 was concluded to be the most suitable well for the injection.
5. Storage capacity calculation for the Tensleep reservoir was done, resulting in the CO₂ capacity P50 value of 168.7 Mt.

Future work

As mentioned in Chapter 1.1, the time was not in abundance during the thesis. Due to that, the following future work possibilities can be presented:

1. reservoir simulation in the mentioned areas by means of a commercial simulator like Eclipse[®]. By implementing all of the collected data from Petrel[®] as an input, simulation can be performed, which will provide knowledge about the mechanics, magnitude and speed of the CO₂ spreading;
2. modelling of solubility, alteration of pH, CO₂ plume migration within the reservoir should also be carried out;
3. determine flow types and injectivity rates for the most optimal wells;
4. rerun the Petrel[®] simulation by implementing the corrected seismic data (which was not available during our thesis);
5. perform stochastic analysis, assessing the sensitivity of the obtained properties;
6. analyse other methods for CO₂ mitigation, for instance: CO₂ conversion (electrochemical and catalytic) and utilisation, Biochar etc.;
7. perform an economic analysis of CO₂ injection into Tensleep reservoir, providing estimates of the cost of injection. This would allow to examine the feasibility of the process and ultimately, choose the best injection strategy.

Bibliography

- [1] M. A. Addis. “The Geology of Geomechanics: Petroleum Geomechanical Engineering in Field Development Planning”. In: *Geomechanics and Geology*. Ed. by J.P. Turner et al. London: Geology Society, 2017, pp. 13–35.
- [2] International Energy Agency. “CO2 Emissions From Fuel Combustion: Overview (2017 Edition)”. In: *IEA* (2017).
- [3] K. Akaku. “Numerical Simulation of CO2 Storage in Aquifers without Trapping”. In: *International Petroleum Technology Conference* (2008).
- [4] A. Al-Hashami et al. “CO2 Injection for Enhanced Gas Recovery and Geo-Storage: Reservoir Simulation and Economics”. In: *Society of Petroleum Engineers* (2005).
- [5] Andy Chadwick et al. “Best Practice for the Storage of CO2 in Saline Aquifers. Observations and Guidelines from the SACS and CO2STORE Projects”. In: *British Geological Survey* (2008).
- [6] Bert Bock et al. *Economic Evaluation of CO2 Storage and Sink Enhancement Options*. TVA Public Power Institute, 2003.
- [7] Hao Xu et al. “Characterization of Rock Mechanical Properties Using Lab Tests and Numerical Interpretation Model of Well Logs”. In: *Mathematical Problems in Engineering* (2015).
- [8] J. D. Schuppers et al. “Storage Capacity and Quality of Hydrocarbon Structures in the North Sea and Aegean Region. Final Report of FP5 GESTCO Project. TNO Report. NITG 02-020-B.” In: *CGS Europe* (2003).
- [9] Pengzhi Pan et al. “Geochemical Modeling of CO2 Geological Storage: A Review”. In: *Journal of Rock Mechanics and Geotechnical Engineering* 8 (2016).
- [10] S. Khan et al. “An Integrated Geomechanics Workflow for Caprock-Integrity Analysis of a Potential Carbon Storage”. In: *SPE International* (2010).
- [11] Stefan Bachu et al. “CO2 storage capacity estimation: Methodology and gaps”. In: *International Journal of Greenhouse Gas Control* 42 (2007).
- [12] Z. Duan et al. “An equation of state for the CH4–CO2–H2O system: I. Pure systems for 0 to 1000 C and 0 to 8000 bar”. In: *Geochim. Cosmochim. Acta* 56. (1992).
- [13] Michael Allaby. *A Dictionary of Geology and Earth Sciences (4th Edition)*. Oxford University Press, 2013.
- [14] Phillip A. Allen and John R. Allen. *Basin Analysis: Principles and Applications. 2nd Edition*. Wiley-Blackwell, 2013.

- [15] George Asquith and Daniel Krygowski. *Basic Well Log Analysis*. The American Association of Petroleum Geologists, 2003.
- [16] Bruce Averill and Patricia Eldredge. *Effects of Temperature and Pressure on Solubility*. In: *Principles of General Chemistry*. Creative Commons, 2012.
- [17] Balan B., Mohaghegh S., and Ameri S. “State-of-the-art in permeability determination From Well Log Data: Part 1 - A comparative study, model development”. In: *SPE Eastern Regional and Exhibition held in Morgantown, West Virginia, USA* (Jan. 1995).
- [18] Sally M. Benson et al. *Relative Permeability for Multi-phase Flow in CO₂ Storage Reservoirs. Part II: Resolving Fundamental Issues and Filling Data Gaps*. Stanford University, 2015.
- [19] Ed L. Bigelow. *Introduction to Wireline Log Analysis*. Baker Hughes, Inc., 2002.
- [20] Pradyut Bora. *Formation Evaluation Based On Logging Data*. Oil India Limited.
- [21] A. Busch et al. “The Significance of Caprock Sealing Integrity for CO₂ Storage”. In: *Society of Petroleum Engineers* (2010).
- [22] Laura Chiaramonte. “Geomechanical Characterization and Reservoir Simulation of a CO₂ Sequestration Project in a Mature Oil Field, Teapot Dome, WY”. PhD thesis. Stanford University, 2008.
- [23] Y. Cinar et al. “CO₂ Storage in Low Permeability Formations”. In: *SPE International* (2008).
- [24] Jacquelin Cobos and Jhony Quintal. “Caprock Integrity Study of the 2nd Wall Creek Reservoir: A case Study from Teapot Dome, Wyoming”. MA thesis. Niels Bohrs Vej 8: Aalborg University, 2017.
- [25] Kay Damen, Andre Faaij, and Wim Turkenburg. “Health, safety and environmental risks of underground CO₂ sequestration: overview of mechanisms and current knowledge”. In: *Utrecht University* (2003).
- [26] Abhijit Y. Dandekar. *Petroleum Reservoir Rock and Fluid Properties, Second Edition*. CRC Press, 2013.
- [27] D. U. Deere and R. P. Miller. “Engineering Classification and Index properties for Intact Rock.” In: *U.S. Air Force Weapons Lab, Kirtland AFB, New Mexico* (1966).
- [28] F. Delprat-Jannaud. “State-of-the-art Review of CO₂ Storage Site Selection and Characterization Methods”. In: *CGS Europe. NO D3.3*. (2013).
- [29] J. Dooley, R. Dahowski, and C. Davidson et al. “Carbon Dioxide Capture and Geologic Storage. A Core Element of a Global Energy Technology Strategy to Address Climate Change”. In: *A Technology Report. Global Energy Technology Strategy Program*. (2006).
- [30] Z.H. Duan and R. Sun. “An Improved Model Calculating CO₂ Solubility in Pure Water and Aqueous NaCl Solutions From 273 to 533 K and from 0 to 2000 bar”. In: *Chemical Geology* 193 (2003), pp. 257–271.
- [31] Ben A. Eaton. “Fracture Gradient Prediction and Its Application in Oilfield Operations”. In: *Society of Petroleum Engineers* 21 (1969).

- [32] D. Nicolas Espinoza and J. Carlos Santamarina. “CO₂ breakthrough—Caprock sealing efficiency and integrity for carbon geological storage”. In: *International Journal of Greenhouse Gas Control* 66 (2017).
- [33] Society of Exploration Geophysicists. *Pore pressure analysis*. 2016. URL: https://wiki.seg.org/wiki/Pore_pressure_analysis (visited on 04/04/2018).
- [34] M. Fleury et al. “Evaluating Sealing Efficiency of Caprocks for CO₂ Storage: an Overview of the Geocarbone-Integrity Program and Results”. In: *Oil Gas Science and Technology – Rev. IFP* 65 (2010), pp. 435–444.
- [35] Amy Fox et al. *Geomechanical Principles for Unconventional Reservoirs*. MicroSeismic, 2013.
- [36] Julio Friedmann and Vicki Stamp. “Teapot Dome: Site Characterization of a CO₂-Enhanced Oil Recovery Site in Eastern Wyoming”. In: (Jan. 2006).
- [37] Ricardo Gaviria Garcia. *Reservoir Simulation of CO₂ Sequestration and Enhanced Oil Recovery in the Tensleep Formation, Teapot Dome Field*. Texas AM University, 2005.
- [38] Nediljka Gaurina-Medimurec and Karolina Novak Mavar. “Depleted hydrocarbon reservoirs and CO₂ injection wells –CO₂ leakage assessment”. In: *The Mining-Geology-Petroleum Engineering Bulletin* 32 (2017).
- [39] Schlumberger Oilfield Glossary. *Temperature log - Schlumberger Oilfield Glossary*. URL: http://www.glossary.oilfield.slb.com/Terms/t/temperature_log.aspx (visited on 02/25/2018).
- [40] Schlumberger Oilfield Glossary. *Water saturation - Schlumberger Oilfield Glossary*. URL: http://www.glossary.oilfield.slb.com/Terms/w/water_saturation.aspx (visited on 02/27/2018).
- [41] Craig Alexander Griffith. “Physical Characteristics of Caprock Formations Used for Geological Storage of CO₂ and the Impact of Uncertainty in Fracture Properties on CO₂ Transport Through Fractured Caprocks”. PhD thesis. Carnegie Mellon University, 2012.
- [42] Megan Jo Gunther. *Estimating Brittleness Using Seismic Data in an Unconventional Shale Reservoir, Fort Worth Basin, Texas*. 2017.
- [43] S.J.T. Hangx. “Subsurface mineralisation: Rate of CO₂ mineralisation and geomechanical effects on host and seal formations. Behaviour of the CO₂-H₂O system and preliminary mineralisation model and experiments.” In: *CATO Workpackage WP 4.1 Deliverable WP 4.1-3-05* (2005).
- [44] Sam Holloway. “Carbon dioxide capture and geological storage”. In: *Phil. Trans. R. Soc.* 365 (2007), pp. 1095–1107.
- [45] Edward D. Holstein and Larry W. Lake. *Petroleum Engineering Handbook: Reservoir Engineering and Petrophysics*. Vol. 5. Elsevier Science, 2007.
- [46] S. Hurter, D. Labregere, and J. Berge. “Simulations for CO₂ Injection Projects With Compositional Simulator”. In: *SPE International* (2007).
- [47] Norman J. Hyne. *Nontechnical Guide to Petroleum Geology, Exploration, Drilling and Production. Third Edition*. PennWell Corporation, 2012.

- [48] M. Kulkarni and D. Rao. “Experimental Investigation of Various Methods of Tertiary Gas Injection,” in: *SPE SPE 90589. Petroleum Engineers Annual Technical Conference and Exhibition, Houston, TX, September 26 -29* (2004).
- [49] Axel Liebcher and Ute Münch. *Geological Storage of CO₂ – Long Term Security Aspects*. Springer, 2015.
- [50] C. Richard Liu. *Theory of Electromagnetic Well Logging*. Elsevier, 2017.
- [51] Probability Management. *Enterprise SIPmath™ Modeler Tools*. 2018. URL: <https://www.probabilitymanagement.org/tools-1/> (visited on 05/30/2018).
- [52] Luigi Marini. *Geological Sequestration of Carbon Dioxide*. Vol. 11. Elsevier Science, 2006.
- [53] Ali Al-Menhali et al. “Advanced Reservoir Characterization for CO₂ Storage”. In: *International Petroleum Technology Conference* (2014).
- [54] John W. Merck. *Introduction to Physical Geology (Lecture Notes)*. University of Maryland: Department of Geology, 2010.
- [55] Bert Metz et al. *Carbon Dioxide Capture and Storage*. Cambridge University Press, 2017.
- [56] Norman R. Morrow and Charlie Carlisle. “Low Salinity Waterflooding Fundamentals and Case Studies”. In: *2012 IOR/EOR Conference. Jackson, WY.* (2012).
- [57] Raja Mustafa N. et al. “Teapot Dome Field / Tensleep Formation”. MA thesis. Petroleum Engineering Senior Design Final Reports. University of Wyoming, 2016.
- [58] Phillip H. Nelson. “Permeability-porosity Relationships In Sedimentary Rocks”. In: *The Log Analyst* 35 (1994).
- [59] Anita Onohuome Okojie-Ayoro. *An Approach to Mapping of Shallow Petroleum Reservoirs Using Integrated Conventional 3D and Shallow P- and SH-Wave Seismic Reflection Methods at Teapot Dome Field in Casper, Wyoming*. Brigham Young University, 2007.
- [60] A. Ouenes et al. “Integrated Characterization and Simulation of the Fractured Tensleep Reservoir at Teapot Dome for CO₂ Injection Design”. In: *SPE International. Conference Paper* (2010).
- [61] Mervyn S. Paterson and Teng-fong Wong. *Experimental Rock Deformation - The Brittle Field*. Springer-Verlag Berlin Heidelberg, 2005.
- [62] Roderick Perez. “Brittleness Estimation from Seismic Measurements in Unconventional Reservoirs: Application to the Barnett Shale”. In: *Oklahoma : University of Oklahoma* (2013).
- [63] Roderick Perez. “Seismic Brittleness Index Volume Estimation from Well Logs in Unconventional Reservoirs”. In: *AAPG* 35 (2014).
- [64] SPE PetroWiki. *Temperature logging*. 2015. URL: http://petrowiki.org/Temperature_logging (visited on 02/25/2018).
- [65] IEA Greenhouse Gas RD Programme. *Caprock Systems for CO₂ Geological Storage*. 2011.

- [66] John C. Lorenz Scott P. Cooper and Laurel B. Goodwin. *Lithologic and Structural Controls on Natural Fracture Characteristics Teapot Dome, Wyoming*. Sandia National Laboratories, 2016.
- [67] P. N. Seevam, J. M. Race, and M. J. Downie. “Infrastructure and pipeline technology for carbon dioxide (CO₂) transport”. In: *Developments and Innovation in Carbon Dioxide (CO₂) Capture and Storage Technology*. Ed. by M. Mercedes Maroto-Valer. Abington Hall, Cambridge: Woodhead Publishing, 2010, pp. 408–434.
- [68] Małgorzata Słota-Valim. “Static and dynamic elastic properties, the cause of the difference and conversion methods – case study”. In: *NAFTA-GAZ* 11 (2015).
- [69] R. Span and W. Wagner. “A New Equation of State for Carbon Dioxide Covering the Fluid Region from the Triple-Point Temperature to 1100 K at Pressures up to 800 MPa”. In: *Journal of Physical and Chemical Reference Data* 25 (1996).
- [70] Luc Steel et al. “CO₂ Solubility Measurements in Brine Under Reservoir Conditions”. In: *Greenhouse Gases: Science and Technology* 6(2) (2016).
- [71] Ahmed Tarek. *Reservoir Engineering Handbook*. 4th ed. Elsevier, 2010.
- [72] David A.N. Ussiri and Rattan Lal. *Carbon Sequestration for Climate Change Mitigation and Adaptation*. Springer, 2017.
- [73] Ernesto Valbuena, Maria Barrufet, and Gioia Falcone. “Analytical Estimation of CO₂ Storage Capacity in Depleted Oil and Gas Reservoirs Based on Thermodynamic State Functions”. In: *SPE Latin American and Caribbean Petroleum Engineering Conference held in Mexito City, Mexico. 16-18 April. Society of Petroleum Engineers* (2012).
- [74] Franesca Verga. “What’s Conventional and What’s Special in a Reservoir Study for Underground Gas Storage”. In: *Energies* 11(5) (2018).
- [75] V. Vishal and T.N. Singh. *Geologic Carbon Sequestration: Understanding Reservoir Behaviour*. Springer, 2016.
- [76] S.P. White et al. “Natural CO₂ Reservoirs on the Colorado Plateau and Southern Rocky Mountains, USA, A Numerical Model”. In: *Greenhouse Gas Control Technologies - 6th International Conference* 1 (2003), pp. 423–248.
- [77] Wei Yan and E.H Stenby. “The Influence of CO₂ Solubility in Brine on Simulation of CO₂ Injection into Water Flooded Reservoir and CO₂ WAG”. In: *SPE International* (2010).
- [78] Peigui Yin. *Characterization of Tensleep Sandstone reservoirs: Rocky Mountain Section AAPG Annual Meeting Abstracts and Program, Search and Discovery article*. PennWell Corporation, 2005.
- [79] “Challenges Associated with CO₂ Sequestration and Hydrocarbon Recovery”. In: *Recent Advances in Carbon Capture and Storage*. Ed. by Yongseung Yun. Intech, 2017. Chap. 10, pp. 210–233.
- [80] Yongseung Yun. *Recent Advances in Carbon Capture and Storage*. InTech, 2017.

- [81] Nummedal D. Zhang Q. and Yin P. *Stratigraphy, Sedimentology and Petrophysics of the Tensleep Sandstone at Teapot Dome and in Outcrop*. University of Wyoming, 2005.

Wireline Logs

A.1 Gamma Ray Log

Gamma ray (GR) logs measure the natural radioactiveness in formations. The response of the gamma ray log is dependant on the content of the shale in the formation. If there is more shale, then the log will give a higher GR log reading and vice versa. It has to be noted however that a formation without shale can also produce a high GR log reading if there is glauconite, potassium feldspar or uranium-rich water present in the formation. GR logs are important, because they provide the means to calculate water saturation in shale-bearing formations. GR is usually depicted on a left track of the log display with the caliper curve [15].

Main uses of the GR logs :

- to identify the lithology;
- to determine volume of shale and clay;
- to correlate various zones.

A.2 Neutron Porosity Log

Neutron porosity logs (in combination with other logs) are used for two main reasons:

- to calculate the porosity;
- to recognize the gas present in the formation;

In case if the formation lithology is known and the pores are full of liquid, the porosity can be directly used to calculate the porosity. On the other hand, if the lithology is not known and there is a presence of gas in the formation, then the

neutron logs are used in combination with other logs to determine the required parameters. Neutron porosity logs use either a pulse-activated accelerator or a chemical source to get a response based on the hydrogen amount in the formation. [19]

A.3 Depth log

Depth logging is the most fundamental measurement, providing extensive and precise information on the depth of the borehole. Furthermore, it provides a basis for most other logging tools for obtaining depth related data, as knowing precisely at what depth a certain measurement is occurring is vital for a good characterization of the well.

Used standards are specified as a function of:

- well depth;
- wireline cable size;
- mud weight;

The base log is expected to be within the range of 1ft to 10000 ft of measured depth. The accuracy of this procedure relies on calibration and verification. Depth calibration is based on known and measurable properties such as cable strength while the verification procedure ensures that compensations like the variations of cable length as a function of tension are considered. Some operating conditions in the downhole must be known prior to selecting the cable to ensure a precise depth measurement (chemical composition, temperature etc). To keep track of the depth, magnetic clips are attached to the cable. Besides that, time markers are used as well to indicate the logging speed, which is usually in intervals of 60 seconds. [19]

A.4 Caliper log

Caliper log is a well log tool that provides information about the diameter of well along its depth. It is important to know the changes in borehole diameters across its depth since most boreholes are usually irregular. Caliper data is mainly used to determine the volume of the wellbore.

Caliper log uses sonic devices that usually records diameters at several depths simultaneously and are referred to as „multifinger” calipers. More advanced sonic equipment can provide a full 360-degree acoustic image of the borehole size and shape. [19]

Main uses of the caliper logs [47]:

- Determine the size of the hole (needed for engineering calculations);
- Various logs (so-called compensated logs) have to be calibrated for the well-bore size size;
- Locate thick filter cakes and permeable zones.

A.5 Acoustic (sonic) logs

According to Liu [50], the average speed of sound in oil and water is around 1310 - 1615 m/s, but in rocks around 1828 m/s for shales and 8077 m/s for dolomites. So, sonic logs provide a great way to characterize the lithology and porosity. This velocity is obtained when the travelling time through formation (knowing a constant distance that the wave travels through) is recorded.

As can be seen on figure A.1, the transmitter T1 will emit a sonic pulse that will go through mud and into the formation, where it will move in all directions. Small part of the sonic pulse can, however, "reflect" back, go through mud again and reach the receiver. Important parameter in sonic logs is the Δt , which depicts the time difference between the pulse arriving at two different receivers. This is the basis for the sonic log measurement.

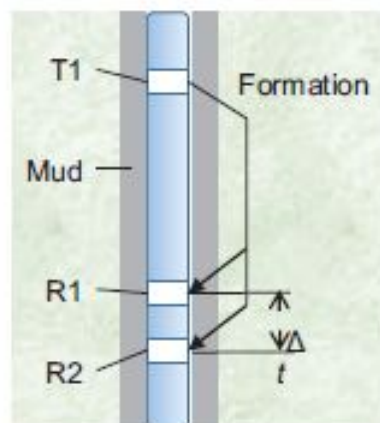


Figure A.1: Principle of a sonic log. Source: [50]

A.5.1 Compressional slowness log

DT (compressional slowness) logs depict the capacity to transmit the acoustic waves through the formation. This is strongly dependent on the lithology and porosity of the formation.

Main uses of the DT log are:

- Determine the porosity;

- Determine the lithology;
- Identify over-pressure;
- Identify fractures;
- Correlate various wells.

A.6 Resistivity log

Electrical logging is one of the oldest logging tools that was invented by the Schlumberger brothers in 1927 [50]. By the resistivity of the formation we talk about the electric current that the materials in the formation can withstand. Gas, oil and dry rock are good insulators and they do not conduct current that well. On the other hand, water is a good conductor. Based on this difference in the resistivities, it is possible to determine the fluids present in the reservoir. According to Hyne [47], oil and gas cannot be seen separately on a resistivity log if there is no change in porosity. If the porosity and the water resistivity is known, oil saturation can be calculated.

Main uses of the resistivity logs:

- Determine the fluids present in the reservoir;
- Correlate the formations;
- Determine the water saturation.

A.7 Formation temperature log

This type of log records the temperature gradient in the well. By comparing the recorded data to a reference gradient, anomalies can be found. This allows the to identify:

- zones of production or taking of fluids;
- cement or hydraulic fracture treatment evaluation
- location of circulation loss zones;
- casing leaks;

Temperature logs are recorded either using an analog measuring method or a digital one. For both types, spikes per minute are counted and translated into a temperature change across depth. A recording sensitivity of 1 oF/in is strongly recommended for both methods.

The temperature tool it self is most effective when located at the bottom of the tool string, so that the recordings would be made in a downward direction in the undisturbed fluid. To achieve precise recordings, it is recommended to keep a constant logging speed and not to exceed 30 ft/min. [39, 64]

A.8 Formation density log (FDL)

FDL logs work on the principle that there exists a radioactive source that will bombard the rock with gamma rays. Then it is possible to see a difference in scattering, which will depend on the atom sizes of a particular rock. If the rock is not dense and has a low porosity, then more gamma rays will be absorbed instead of scattered back to the detector of the logging tool. Porous rock however will scatter the gamma rays [47] Figure A.2 shows a typical FDL log that is used in oil and gas industry.

Most important tasks that can be carried out with the help of a FDL log are:

- identify lithology ;
- calculate porosity.

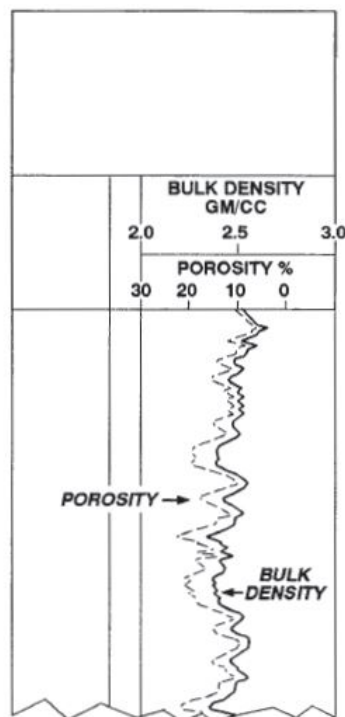


Figure A.2: Formation density log. Source: [47]

Additional Data From Techlog[©]

Figures presented in this part of the Appendix consist of following subsections: porosity, water saturation, volume of the shale and ... that were obtained from Techlog and not used in the main part of the report.

B.1 Porosity

Figures B.1-B.6 show the porosity histograms and logs for Permian and Pennsylvanian layers.

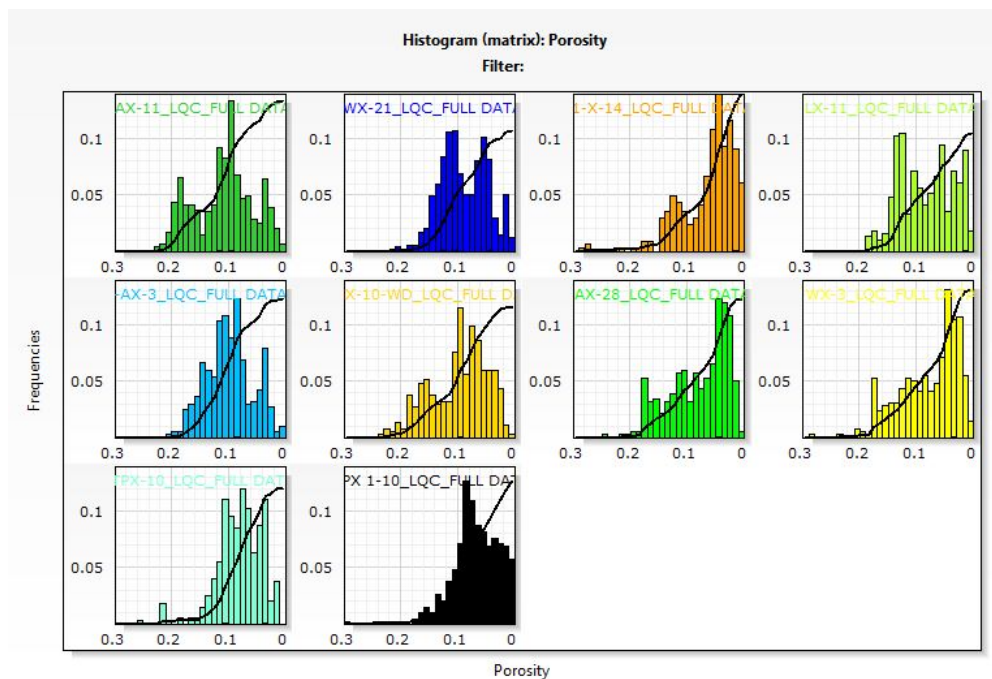


Figure B.1: Depiction of total porosity values for each individual well in the reservoir (Pennsylvanian layer).

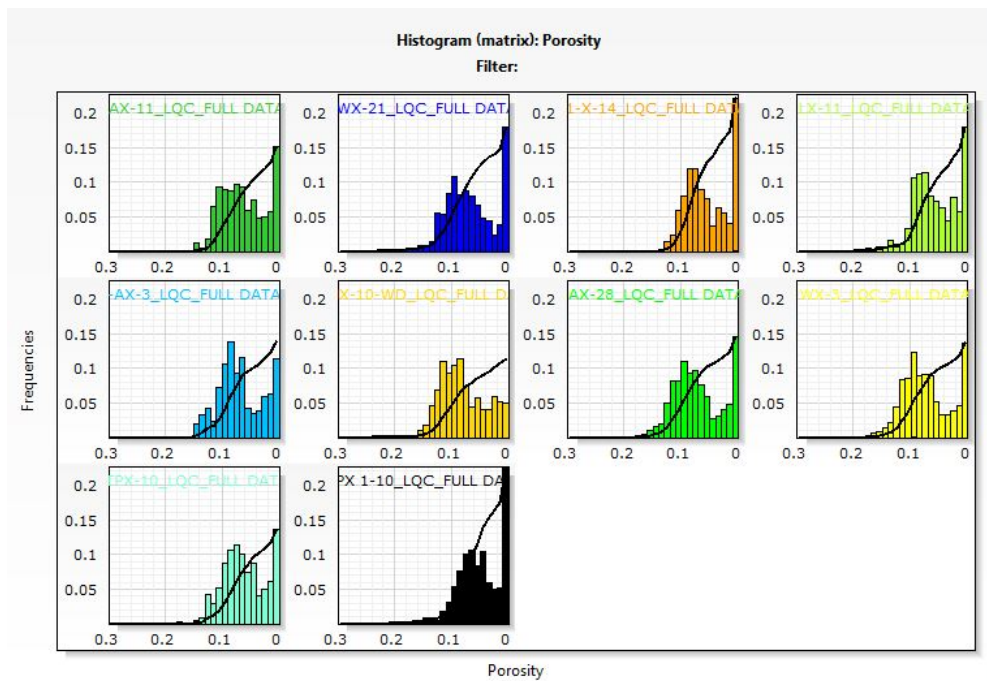


Figure B.2: Depiction of total porosity values for each individual well in the caprock (Permian layer).

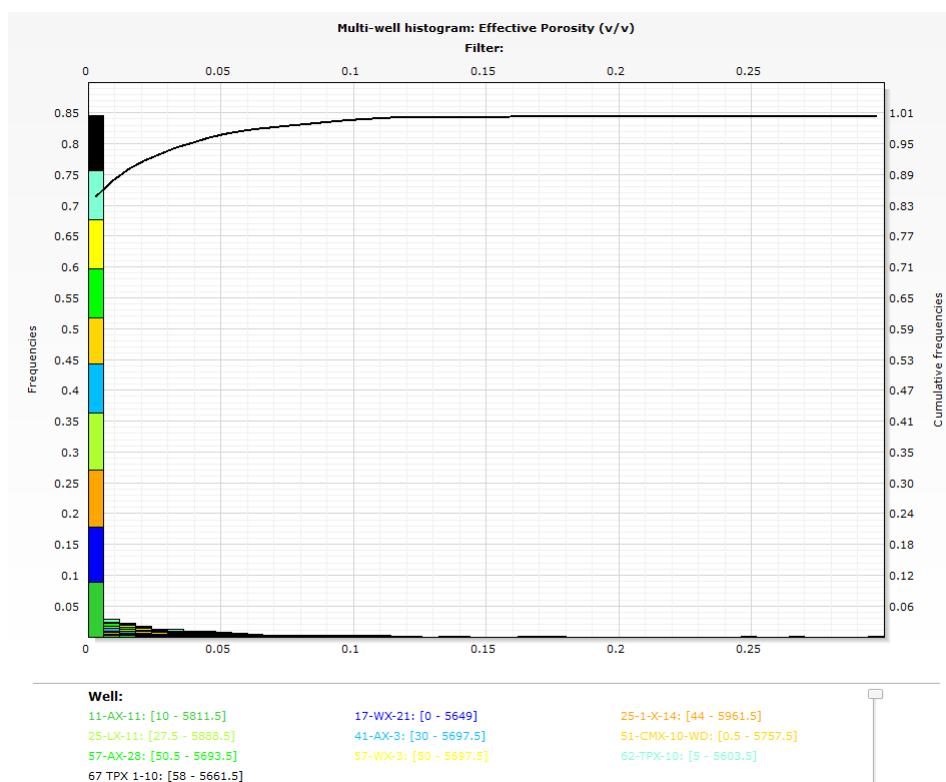


Figure B.3: Depiction of cumulative effective porosity values for all 10 wells in the caprock (Permian layer).

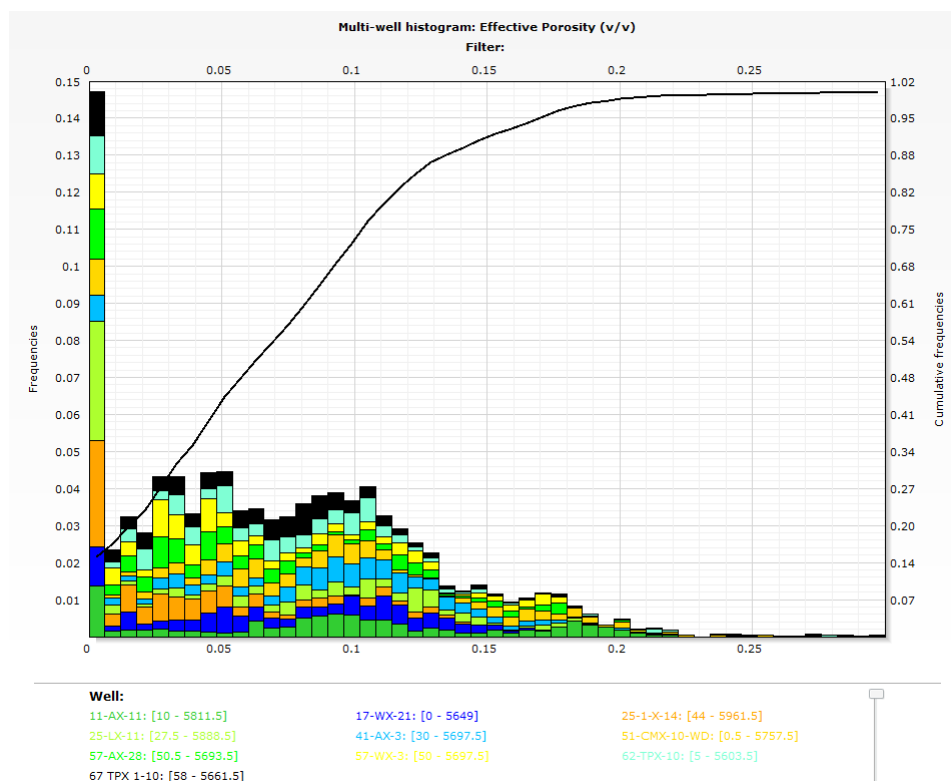


Figure B.4: Depiction of cumulative effective porosity values for all 10 wells in the reservoir (Pennsylvanian layer).

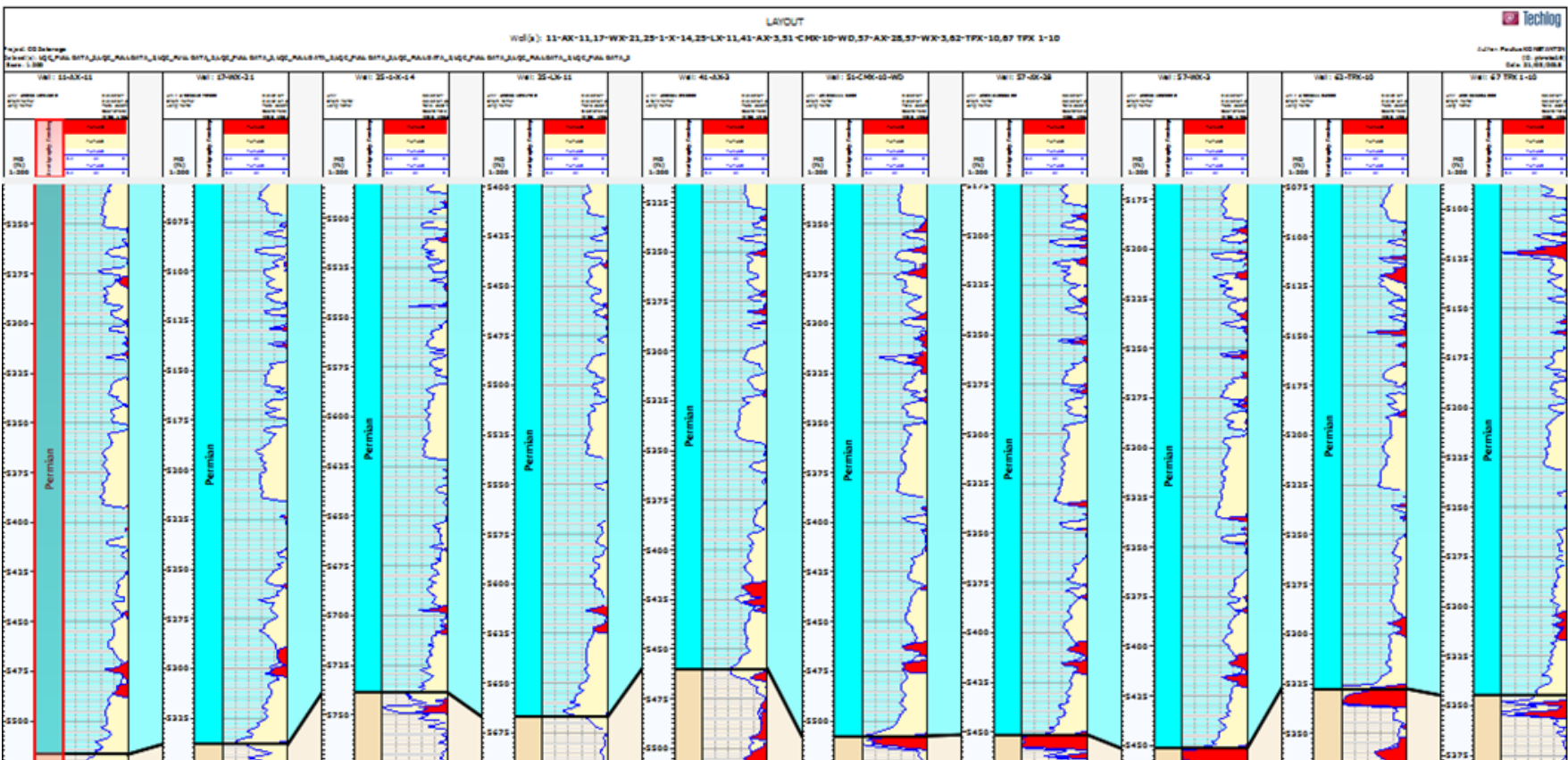


Figure B.5: Logs for all 10 wells showing the effective and total porosity in the caprock (Permian layer). Logs from left: 11-AX-11, 17-WX-21, 25-1-X-14, 25-LX-11, 41-AX-3, 51-CMX-10-WD, 57-AX-28, 57-WX-3, 62-TPX-10, 67-TPX 1-10.

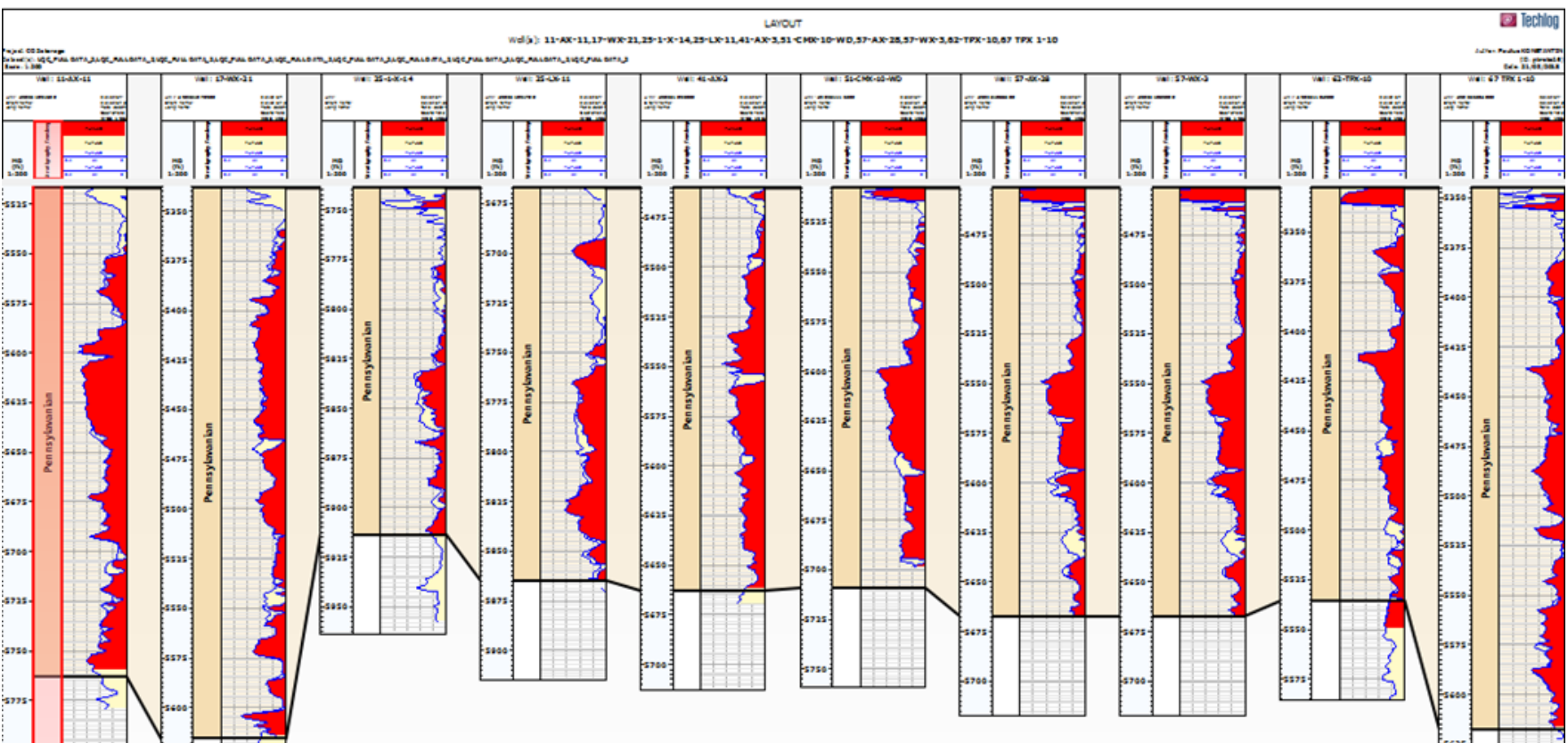


Figure B.6: Logs for all 10 wells showing the effective and total porosity in the reservoir (Pennsylvanian layer). Logs from left: 11-AX-11, 17-WX-21, 25-1-X-14, 25-LX-11, 41-AX-3, 51-CMX-10-WD, 57-AX-28, 57-WX-3, 62-TPX-10, 67-TPX 1-10.

B.2 Water Saturation

Figures B.7-B.13 show the water saturation histograms, box plots and logs for Permian and Pennsylvanian layers. Figure B.11 shows the cross-plot of water saturation and porosity for the reservoir, where it can be seen that most of the values are observed at porosity value of 0.09 and water saturation of 0.15.

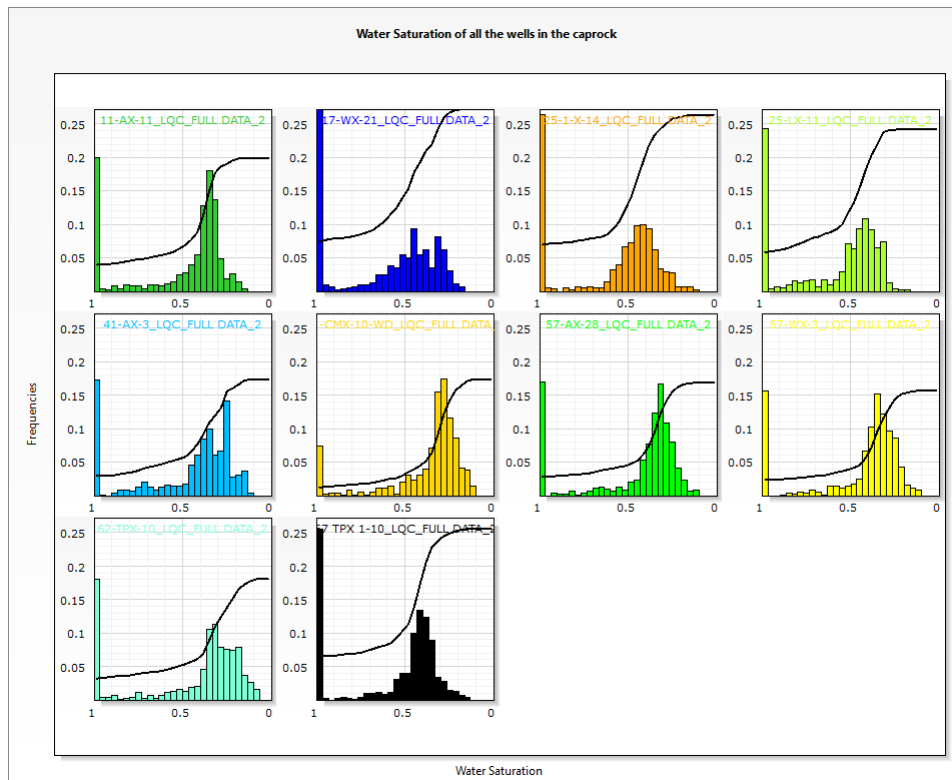


Figure B.7: Depiction of water saturation values for each individual well in the caprock (Permian layer).

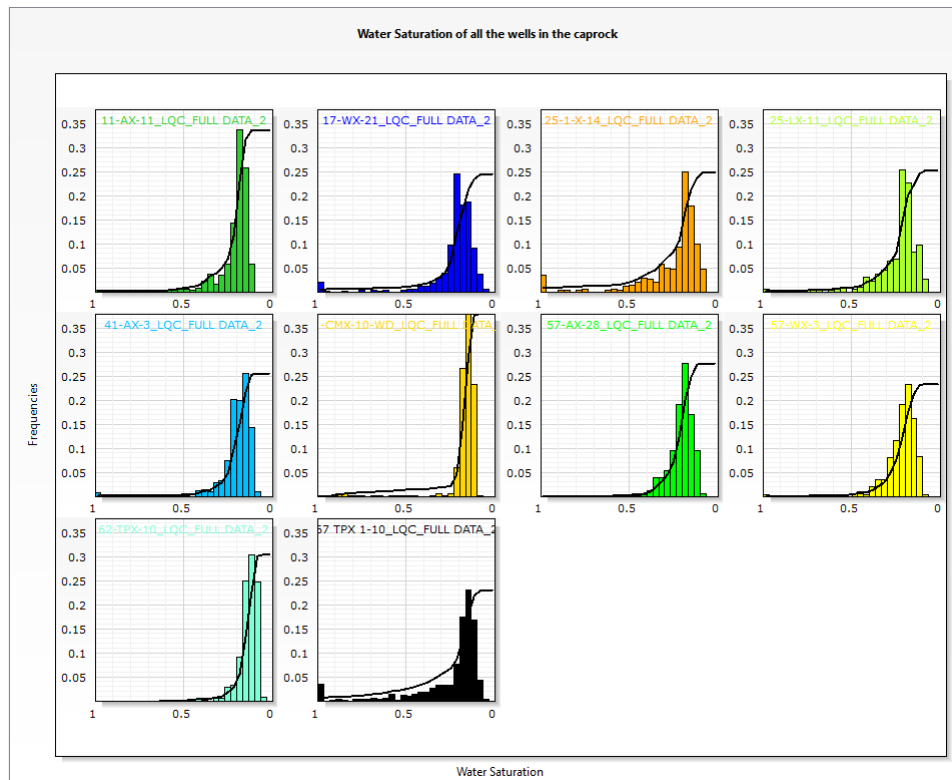


Figure B.8: Depiction of water saturation values for each individual well in the reservoir (Pennsylvanian layer).

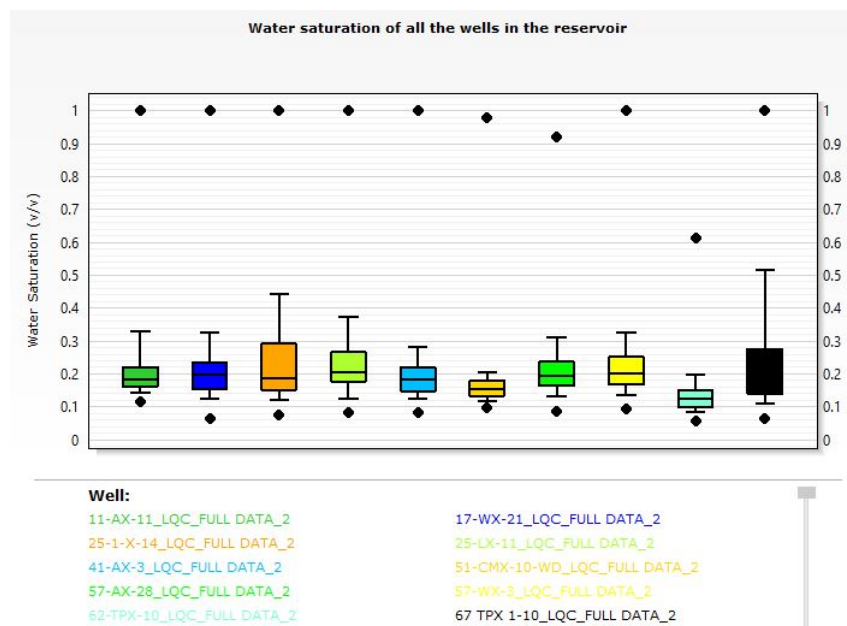


Figure B.9: Depiction of the average water saturation of each individual well in the reservoir (Pennsylvanian layer).

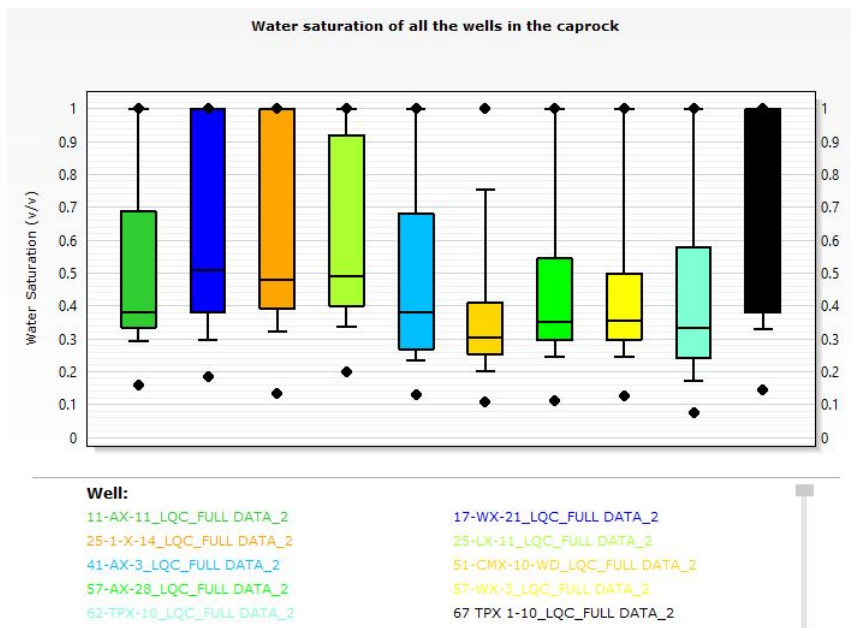


Figure B.10: Depiction of the average water saturation of each individual well in the caprock (Permian layer).

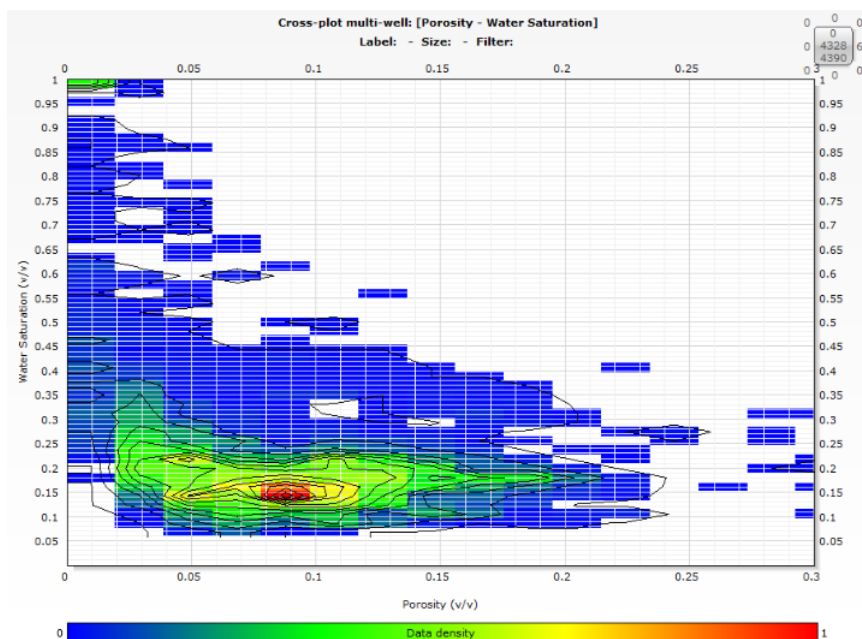


Figure B.11: Depiction of the cross-plot for water saturation and porosity for the reservoir zone across all the wells with data density legend.

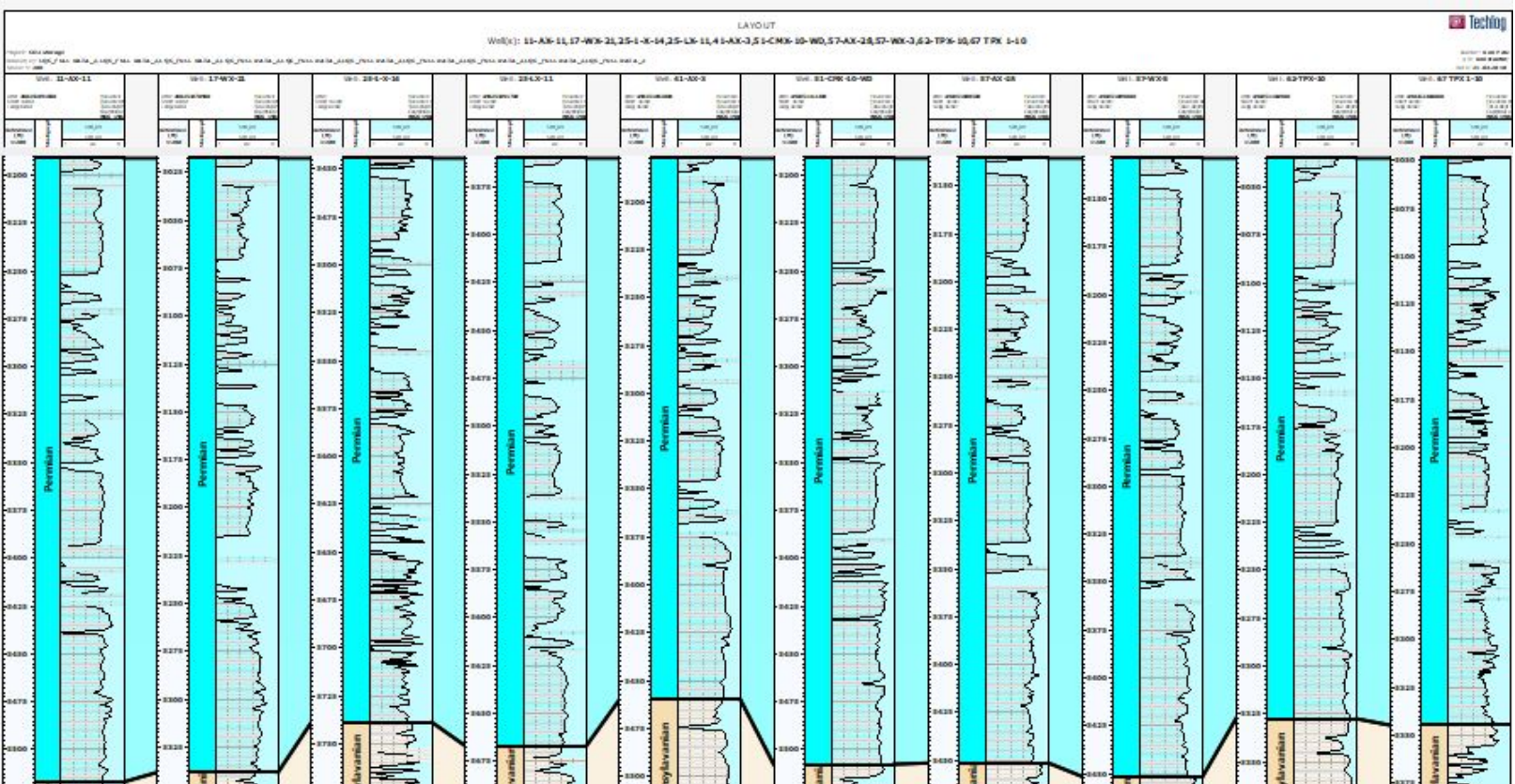


Figure B.12: Logs for all 10 wells showing water saturation in the caprock (Permian layer). Logs from left: 11-AX-11, 17-WX-21, 25-1-X-14, 25-LX-11, 41-AX-3, 51-CMX-10-WD, 57-AX-28, 57-WX-3, 62-TPX-10, 67-TPX 1-10.

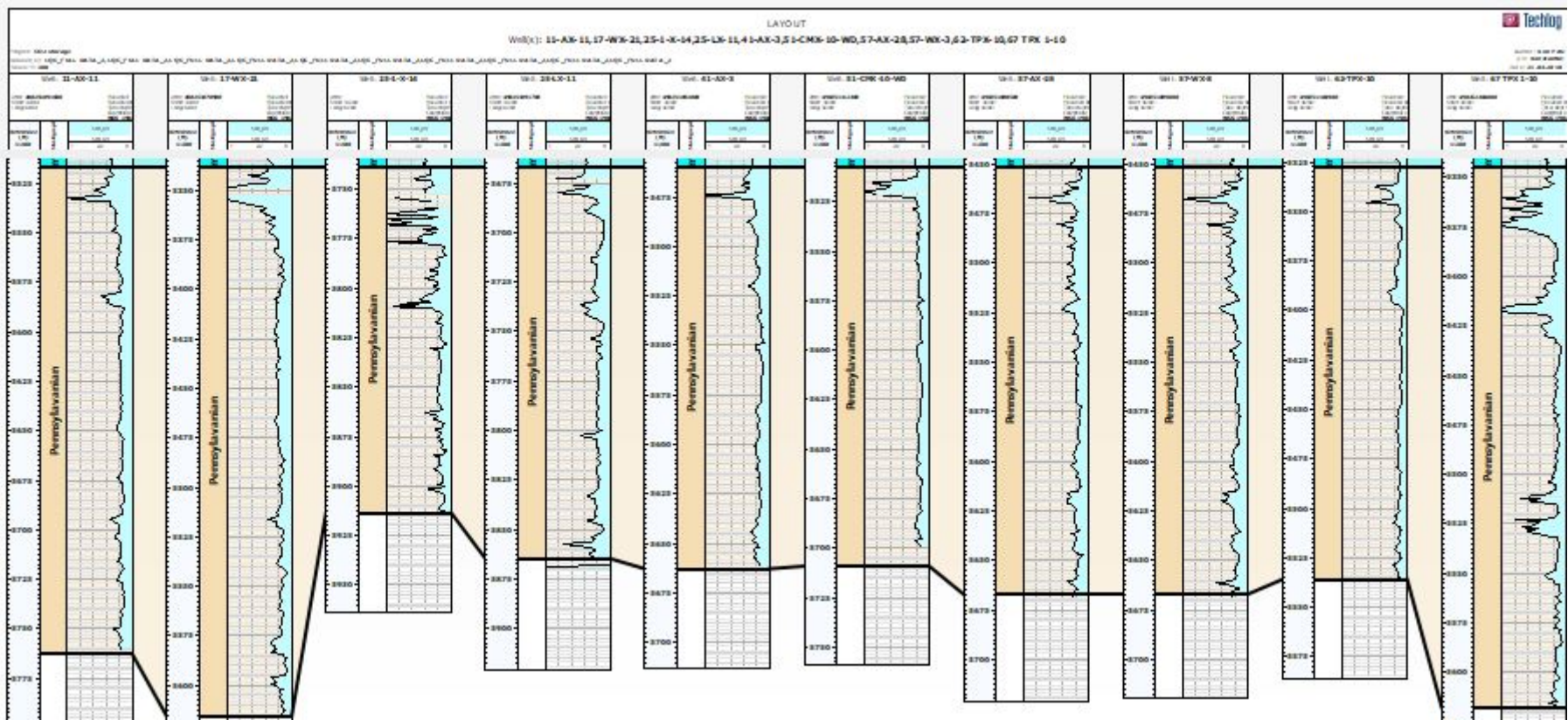


Figure B.13: Logs for all 10 wells showing water saturation in the reservoir (Pennsylvanian layer). Logs from left: 11-AX-11, 17-WX-21, 25-1-X-14, 25-LX-11, 41-AX-3, 51-CMX-10-WD, 57-AX-28, 57-WX-3, 62-TPX-10, 67-TPX 1-10.

B.3 Volume of Shale and Mineralogy

Figures B.14-B.16 show the volume of the shale histograms and logs for Permian and Pennsylvanian layers. Figure B.17 shows the mineral composition of the 10 wells in Permian and Pennsylvanian layers.

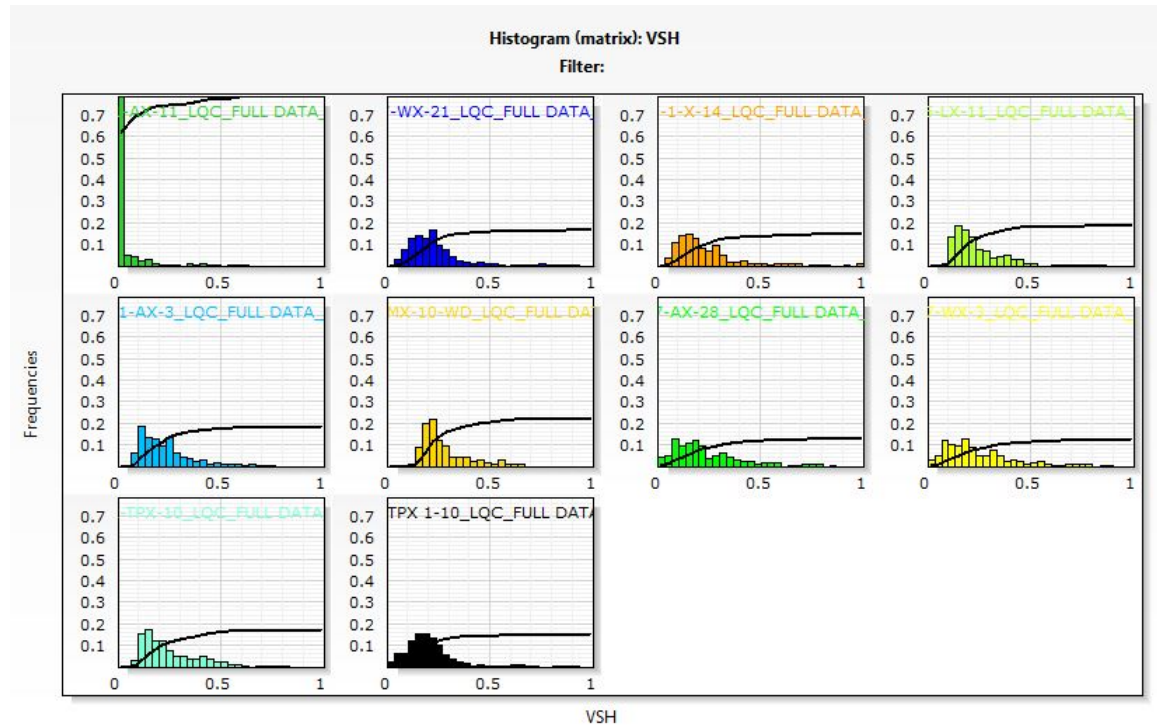


Figure B.14: Matrix histograms showcasing the volume of shale in each of the 10 wells in the reservoir (Pennsylvanian layer).

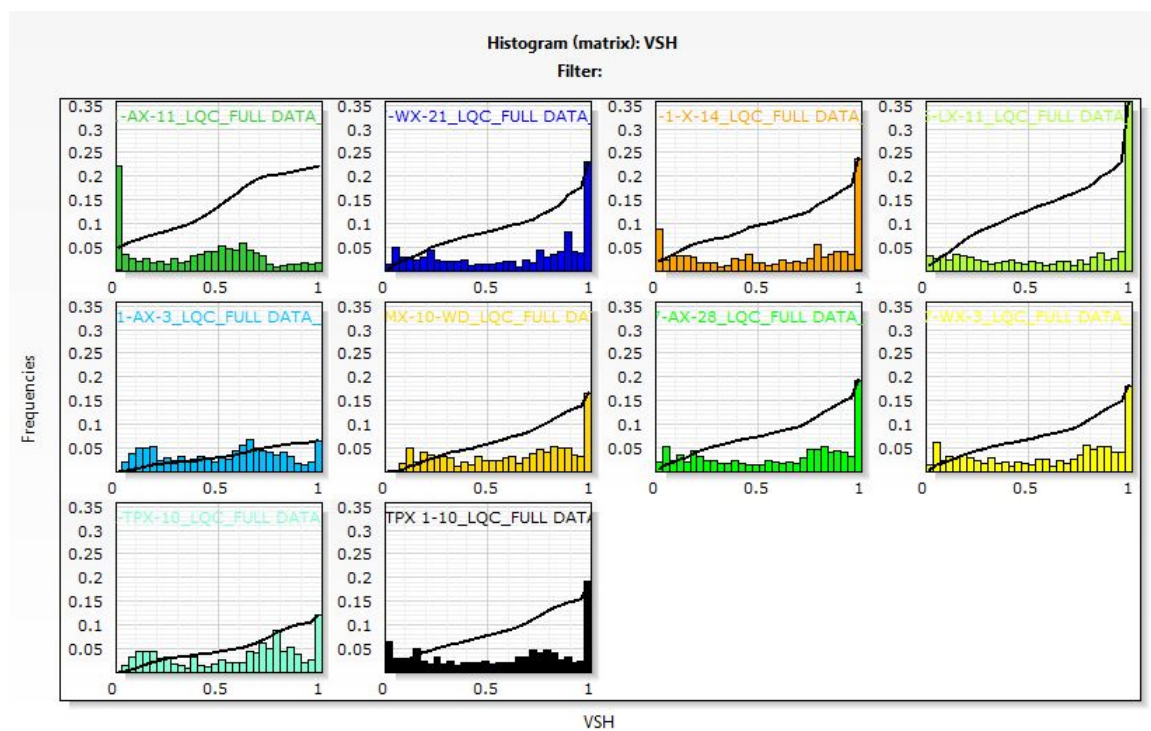


Figure B.15: Matrix histograms showcasing the volume of shale in each of the 10 wells in the caprock (Permian layer).

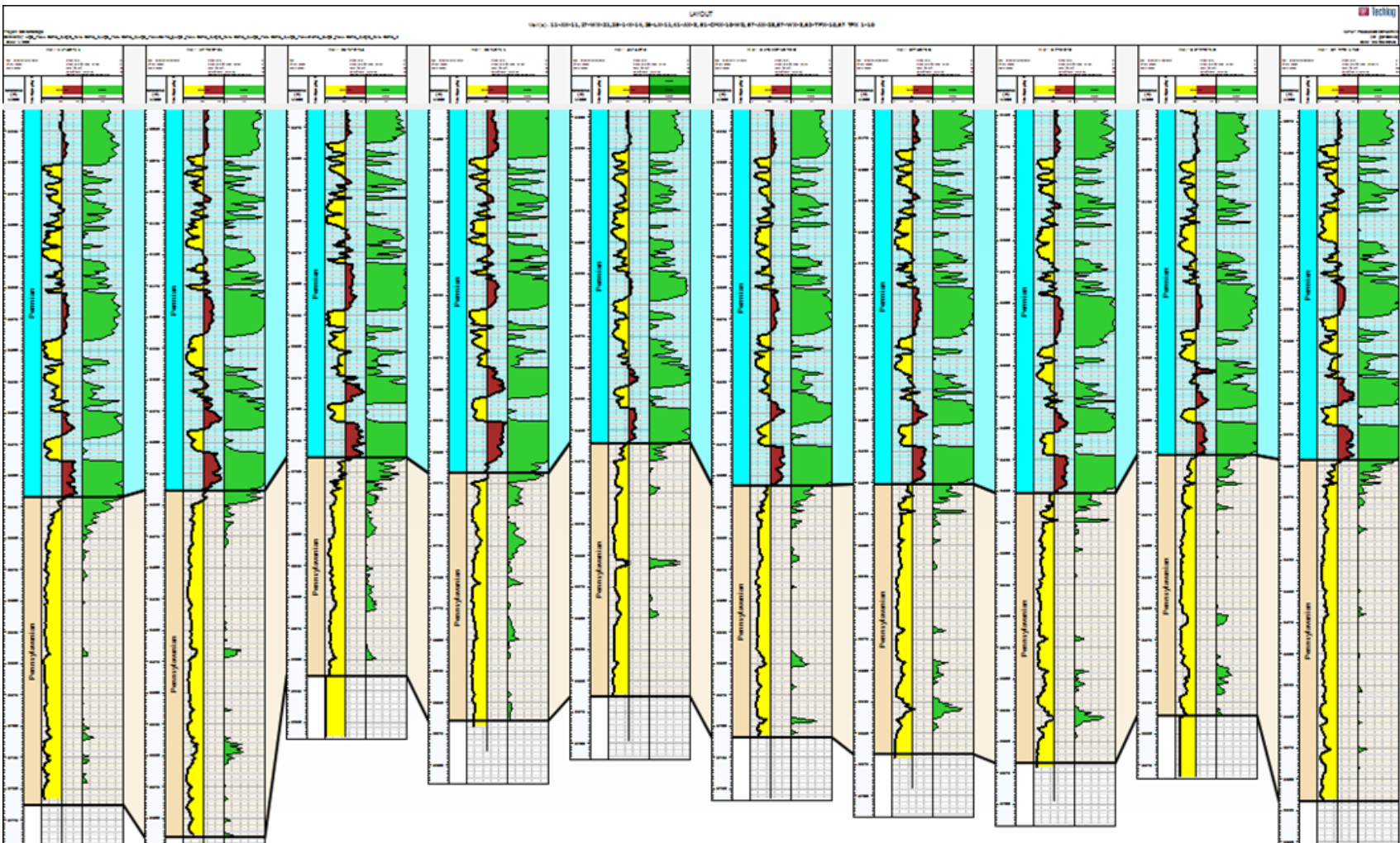


Figure B.16: Logs of all the 10 wells showing the volume of shale in the caprock (Permian layer) and reservoir (Pennsylvanian layer). Logs from left: 11-AX-11, 17-WX-21, 25-1-X-14, 25-LX-11, 41-AX-3, 51-CMX-10-WD, 57-AX-28, 57-WX-3, 62-TPX-10, 67-TPX 1-10.

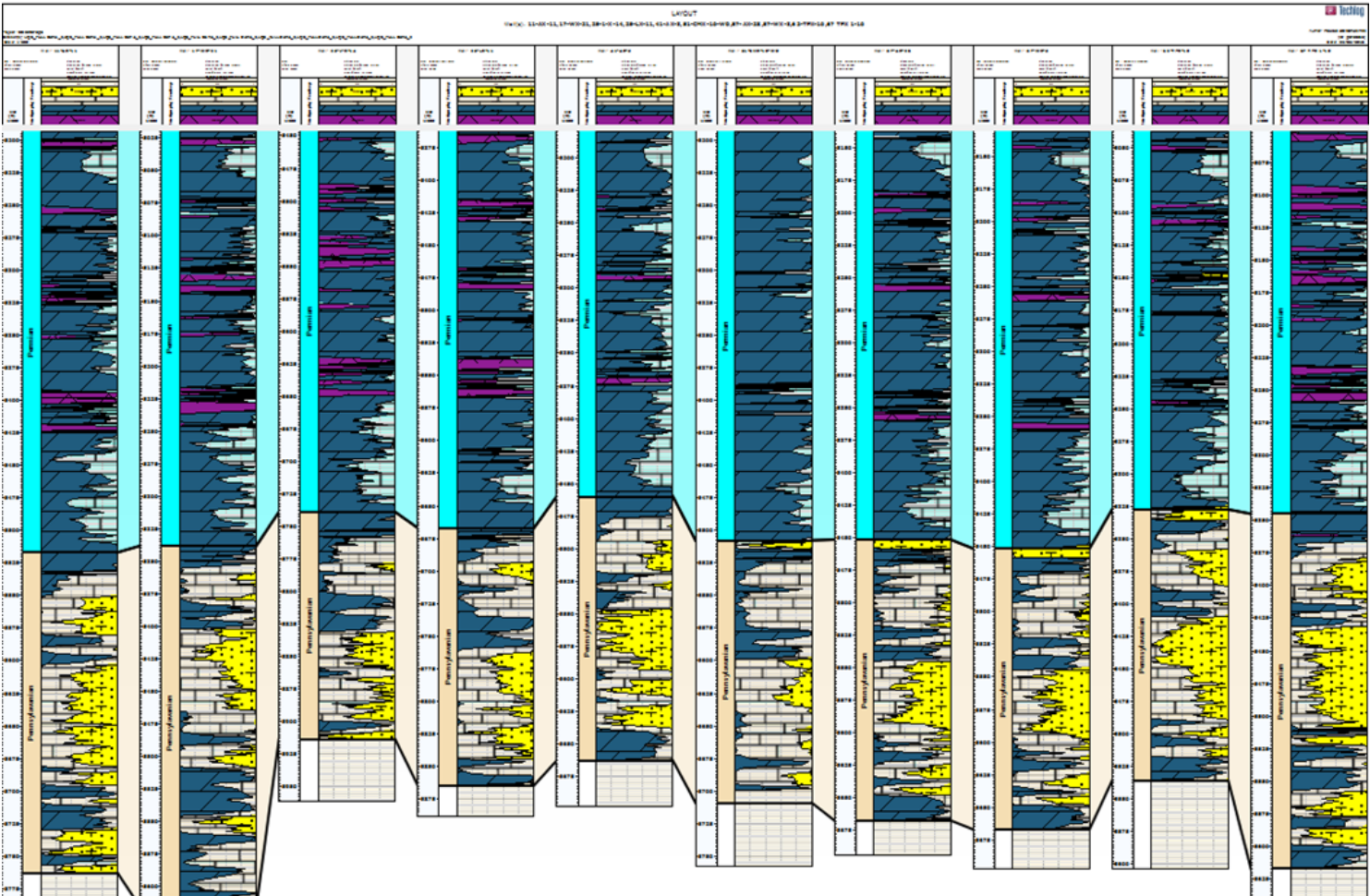


Figure B.17: Logs of all the 10 wells showcasing the mineralogy in the caprock (Permian layer) and reservoir (Pennsylvanian layer). Logs from left: 11-AX-11, 17-WX-21, 25-1-X-14, 25-LX-11, 41-AX-3, 51-CMX-10-WD, 57-AX-28, 57-WX-3, 62-TPX-10, 67-TPX 1-10.

B.4 Bulk Modulus and Bulk Density

Figures B.18-B.19 show the bulk density Permian and Pennsylvanian layer across 10 wells, respectively. Figure B.20 shows bulk modulus for the caprock zone.

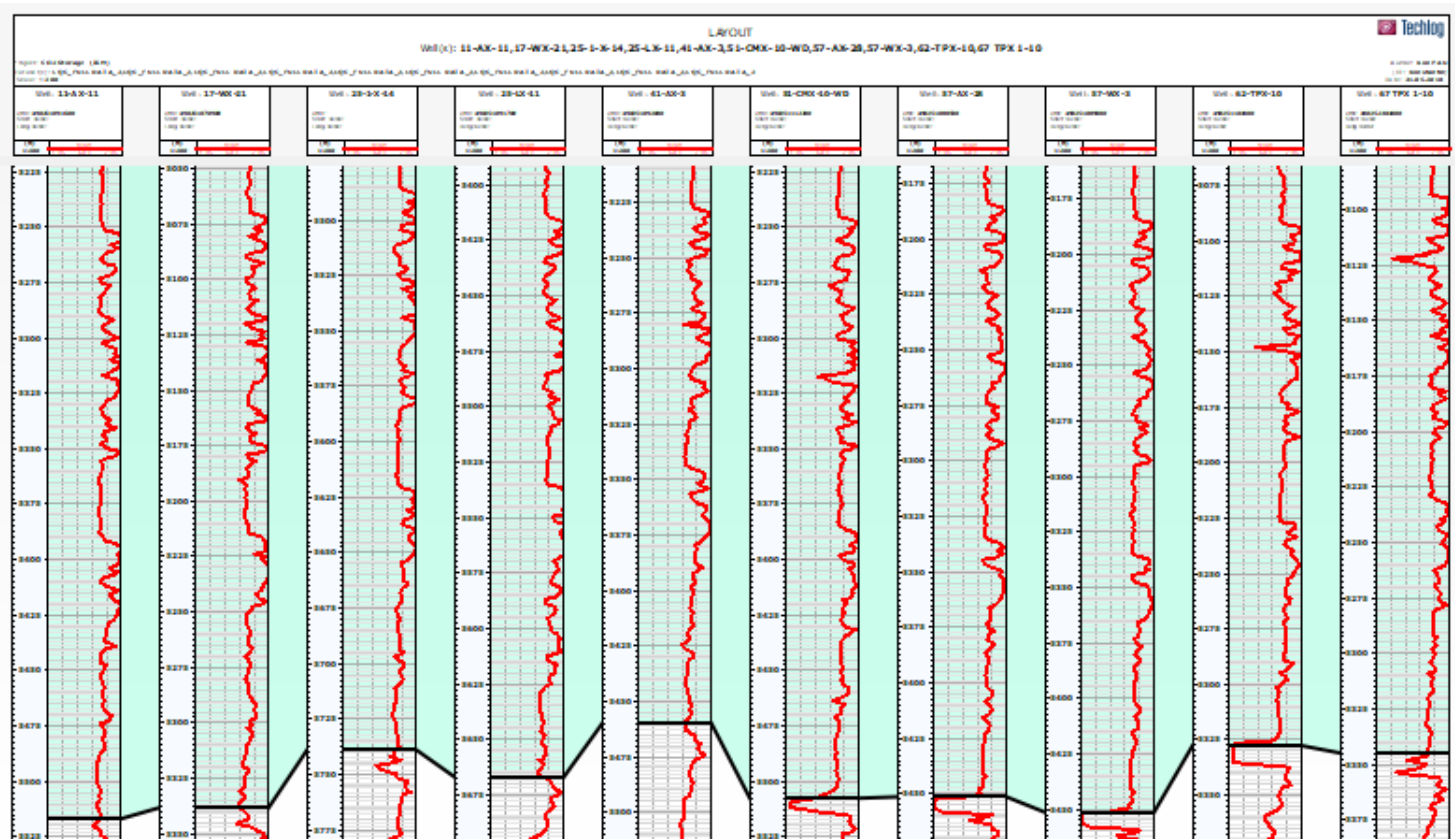


Figure B.18: Logs of all the 10 wells presenting the bulk density in the caprock (Permian layer). Logs from left: 11-AX-11, 17-WX-21, 25-1-X-14, 25-LX-11, 41-AX-3, 51-CMX-10-WD, 57-AX-28, 57-WX-3, 62-TPX-10, 67-TPX 1-10.

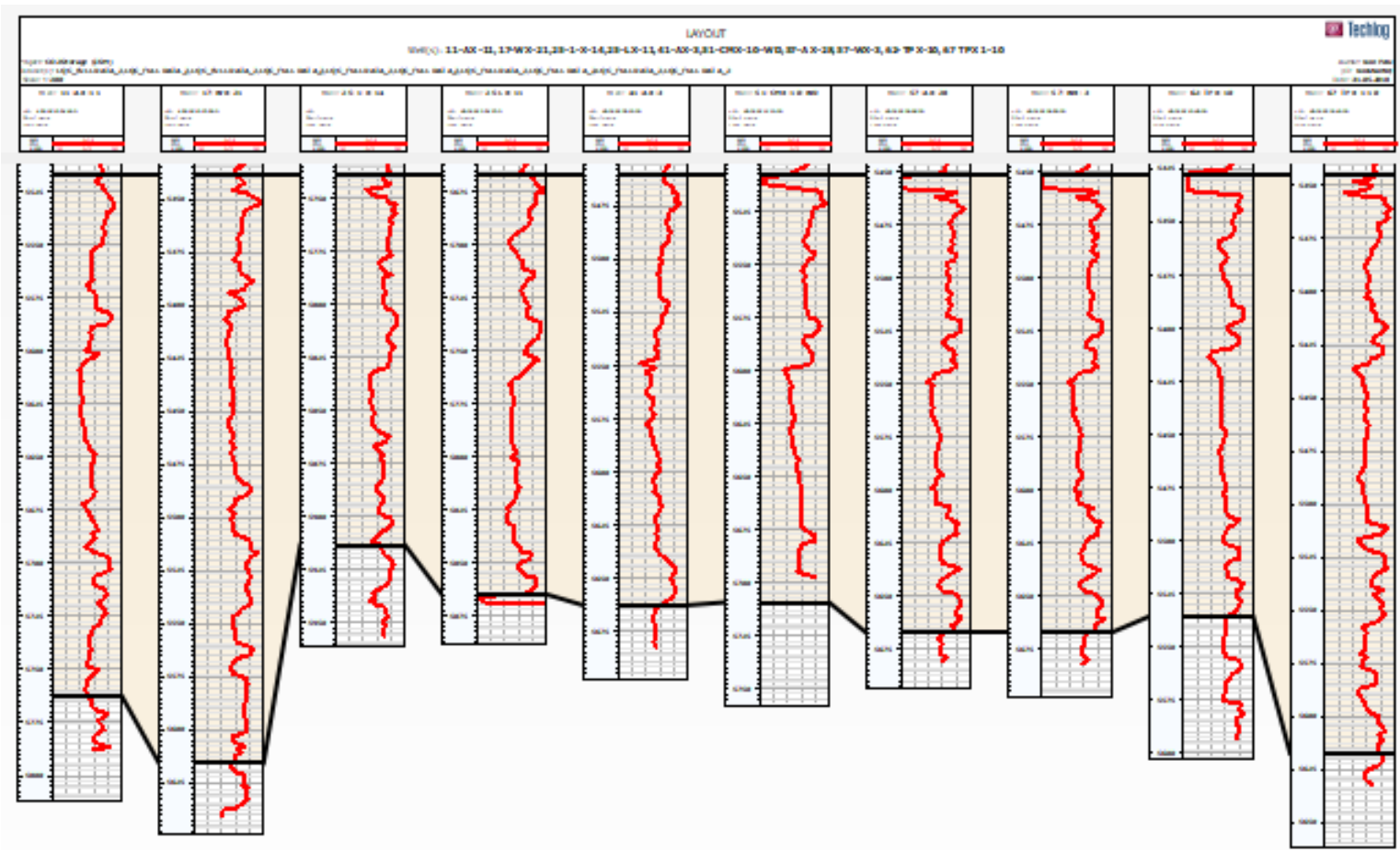


Figure B.19: Logs of all the 10 wells presenting the bulk density in the reservoir (Pennsylvanian layer). Logs from left: 11-AX-11, 17-WX-21, 25-1-X-14, 25-LX-11, 41-AX-3, 51-CMX-10-WD, 57-AX-28, 57-WX-3, 62-TPX-10, 67-TPX 1-10.

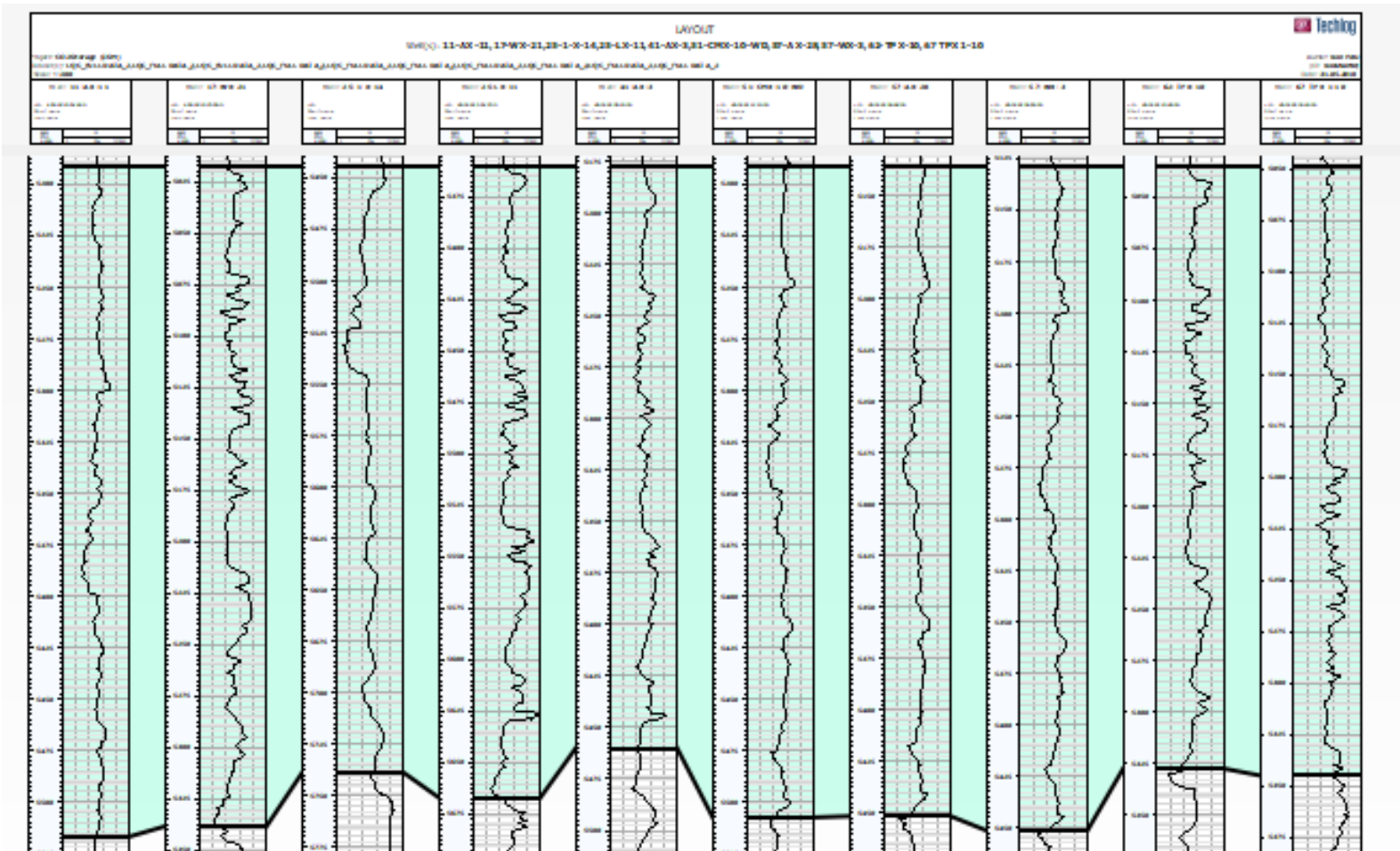


Figure B.20: Logs of all the 10 wells presenting the bulk modulus in the caprock (Permian layer). Logs from left: 11-AX-11, 17-WX-21, 25-1-X-14, 25-LX-11, 41-AX-3, 51-CMX-10-WD, 57-AX-28, 57-WX-3, 62-TPX-10, 67-TPX 1-10.

B.5 Permeability

Figures B.21 to B.22 illustrate the logs for permeability in the caprock and reservoir, respectively.

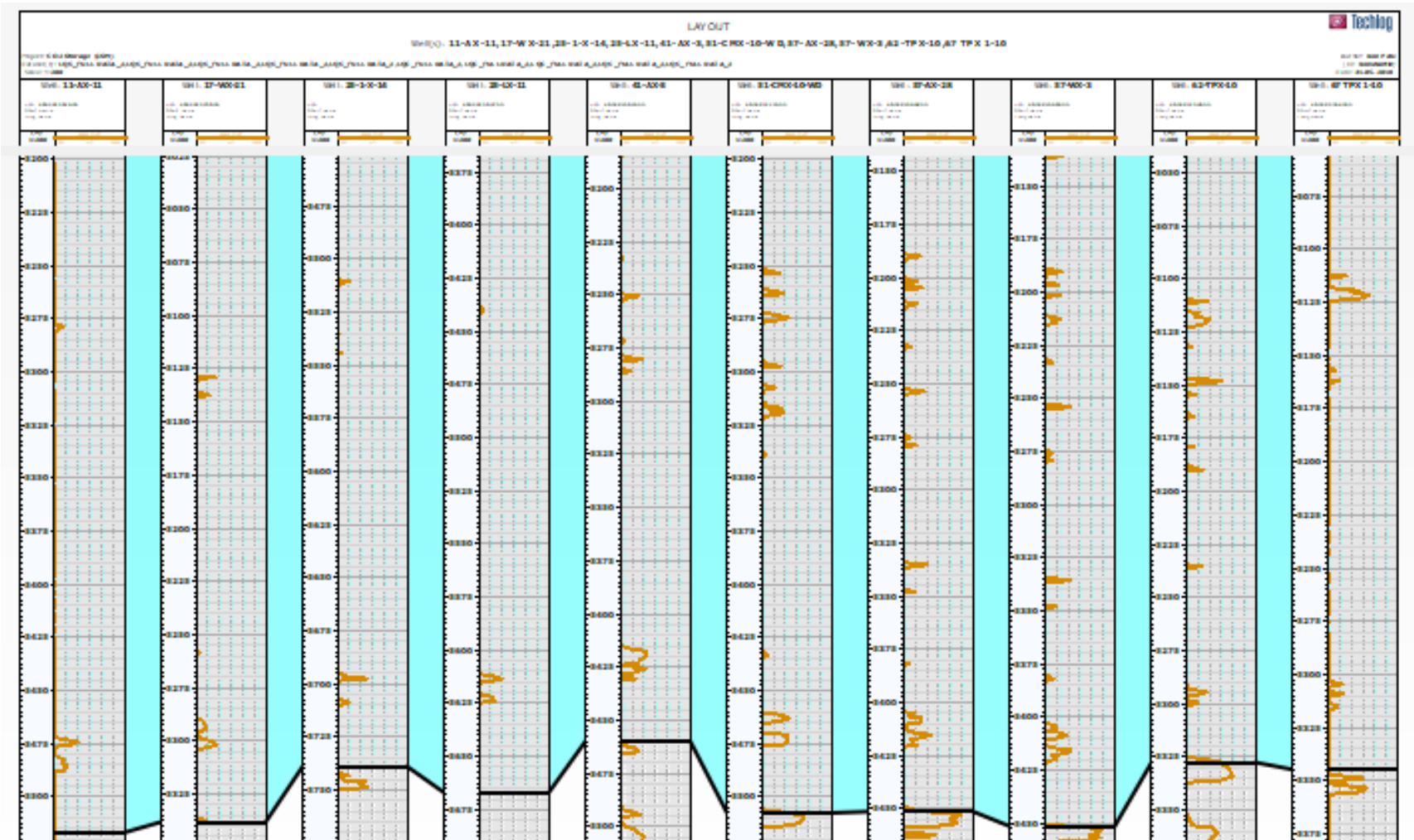


Figure B.21: Logs of all the 10 wells presenting the permeability in the caprock (Permian layer). Logs from left: 11-AX-11, 17-WX-21, 25-1-X-14, 25-LX-11, 41-AX-3, 51-CMX-10-WD, 57-AX-28, 57-WX-3, 62-TPX-10, 67-TPX 1-10.

Additional Data From Petrel[©]

C.1 Elevation Depth

Figure C.1 illustrates the depth distribution across the reservoir area.

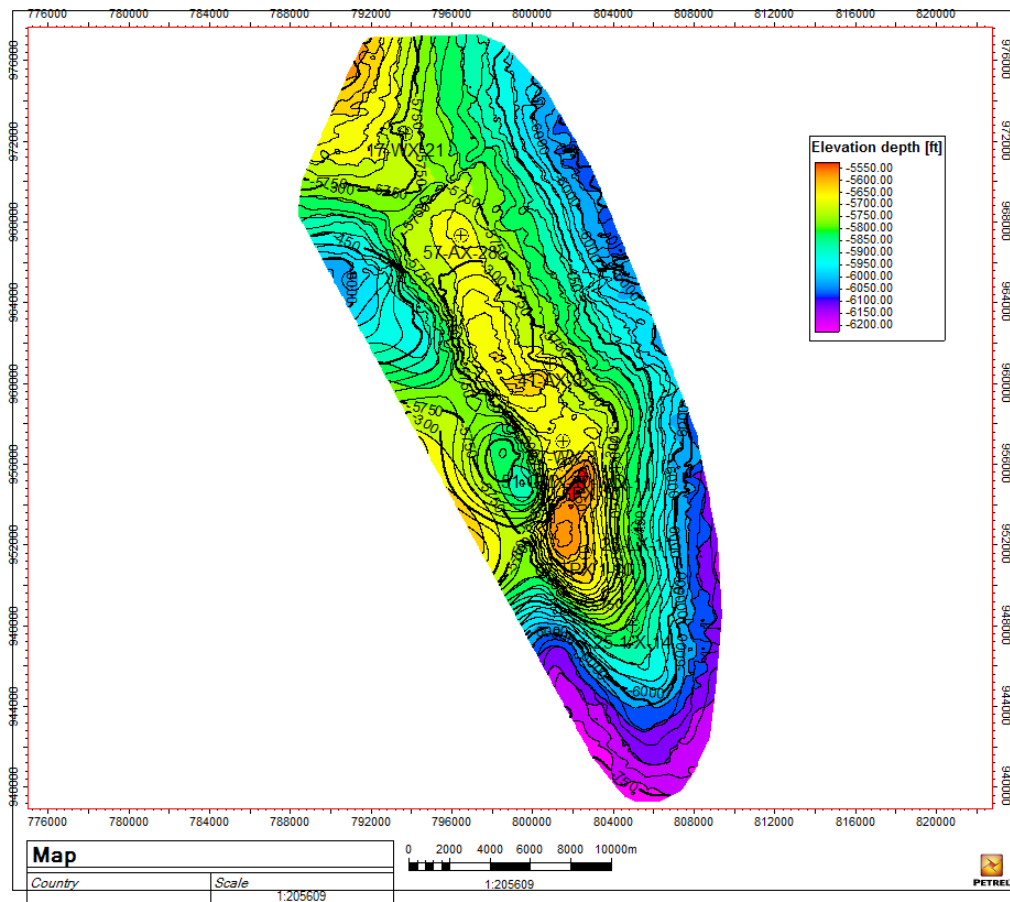


Figure C.1: Elevation depth distribution for reservoir (Pennsylvanian layer).